2014

Modeling Dynamic Stall for a Free Vortex Wake Model of a Floating Offshore Wind Turbine

Evan M. Gaertner
UMass, Amherst, evan.gaertner@gmail.com

MODELING DYNAMIC STALL FOR A FREE VORTEX WAKE MODEL OF A FLOATING OFFSHORE WIND TURBINE

A Thesis Presented

By

EVAN MICHAEL GAERTNER

Submitted to the Graduate School of the
University of Massachusetts Amherst in partial fulfillment
of the requirements for the degree of

MASTER OF SCIENCE IN MECHANICAL ENGINEERING

September 2014

Mechanical Engineering

MODELING DYNAMIC STALL FOR A FREE VORTEX WAKE MODEL OF A FLOATING OFFSHORE WIND TURBINE

A Thesis Presented

By

EVAN MICHAEL GAERTNER

Approved as to style and content by:

_____
Matthew Lackner, Chairperson

_____
James Manwell, Member

_____
James Blair Perot, Member

_____
Donald L. Fisher, Department Head
Department of Mechanical and Industrial Engineering

ACKNOWLEDGMENTS

I would like to thank my adviser and committee chair, Dr. Matt Lackner, for his support and guidance. You have given me every opportunity to succeed in the classroom, on my research, and assistance in obtaining industry internships. I consider myself extremely lucky to work with you and look forward to continuing to do so during my doctoral research. I would also like to thank my committee members Dr. James Manwell and Dr. Blair Perot for their patience and accommodation, especially when I was on hiatus last year.

There are many other people that made this work possible. I am very appreciative of the support from my friends and coworkers at the UMass, Amherst Wind Energy Center. I would also like to thank my friends at Alstom Wind and NREL's National Wind Technology Center, both of which I was very fortunate to work with over the course of my Master's studies.

Finally, I would like to dedicate this work to all the wonderful teachers, tutors, and professors that inspired me over the years, I would not be here without you. From those that instilled a love and curiosity for math, science, and technology, to those that were patient with me when I was less enthusiastic, I am eternally grateful. First and foremost among my teachers are my loving parents, your constant hard work and dedication is the standard to which I hold myself to.

ABSTRACT

MODELING DYNAMIC STALL FOR A FREE VORTEX WAKE MODEL OF A FLOATING OFFSHORE WIND TURBINE

SEPTEMBER 2014

EVAN M. GAERTNER, B.Sc., JAMES MADISON UNIVERSITY
M.S.M.E., UNIVERSITY OF MASSACHUSETTS AMHERST

Directed by: Professor Matthew A. Lackner

Floating offshore wind turbines in deep waters offer significant advantages to onshore and near-shore wind turbines. However, due to the motion of floating platforms in response to wind and wave loading, the aerodynamics are substantially more complex. Traditional aerodynamic models and design codes do not adequately account for the floating platform dynamics to assess its effect on turbine loads and performance. Turbines must therefore be over designed due to loading uncertainty and are not fully optimized for their operating conditions. Previous research at the University of Massachusetts, Amherst developed the Wake Induced Dynamics Simulator, or WInDS, a free vortex wake model of wind turbines that explicitly includes the velocity components from platform motion. WInDS rigorously accounts for the unsteady interactions between the wind turbine rotor and its wake, however, as a potential flow model, the unsteady viscous response in the blade boundary layer is neglected. To address this concern, this thesis presents the development of a Leishman-Beddoes dynamic stall model integrated into WInDS. The stand-alone dynamic stall model was validated against two-dimensional unsteady data from the OSU pitch oscillation experiments and the coupled WInDS

model was validated against three-dimensional data from NREL's UAE Phase VI campaign. WInDS with dynamic stall shows substantial improvements in load predictions for both steady and unsteady conditions over the base version of WInDS. Furthermore, use of WInDS with the dynamic stall model should provide the necessary aerodynamic model fidelity for future research and design work on floating offshore wind turbines.

TABLE OF CONTENTS

Page

LIST OF TABLES

Table **Page**

LIST OF FIGURES

Figure **Page**

CHAPTER 1
INTRODUCTION

Floating offshore wind turbines (FOWTs) are a promising technology poised to provide access to superior offshore wind resources, while avoiding competition of use issues prevalent onshore and near-shore. However, floating platforms are a major technological leap, even compared to fixed bottom offshore wind turbines. This is in part due to additional platform motion which adds complexity to the unsteady aerodynamic operating environment of FOWTs. The existing techniques for modelling unsteady aerodynamics of FOWTs are currently inadequate.

To address these concerns, previous work by Sebastian (2012) developed the Wake Induced Dynamics Simulator (WInDS). WInDS explicitly accounts for platform kinematics using a free vortex wake method. While the model accounts for rotor and platform dynamics and their time-varying impact on the wake development, unsteady aerodynamics are not accounted for at the blade section level. Instead, the current version of WInDS assumes static sectional aerodynamics via two-dimensional airfoil lookup tables, and so while rotor-scale unsteadiness is modeled in WInDS, it is ignored at the blade section scale. Modeling the physics of the unsteady flow at the blade section scale should improve the accuracy of load predictions in WInDS, therefore indirectly improving wake dynamics predictions and overall enabling more accurate assessment of the aerodynamic behavior of FOWTs. In an effort to improve the understanding of the unsteady aerodynamics of FOWTs, this thesis has the following goals:

- Develop and validate a Leishman-Beddoes type dynamic stall model in Matlab
- Interface the dynamic stall model with WInDS
- Validate the coupled model
- Analyze the dynamics stall behavior of FOWTs using the coupled model

Chapter 2 provides relevant background information on offshore wind turbines, wind turbine aerodynamics, and dynamic stall. Chapter 3 outlines the theory and mathematical representation of a Leishman-Beddoes dynamic stall model. Chapter 4 discusses the implementation of the Leishman-Beddoes dynamic stall model and validation against two-dimensional data. Chapter 5 discusses coupling the dynamic stall model with WInDS, validation of the combined code, and sample model results for FOWTs. Finally, Chapter 6 summarizes conclusions and future research opportunities.

CHAPTER 2

BACKGROUND

2.1 Offshore Wind

The best onshore wind resources in the United States (U.S.) are generally found on the plains in the interior of the country or on mountain ridges, shown in Figure 2.1. Development of these resources can be difficult because the plains have low population density and therefore low electricity demand. Development of mountain ridges can be challenging due to competition for use and view shed concerns.

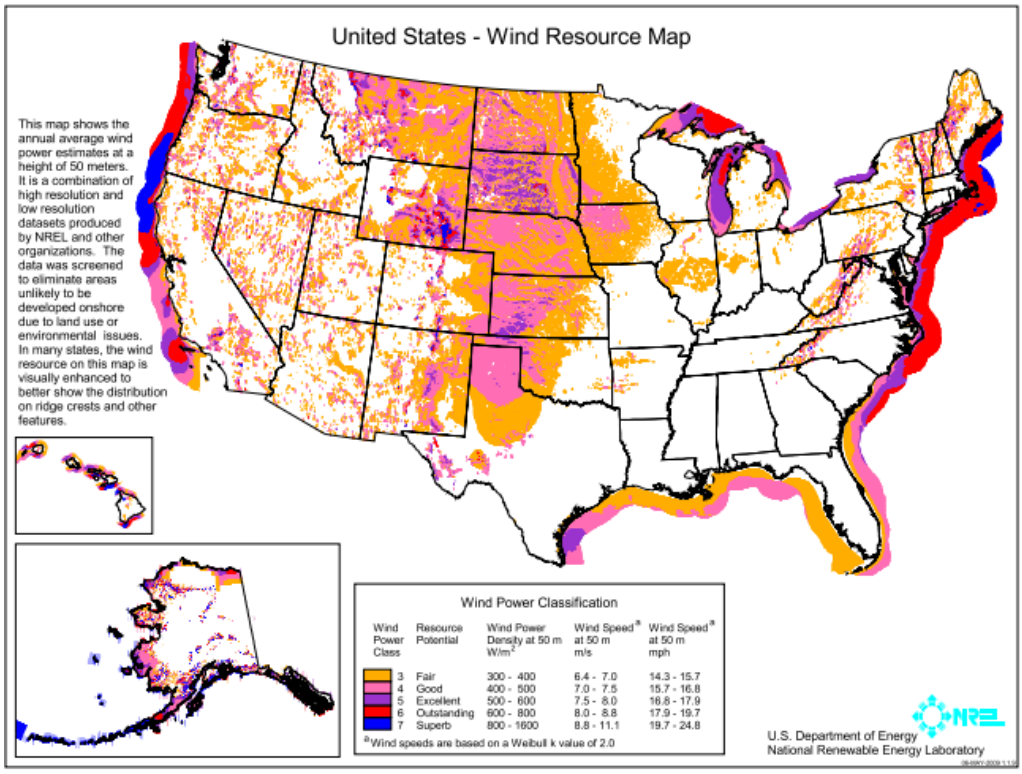

Figure 2.1: United States wind resource map

Offshore wind turbines are a promising application to avoid these issues due to strong offshore wind resources and proximity to population dense load centers. Musial and Ram (2010) estimated that there are sufficient wind resources within 50 miles of shore to provide four times the electrical demand of the United States. Additionally, offshore wind turbines can be larger

than onshore machines due to simplified transportation and have higher efficiency due to reduced noise concerns.

Despite the potential, there are currently no offshore wind farms off the coast of the U.S. due to technical and political challenges. An offshore operational environment is substantially more complex due to wave loading, access issues, and additional expense for installation and maintenance. As more of these concerns are addressed, the cost of offshore wind energy will decrease and development will accelerate, as outlined by Kaiser and Snyder (2010) and Tegen, et al. (2012).

2.1.1 Floating offshore wind turbines

International offshore wind energy development has largely been limited to depths less than 30 m, the limit for monopile foundations. Shallow depths are typically close to the shoreline where viewshed concerns can prevent development. Furthermore, Musial and Ram (2010) estimated that 75% of the U.S. offshore wind resource is at depths greater than 30 m.

FOWTs can provide access to deeper waters, mitigating competition of use concerns and expanding the potential area for development. The technology also has the potential to reduce the cost of energy through tow-out installation of fully assembled systems rather than offshore assembly using specialized lift vessels. A wide variety of concepts have been proposed, however all designs attain stability though a combination of ballast, buoyancy, and mooring line tension, as shown in Figure 2.2. Yu and Chen (2012) provide an overview of the various FOWTs concepts under development.

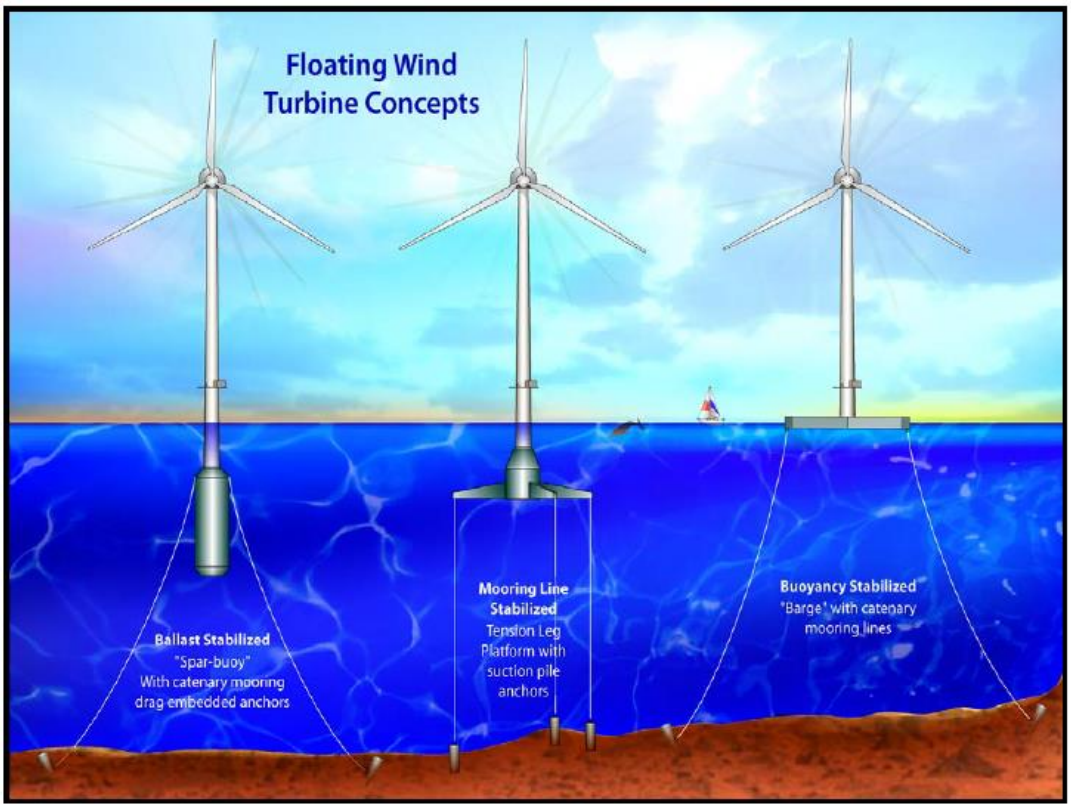

Figure 2.2: FOWT stability concepts (Jonkman, 2007)

2.1.2 Modeling FOWTs

Wind turbines operate in complex unsteady flow fields. The underlying aerodynamics are not fully understood leading to significant limitations to the state-of-the-art aerodynamic models. This was clearly highlighted in a blind comparison conducted by the National Renewable Energy Laboratory (NREL). Experimental data from the NREL Unsteady Aerodynamics Experiment (UAE) at the NASA Ames 80 x 120 ft. wind tunnel were utilized. Twenty independent "blind" sets of predictions were made by the participants, using a variety of models. Simms, et al. (2001) showed the results range from 60% under-prediction to 150% over-prediction. Even in the simplest case in a controlled environment, state-of-the-art models fail to accurately predict wind turbine aerodynamic performance.

FOWTs operate in even more complex conditions than fixed bottom turbines due to additional platform motion. Floating platforms experience 6 degrees of freedom in response to

wind and wave loading, depicted in Figure 2.3. This additional motion results in cyclical loading that can shorten the lifetime of wind turbine components or lead to dynamic instabilities. Additionally, platform motion can cause rapid unsteady wind velocity changes at the blade section level. Sebastian and Lackner (2011) concluded that this would result in increased occurrence and severity of dynamic stall. Sebastian (2012) and Sebastian and Lackner (2012) also found that the complex dynamic inflow conditions due to rotor-wake interactions from platform motion violated the underlying assumptions of many traditional modelling techniques such as Blade Element Momentum Theory.

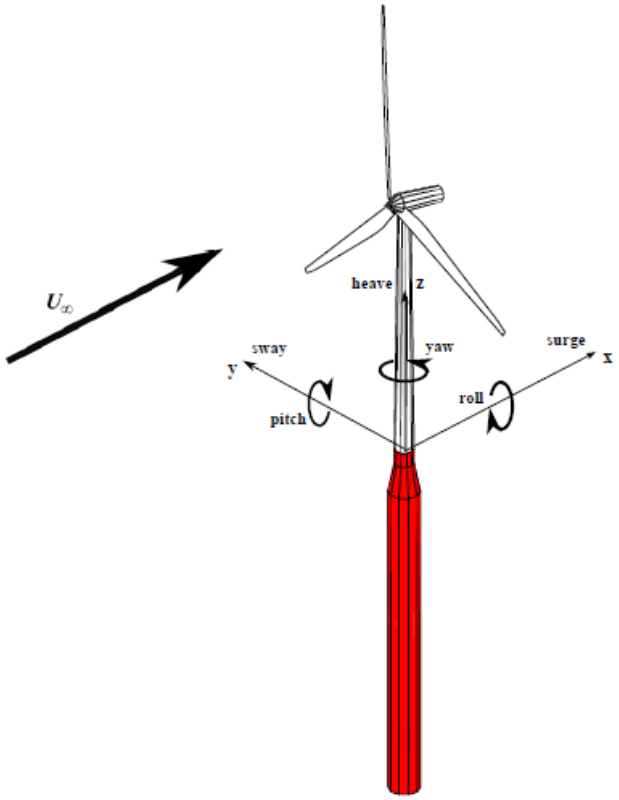

Figure 2.3: Rotational and translational degrees of freedom for FOWTs (Sebastian, 2012)

2.2 Wind Turbine Aerodynamics

2.2.1 Aerodynamic properties of airfoils

An airfoil is a structure that generates lift as a result of favorable pressure gradients as it moves through a fluid. Experimentation with airfoil shapes and properties began prior to the advent of flight, but the first comprehensive study was conducted by the National Advisory Committee for Aeronautics (NACA) in the 1930s and 1940s, summarized in Abbott (1949). Figure 2.4 provides the nomenclature and typical shape of subsonic airfoils.

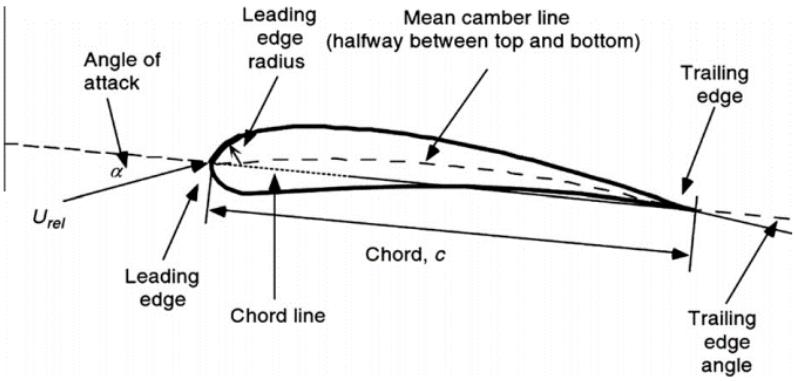

Figure 2.4: Airfoil nomenclature (Manwell, et al. 2002)

Figure 2.5 shows the components of the resultant force on an airfoil in a fluid flow. The normal force and axial force (also referred to as the chord or tangential force) are perpendicular and parallel with the airfoil chord line respectively and lift and drag are perpendicular and parallel to the free stream velocity respectively. Equations 2.1 and 2.2 give the geometric relationships for transferring from normal and axial force to lift and drag.

$$L = N\cos(\alpha) + A\sin(\alpha) \quad [2.1]$$

$$D = N\sin(\alpha) - A\cos(\alpha) \quad [2.2]$$

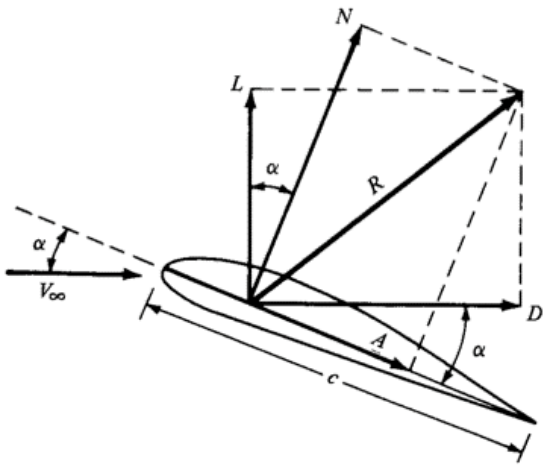

Figure 2.5: Components of the resultant force on an airfoil in a fluid flow (Anderson, 2007)

The aerodynamic properties for an airfoil shape can be experimentally determined in a wind tunnel. Under steady conditions, i.e. constant wind speed and airfoil orientation, the lift coefficient increases linearly with angle of attack under attached flow. At a critical angle, viscous forces cause flow reversals and recirculation along the boundary layer on the suction side resulting in flow separation. The airfoil experiences decreased lift and an increased drag under separated flow at high angles of attack. This phenomenon is known as stall and the angle of attack where stall begins is known as the static stall angle. Figure 2.6 shows a typical steady lift curve.

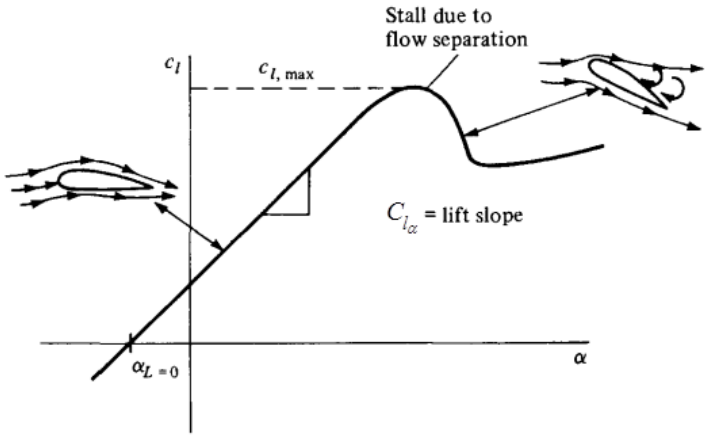

Figure 2.6: C_L-alpha curve (Anderson, 2007)

2.2.2 Potential flow modeling

2.2.2.1 Potential flow

Potential flow is a fluid dynamics analysis technique made possible by three key simplifying assumptions:

- The flow is incompressible. This can be expressed by the continuity equation, Equation 2.3. This assumption is valid for wind turbine applications due to the low Mach number flow fields.

$$\nabla \cdot \mathbf{U} = 0 \qquad [2.3]$$

- The flow is irrotational, expressed in Equation 2.4. Viscous forces are only significant for a thin boundary layer around an airfoil operating in subsonic flow. Therefore for external flows around wind turbines, this is an acceptable assumption.

$$\nabla \times \mathbf{U} = 0 \qquad [2.4]$$

- The flow is inviscid. Due to the large Reynolds numbers for typical wind turbine flow fields, the inertial forces are significantly larger than viscous forces, allowing viscous effects to be neglected.

Equation 2.5 gives the vector identity which states that the curl of the gradient of a scalar function is zero. By combining Equations 2.4 and 2.5, Equation 2.6 gives a new expression of the velocity in terms of ϕ, the velocity potential. The velocity potential function shows that there exists some scalar function where its gradient is the velocity field.

$$\nabla \times (\nabla \phi) = 0 \qquad [2.5]$$

$$\mathbf{U} = \nabla \phi \qquad [2.6]$$

Taking the gradient of the velocity potential function and applying incompressibility yields Laplace's equation, 2.7. The main advantage of Laplace's equation is its linearity. This allows complex flows to be modelled by the superposition of multiple elementary flow solutions.

$$\nabla^2 \phi = 0 \qquad [2.7]$$

2.2.2.2 Vortex filaments

In aerodynamic modeling, the elementary solution to Laplace's equation for vortex flows is particularly useful. A vortex is a flow where the velocity is constant on circular stream lines, decreasing in magnitude with distance from the origin. Equation 2.7 is the velocity profile of a potential vortex where r is the radius from the origin and Γ is the circulation strength as given by Anderson (2005).

$$U_\theta = -\frac{\Gamma}{2\pi r} \qquad [2.7]$$

The extension of potential vortices into three-dimensions is the vortex filament, a closed or infinite curve with concentrated vorticity of constant circulation strength along its length. The filament induces a velocity field around it. The Biot-Savart law can be used to calculate the induced velocity at any given point in the flow field, as shown in Figure 2.7, where a segment of the straight line vortex filament L induces velocity on the point P. Equation 2.8 is an expression of the discretized Biot-Savart law for the velocity at point P as given by Sebastian (2012).

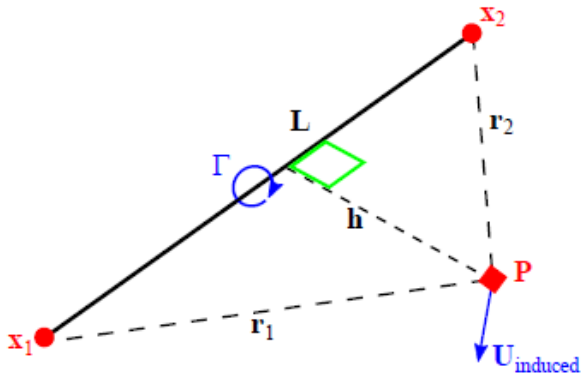

Figure 2.7: Vectors associated with the discretized Biot-Savart law (Sebastian, 2012)

$$U_{induced} = \frac{\Gamma}{4\pi} \frac{\left(|r_1| + |r_2|\right)\left(r_1 \times r_2\right)}{|r_1||r_2|\left(|r_1||r_2| + r_1 \cdot r_2\right)} \qquad [2.8]$$

2.2.2.3 Lifting line theory

The true utility of vortex filaments is given by the Kutta-Joukowski theorem, Equation 2.9, which expresses the lift per unit span on a body in terms of the circulation about the body. This allows a two-dimensional flow about an airfoil to be modeled as a potential vortex or a three-dimensional finite wing to be modelled with vortex filaments.

$$L' = \frac{1}{2}\rho_\infty U_\infty^2 C_l c dy = \rho_\infty U_\infty \Gamma \qquad [2.9]$$

Classical lifting-line theory was developed by Ludwig Prandtl to model finite wings. A bound vortex filament is placed on the quarter-chord of the wing and extends from wing tip to tip, or tip to root in the case of a wind turbine blade. However, vortex filaments must be infinite in length or bound according to the Helmholtz theorem, so two trailing vortex filaments of equal strength are placed at the wing end points, parallel to the free steam flow velocity. This configuration is known as a horseshoe vortex and it is closed by a starting vortex filament, of equal strength to the bound vortex and parallel to the trailing edge, which is shed and convected downstream by the ambient flow. The trailing and shed vortices all induce velocity on the bound vortices according to the Biot-Savart law. To model span-wise variations in lift along a wing,

multiple or an infinite number of horseshoes vortices can be superimposed on the same lifting line, resulting in a sheet of trailing vortices shown in Figure 2.8.

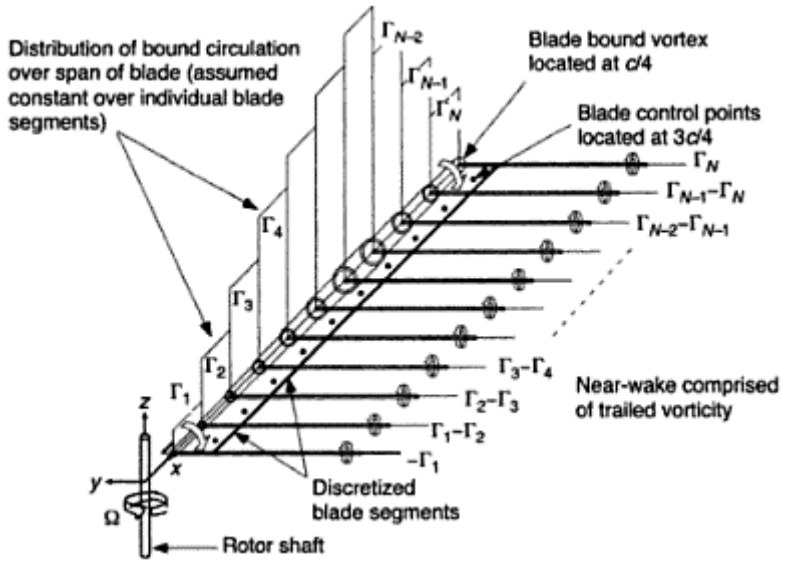

Figure 2.8: Superposition of vortex filaments to form a lifting-line and trailing vorticity (Leishman, 2006)

To model unsteady changes in lift, the circulation strength along the lifting line span can change with time. As a result, shed vortex filaments equal to the change in the bound vorticity with respect to time are released into the wake. Trailing and shed vortices due to spatial and temporal changes in bound vorticity, respectively, dynamically model the wake as a lattice structure of vortex filaments.

An extension of lifting line theory is the free vortex wake model. Using Lagrangian markers, vortex filaments are convected downstream by the free stream fluid velocity and the self-induced velocity of the wake. This allows the structure of the wake to evolve with time as shown in Figure 2.9.

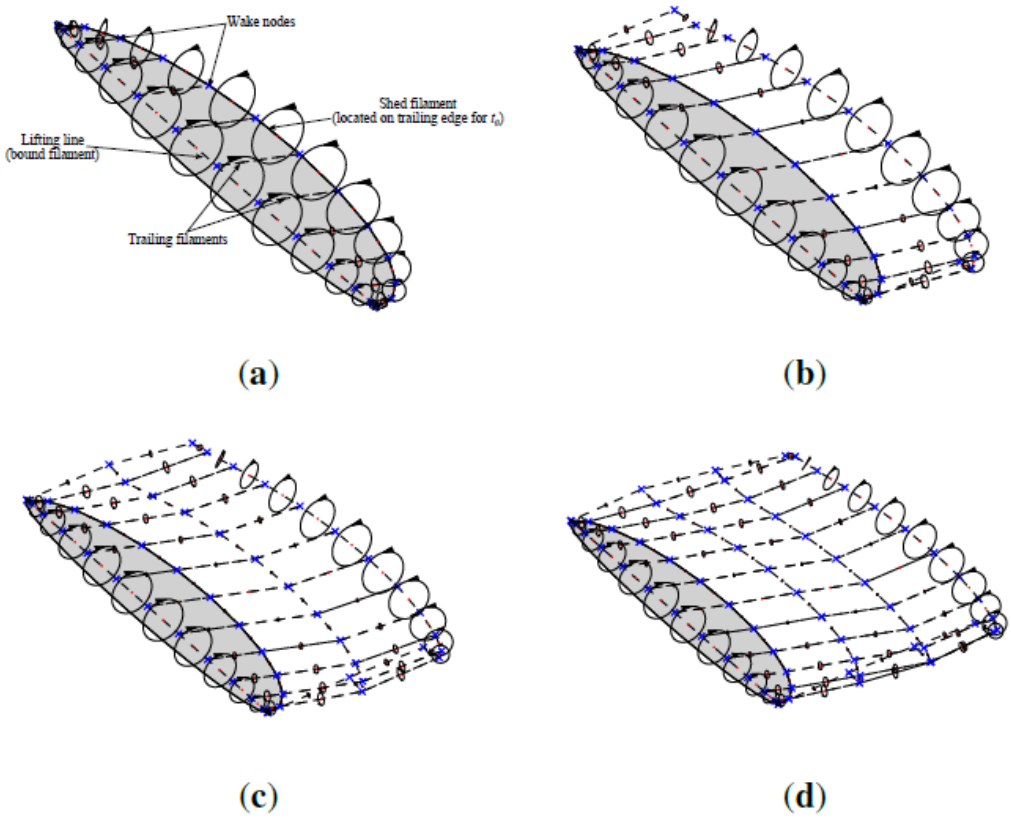

Figure 2.9: Evolution of the vortex lattice wake structure over time (Sebastian and Lackner, 2012); (a) t_0, (b) t_1, (c) t_2, (d) t_3

Difficulties can arise when applying vortex models because the induced velocity approaches infinity near the vortex origin. This is a result of potential vortices being over idealized while true vortices experience viscous shear forces that significantly influence the velocity profile near their origin. Through empirical observations, vortex core models have been developed to account for the discrepancy between potential and physical vortices. Additional corrections are also applied to account for vortex filament strain and stretching as a result of the freely convecting wake. These topics are beyond the scope of this work, but are discussed in detail by Leishman (2006) and Sebastian (2012).

2.2.3 Wake Induced Dynamics Simulator

To address the need for more sophisticated methods for modeling the aerodynamics of FOWTs, the Wind Energy Center at the University of Massachusetts, Amherst, developed the Wake Induced Dynamics Simulator (WInDS) through the work of Sebastian (2012) and updates by deVelder (2014). WInDS is a free vortex wake method potential flow code written in Matlab, and used to model the aerodynamic loads on operating wind turbines and their wake development. The main advantage of this modeling technique is the ability to superimpose velocity contributions from different modes of forcing. The local velocity at a blade filament can include contributions from the free stream, induced velocity from the wake, and velocity from the platform motion, as shown in Equation 2.10. Thus, platform motion and off-axis flow are explicitly accounted for in the aerodynamic model.

$$U = U_{\infty} + U_{induced} + U_{platform} \qquad [2.10]$$

The main WInDS algorithm is shown in Algorithm 1, as given by Sebastian (2012). During simulation time stepping, the induced velocities due to wake effects are calculated to yield the dynamic loads due to rotor-wake interaction. Structural motions of the platform, turbine, and rotor are prescribed, either by user inputs or by importing output data from a FAST simulation. FAST (Fatigue, Aerodynamics, Structures, and Turbulence) is a widely used computer-aided engineering tool developed by NREL used for time-marching simulations of operating wind turbines, outlined in detail by Jonkman and Buhl (2005) and Jonkman (2007).

Since WInDs is a potential flow model, the flow is assumed to be inviscid, incompressible, and irrotational. Consequently, blade section level viscous effects cannot be modeled. Coupling the model with a dynamic stall module has the potential to improve the accuracy of the bound vortex strength calculations and thus the accuracy of the global model.

Algorithm 1: WInDS Algorithm

Data: Turbine geometry and load conditions
Results: Turbine loads and wake geometry

1 Import turbine geometry and load conditions
2 Determine position of blade nodes because of platform, turbine, and rotor motions
3 Compute velocity of blade nodes via rotation sequence
4 Determine initial values for span-wise C_l and Γ_{bound} using Blade Element Momentum theory
5 **for** *all time steps*
6 Compute Γ_{shed} and Γ_{trail}
7 Compute vortex core size, including filament strain effects
8 Compute induction at all wake nodes via Biot-Savart law
9 Convect wake nodes via numerical integration
10 Compute new Γ_{bound} via iteration on Kutta-Joukowski theorem (Algorithm 2)

2.3 Dynamic Stall

2.3.1 Sources of unsteadiness

Robinson, et al. (1995), Huyer et al. (1996), and Sebastian and Lackner (2012) showed that wind turbines operate in complex, unsteady flow fields at all times. This results in significant deviation from the expected aerodynamic response from steady wind tunnel tests. Time varying wind at the blade element can be caused by rotor yaw, ambient turbulence, blade flapping and vibration, and induced wake effects, such as tower shadow. Since wind turbines operate at low tip speed ratios, the incident wind is a significant portion of the flow velocity seen by a blade element, especially for portions of the blade span closer to the root. As a result, sudden changes in the wind speed or direction can cause dramatic changes in the angle of attack. Figure 2.10 shows changes in the local wind velocity for a blade element as a result of unsteady effects.

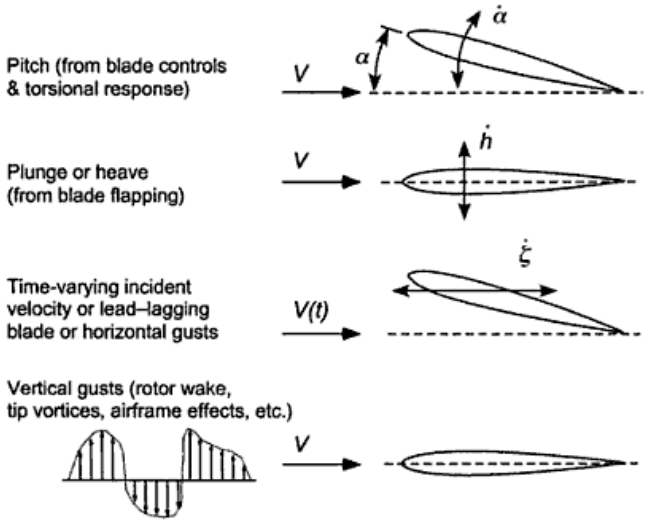

Figure 2.10: Sources of unsteady forcing on a blade element (Leishman, 2006)

It can be useful to quantify the unsteadiness in a flow or forcing term. This is accomplished using the reduced frequency (k) shown in Equation 2.1. The variable ω is the angular frequency of oscillatory changes. Table 2.1 classifies the unsteadiness of flows based on the reduced frequency according to Leishman (2006).

$$k = \frac{\omega c}{2V} \qquad [2.1]$$

Table 2.1: Reduced frequency ranges

Range	Flow Type
$k = 0$	steady
$0 < k \leq 0.05$	quasi-steady
$0.05 < k \leq 0.2$	unsteady
$k \geq 0.2$	highly unsteady

2.3.2 Dynamic stall

McCroskey et al. (1976) first defined dynamic stall as the time varying phenomenon where flow separates from a lift generating structure causing it to stall. It occurs whenever an airfoil undergoes a time varying change in motion or incident flow, resulting in the effective angle of attack exceeding the static stall angle. Flow separation is delayed to a higher angle of attack than the static case, allowing greater lift to be achieved, as observed by Kramer (1932).

Flow separation is initiated by a vortical disturbance shedding from the leading edge of the airfoil. The vortex convects rapidly down the chord resulting in separated flow. While the vortex is in the vicinity of the suction side of the airfoil, additional lift is induced. Additionally, the center of pressure moves toward the trailing edge as the vortex convects down the chord. This results in a nose-down pitching moment of the blade section which can cause undesirable torsional loading, because flow separation is not uniform over the full length of the blade. Aerodynamic damping can also be reduced due to separated flow, potentially resulting in blade instabilities, referred to as stall flutter. Dynamic stall is therefore an important design consideration since peak loads often occur during flow separation and increased blade vibration and stresses could potentially exceed structural fatigue limits.

Section 2.2.3.1 discusses the flow morphology in greater detail and Section 2.2.3.2 will discusses modelling methods for dynamic stall. Chapter 3 discusses implementation of the Leishman-Beddoes dynamic stall model in detail.

2.3.3.1 Flow morphology

Dynamic stall can be divided into five stages as shown in Figure 2.11. Leishman (2006) has provided a useful overview of this process.

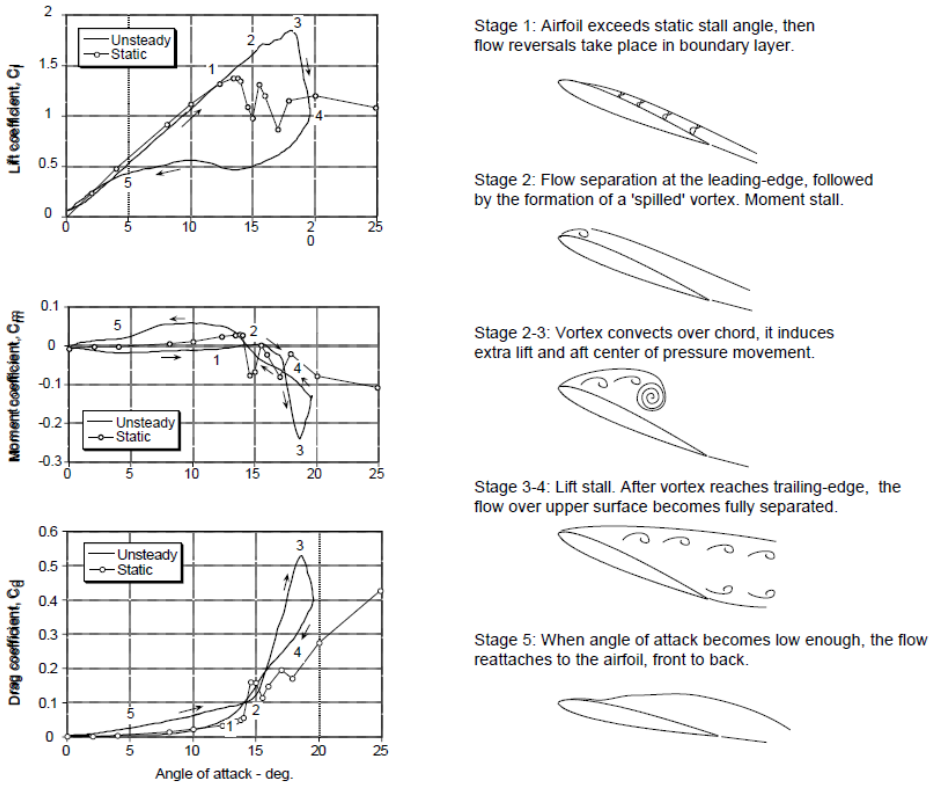

Figure 2.11: Progress of dynamic stall (Leishman, 2006)

At Stage 1, the static stall angle is surpassed, yet flow separation is delayed and lift continues to increase with angle of attack. This can be explained in part by classical 2-D thin airfoil theory and Theodorsen's Theory (1935). When circulation about an airfoil changes (i.e. lift changes), an equal and opposite circulation is shed into the wake at the trailing edge. This counter-circulation in the wake induces a down washing force on the airfoil which delays vortex formation.

In addition to wake effects, leading edge pressure and pressure gradients are reduced by a positive pitch rate compared to the steady case, a well know phenomenon studied by Ericsson (1967), Carta (1971), Ericsson and Redding (1972), Johnson and Ham (1972), McCroskey (1973), and Beddoes (1978). As the airfoil pitches away from the incident flow, the airfoil camber is effective changed. Adverse pressure gradients are also curbed by the development of

unsteady flow reversals in the boundary layer according to work by McAlister and Carr (1979). A combination of these effects creates a delay in flow separation beyond the static stall angle.

Once the pressure gradient at the leading edge become sufficiently high, viscous shear forces cause a vortex to form as the flow folds in on itself. This was first modelled by Ham (1968) and represents Stage 2 in Figure 2.11. The vortex is unstable and quickly convects down the airfoil at approximately 1/3 to 1/2 the free stream velocity during Stage 3. The center of pressure moves toward the trailing edge as the vortex moves aft. Additional lift is provided by the vortex until it passes the trailing edge at which point the flow is fully separated and Stage 4 begins. The airfoil undergoes a sudden drop in lift, a peak nose-down pitching moment, and high drag.

As the angle of attack decreases below the static stall angle, flow begins to reattach. However, this process experiences a similar lag as flow detachment as discussed in Green and Galbraith (1995). The delay is brought on by the reorganization of the flow on the suction side as flow reattaches. A negative pitch rate also causes decreased lift, opposite of the effect described in Stage 1. The angle of attack must therefore decrease below the static stall limit for flow to become fully attached. Once reattached, Stage 5 is reached and the cycle is completed. Delays in flow detachment and reattachment result in a hysteresis effect, shown in the lift plot in Figure 2.11, that is characteristic of dynamic stall.

2.3.3.2 Modeling dynamic stall

Due to the nonlinear, transient, viscous forces during flow separation, dynamic stall can only be rigorously modeled by numerically solving the Navier-Stokes equation. This makes computational fluid dynamics (CFD) with sophisticated turbulence models the ideal method to predict dynamic stall onset and effects. However due to the complexity of the problem, current models are insufficiently accurate to justify the large computational expense. According to Sims,

et al. (2001), as the cost of computational resources continue to decrease, CFD models will more accurately capture the physics of dynamic stall. Even if these models yield improved results, the large computational expense and long run-times will still make CFD impractical for design work which requires extensive simulations and load-cases.

Since dynamic stall is an important consideration in calculating aerodynamic loads and for blade and rotor design, less precise methods have been developed that employ simplified physical representations augmented with experimental data from 2D unsteady airfoil experiments. These semi-empirical or engineering level models are a balance between accurate load predictions and computational complexity. They vary widely by the methods they employ and the amount of experimental data required. Leishman (2002, 2006) has written an overview of these modeling techniques.

Semi-empirical methods can offer significant improvements in model performance, but they have several inherent weaknesses. Typically, empirical coefficients are derived using parameter ID methods that are only accurate over the range of Mach numbers, Reynolds numbers, excitation frequencies, and airfoil shapes represented in the experimental data. Furthermore, their accuracy is dependent on the quality of the experimental data, which can be problematic since airfoil experiments are notoriously difficult to repeat between different experimental setups, discussed by Tangler (2002). This makes validation of these models essential and care should be taken when applying them to problems outside their design conditions.

CHAPTER 3

LEISHMAN-BEDDOES DYNAMIC STALL MODEL

3.1 Overview

The Leishman-Beddoes (L-B) method is a commonly used semi-empirical model of dynamic stall, developed by Beddoes (1983), Leishman and Beddoes (1986, 1989), Leishman (1989), and Tyler and Leishman (1992). At a given blade element, the wind velocity is the main input and the aerodynamic loads are the output, allowing the dynamic model to replace experimental data table look ups. The L-B model is based on simplified physical representations of the flow morphology. The model is divided into four subsystems shown in Figure 3.1: unsteady attached flow, trailing edge flow separation, leading edge flow separation, and vortex shedding. Representation of complex viscous effects are avoided through the use of empirically derived time constants from unsteady, 2-D oscillating or plunging wind tunnel experiments. The subsequent sections outline the theory behind each subsystem and additional modelling considerations such as subsystem interaction.

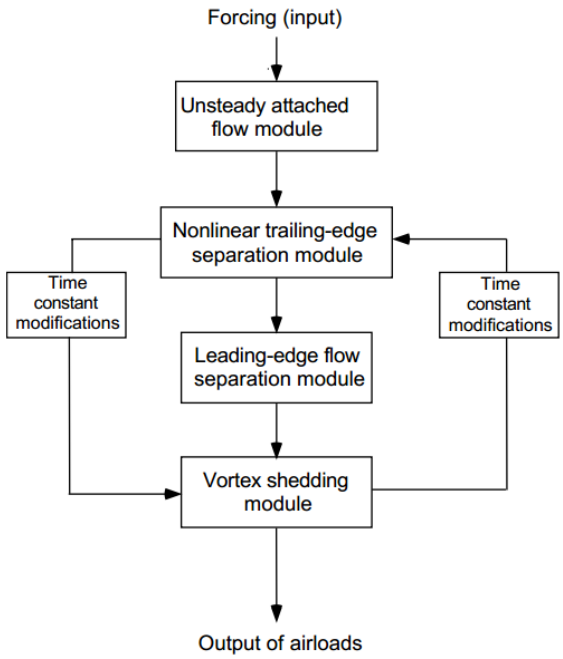

Figure 3.1: Dynamic stall flowchart (Leishman, 2002)

3.2 Unsteady Attached Flow

Under attached flow conditions a blade element experiences dynamically changing aerodynamic loads due to unsteadiness in the flow field, motion of the airfoil, and induced forces from the wake. An unsteady attached flow model is therefore a prerequisite to modeling dynamic stall. Wagner (1925) derived an expression for the coefficient of lift, C_l, on a thin airfoil for a step change in angle of attack, α, in incompressible flow as

$$C_l(t) = \frac{\pi c}{2V}\delta(t) + 2\pi\alpha\phi(s) \qquad [3.1]$$

Where $\delta(t)$ is the Dirac-delta function representing a step change and φ is the Wagner function which approximates the wake effects. The Wagner function is determined based on s, the dimensionless distance traveled by the airfoil in semi-chords defined as

$$s = \frac{2}{c}\int_0^t U(t)dt \qquad [3.2]$$

The first term of Equation 3.1 represents the apparent mass while the second term represents the circulatory effects of the wake. The Wagner function is determined using indicial response theory, which states that the response of a non-linear system to an arbitrary time-dependent input can be calculated if the characteristic response of the system is known. The indicial response of the system can be solved exactly for incompressible flow using a Duhamel integral for an arbitrary forcing function, shown in Equation 3.3.

$$y(t) = f(0)\phi(t) + \int_0^t \frac{df}{dt}\phi(t-\sigma)\,d\sigma \qquad [3.3]$$

Where $y(t)$ is the output of the system, $f(t)$ is a general forcing function, and σ is time variable of integration. Use of the Durhamel integral is based on the principle that the response of the system can be linearized and determined by the superposition of multiple indicial responses

to different modes of forcing. Unfortunately, analytical and numeric solutions to the Wagner function are too computationally intensive for most applications. Rather, it may be replaced with an indicial exponential approximation of the form

$$\phi(s) = 1 - A_1 e^{-b_1 s} - A_2 e^{-b_2 s} \qquad [3.4]$$

Equation 3.4 was first used to approximate the Wagner function by Jones (1938, 1940) for specific cases and generally by Beddoes (1984). The indicial coefficients A_1, A_2, b_1, and b_2 are empirically derived by system identification methods from unsteady airfoil data. Beddoes determined the normal force indicial response for the step changes in angle of attack (α) and non-dimensional pitching rate ($q = \dot{\alpha} c / V$), Equations 3.5 and 3.6 respectively.

$$\frac{C_{n_\alpha}}{\alpha} = \frac{4}{M}\phi_\alpha^{nc}(s, M) + \frac{2\pi}{\beta}\phi_\alpha^{c}(s, M) \qquad [3.5]$$

$$\frac{C_{n_q}}{q} = \frac{1}{M}\phi_q^{nc}(s, M) + \frac{\pi}{\beta}\phi_q^{c}(s, M) \qquad [3.6]$$

Where M is the Mach number and $\beta = \sqrt{1 - M^2}$. The indicial functions for the circulatory terms are assumed to be equal, that is

$$\phi_\alpha^c(s, M) = \phi_q^c(s, M) = 1 - A_1 e^{-b_1 \beta^2 s} - A_2 e^{-b_2 \beta^2 s} \qquad [3.7]$$

Using Equation 3.7, the circulatory contribution to coefficient of lift can be expressed as a function of angle of attack in terms of the Duhamel integral. This representation is shown in Equation 3.8 where C_{n_α} is the steady normal force curve slope for attached flow, 2π/radian under thin airfoil theory. The Duhamel integral can be represented as an effective angle of attack, α_e, which accounts for the flow history, Equation 3.9.

$$C_n(t) = C_{n_\alpha}\left[\alpha(t_0)\phi(s) + \int_{s_0}^{s} \frac{d\alpha}{dt}(\sigma)\phi(s-\sigma)\,d\sigma\right] \quad [3.8]$$

$$C_n^c(t) = C_{n_\alpha}\alpha_e(t) \quad [3.9]$$

Beddoes (1976, 1984) solved the Duhamel integral to express α_e in terms of deficiency functions acting on the angle of attack, shown in Equations 3.10 to 3.12.

$$\alpha_{e_n} = \alpha_n - X_n - Y_n \quad [3.10]$$

$$X_n = X_{n-1}e^{-b_1\beta^2\Delta s} + A_1\Delta\alpha_n e^{-b_1\beta^2\Delta s/2} \quad [3.11]$$

$$Y_n = Y_{n-1}e^{-b_2\beta^2\Delta s} + A_2\Delta\alpha_n e^{-b_2\beta^2\Delta s/2} \quad [3.12]$$

The non-circulatory added mass term is a result of the airfoil displacing fluid as it undergoes pitching and plunging. For compressible flows, the non-circulatory term also accounts for the propagation of acoustical compression and expansion waves. The indicial response functions for angle of attack and pitching rate, Equations 3.13 and 3.14, are represented by a single exponential function.

$$\phi_\alpha^{nc}(s,M) = \exp\left(-s\frac{a}{2Vk_\alpha}\right) \quad [3.13]$$

$$\phi_q^{nc}(s,M) = \exp\left(-s\frac{a}{2Vk_q}\right) \quad [3.14]$$

The literature typically expresses the exponential in these equation in terms of the time constants T'_α and T'_q. For consistency with the subsequent equations however, k_α and k_q have been used which are related by

$$k_\alpha = \frac{c}{2VT_I}T'_\alpha \;,\; k_q = \frac{c}{2VT_I}T'_q \;, \text{ Where } T_I = \frac{c}{a}$$

Lomax, et al. (1952) showed that the indicial response can be solved exactly. Therefore the time constants can be solved for, resulting in Equations 3.15 and 3.16.

$$k_\alpha = 0.75\left[\left(1-M\right)+\pi\beta^2 M^2\left(A_1 b_1 + A_2 b_2\right)\right]^{-1} \quad [3.15]$$

$$k_q = 0.75\left[\left(1-M\right)+2\pi\beta^2 M^2\left(A_1 b_1 + A_2 b_2\right)\right]^{-1} \quad [3.16]$$

To calculate the non-circulatory contribution to lift, the Duhamel integral is applied and rearranged in terms of a deficiency function that captures the time history of the flow, similar to the circulatory contribution. Different forcing modes must be determined separately, in Equations 3.17 and 3.18 for angle of attack and pitch rate.

$$C_{n_\alpha}^{nc} = \frac{4k_\alpha T_I}{M}\left(K_{\alpha_n} - K'_{\alpha_n}\right) \quad [3.17]$$

$$C_{n_q}^{nc} = \frac{k_q T_I}{M}\left(K_{q_n} - K'_{q_n}\right) \quad [3.18]$$

The *K* terms in Equations 3.19 and 3.20 are the rate of the forcing perturbations and *K'* terms in Equations 3.21 and 3.22 are the deficiency functions.

$$K_{\alpha_n} = \frac{\alpha_n - \alpha_{n-1}}{\Delta t} \quad [3.19]$$

$$K_{q_n} = \frac{q_n - q_{n-1}}{\Delta t} \quad [3.20]$$

$$K'_{\alpha_n} = K'_{\alpha_{n-1}} e^{\left(\frac{-\Delta t}{2k_\alpha T_I}\right)} + \left(K_{\alpha_n} - K_{\alpha_{n-1}}\right) e^{\left(\frac{-\Delta t}{2k_\alpha T_I}\right)} \quad [3.21]$$

$$K'_{q_n} = K'_{q_{n-1}} e^{\left(\frac{-\Delta t}{2k_q T_I}\right)} + \left(K_{q_n} - K_{q_{n-1}}\right) e^{\left(\frac{-\Delta t}{2k_q T_I}\right)} \quad [3.22]$$

Then by linear superposition in Equation 3.23, the total potential coefficient of normal force under attached flow is the sum of all circulatory and non-circulatory components.

$$C_{n_n}^{p} = C_{n_\alpha}^{c} + C_{n_\alpha}^{nc} + C_{n_q}^{nc} \quad [3.23]$$

3.3 Trailing Edge Flow Separation

Gradual trailing edge flow separation can be observed before airfoils experience dynamic stall through leading edge vortex shedding. This phenomenon is more pronounced for thicker airfoils, like those used in wind turbine applications. Trailing edge flow separation results in non-linear forces which must be accounted for if the model is to be applicable over a wide range of forcing conditions and airfoil shapes.

In the L-B model, trailing edge flow separation is modelled using the Kirchhoff and Helmholtz Theory, outlined by Thwaites (1987). Under steady conditions, Equation 3.24 is used to express normal force as a function of the trailing edge separation point, *f*, and angle of attack. The separation point is expressed as a ratio of position from the leading edge over chord length, where 1 is fully attached at the trailing edge and 0 is fully separated at the leading edge. The chord force can similarly be expressed as Equation 3.25, where η_e is the recovery factor. The recovery factor accounts for not all of the chord force predicted by potential flow being realized. It is calculated by resolving Equations 3.24 and 2.25 to find the coefficient of drag and performing a least squares fit to the static drag data. Values for recovery factor vary between airfoils, typically in the range of $0.85 \leq \eta_e \leq 1.0$.

$$C_n(\alpha, f) = C_{n_\alpha}\left(\frac{1+\sqrt{f}}{2}\right)^2 \alpha \quad [3.24]$$

$$C_a(\alpha, f) = \eta_e C_{n_\alpha} \alpha^2 \sqrt{f} \quad [3.25]$$

The separation point can be approximated using the steady normal force tables by rearranging Equation 3.24 to solve for f as a function of normal force and angle of attack. Beddoes (1984) showed that an expression for f can then be found by using a two function piecewise least-squares curve fit, Equation 3.26. The piecewise equation breaks at α_1, the angle of attack where $f = 0.7$. Figure 3.2 shows an example of the curve fitted to steady airfoil data for the S809 airfoil.

$$f = \begin{cases} 1 - 0.3e^{\left(\frac{\alpha-\alpha_1}{S_1}\right)}, & if\ \alpha < \alpha_1 \\ 0.04 + 0.66e^{\left(\frac{\alpha_1-\alpha}{S_2}\right)}, & if\ \alpha > \alpha_1 \end{cases} \quad [3.26]$$

Equation 3.26 was developed primarily for helicopter applications which typically use thinner airfoils than wind turbines. Gupta and Leishman (2006) suggested a three function piecewise fit (Equation 3.27) which often yields a better fit for wind turbine airfoils as shown in Figure 3.2. The second break point, α_2, is determined by the location of the second normal force break point, which corresponds to a dramatic break in the chord force. Figure 3.2 shows the associated lift and drag forces using Equation 3.27.

$$f = \begin{cases} c_1 + a_1 e^{S_1 \alpha}, & \alpha \le \alpha_1 \\ c_2 + a_2 e^{S_2 \alpha}, & \alpha_1 \le \alpha \le \alpha_2 \\ c_3 + a_3 e^{S_3 \alpha}, & \alpha_2 \le \alpha \end{cases} \quad [3.27]$$

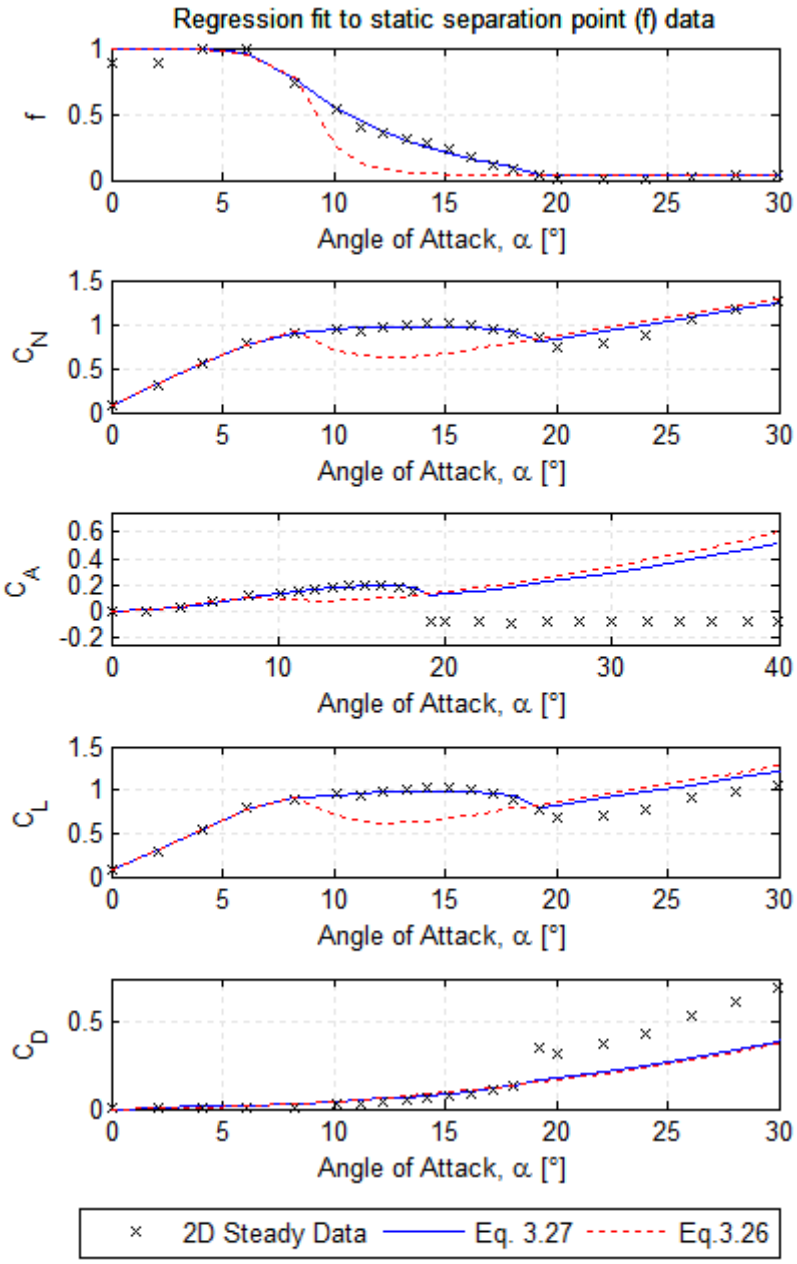

Figure 3.2: Example Kirchhoff and Helmholtz TE separation point curve fitting

The accuracy of the reconstructed forcing coefficient curve fits from the separation point fit is one of the most sensitive model consideration. It is critically important that the coefficients of normal and chord force are accurately predicted at angles of attack below the static stall angle because the trailing edge flow separation model has the largest contribution to lift and drag when leading edge flow separation has not occurred. Since leading edge flow separation typically only

occurs near the blade root, the trailing edge flow separation will dominate force predictions for the majority wind turbine blade, the majority of the time.

Since Equation 3.24 is based entirely on steady data, it does not account for unsteady dynamic effects. To determine the trailing edge separation point, the unsteady pressure response of the system must be determined. Since calculating the pressure gradient would be too computationally expensive, an effective lift is calculated, $C'_n(t)$, referred to as the ersatz lift parameter in the literature. It captures the overall effect of delayed flow separation as a result of pressure gradient dynamics. The ersatz lift parameter is calculated by applying a deficiency function to the steady lift, shown in Equations 3.28 and 3.29. In Equation 3.29, T_p is an empirically derived time constant determined by analyzing the leading edge pressure response. The ersatz lift parameter is also used in the leading edge flow separation module to determine the onset of dynamic stall, discussed in Section 3.4.

$$C'_{n_n} = C^p_{n_n} - D_{p_n} \qquad [3.28]$$

$$D_{p_n} = D_{p_{n-1}} e^{\left(\frac{-\Delta s}{T_p}\right)} + \left(C^p_{n_n} - C^p_{n_{n-1}}\right) e^{\left(\frac{-\Delta s}{2T_p}\right)} \qquad [3.29]$$

In Equation 3.30, the ersatz lift parameter is used to calculate an effective angle of attack where the steady leading edge pressure is equal to the unsteady case. An effective separation point *f'* is then calculated as a function of α_f using Equation 3.26 or 3.27.

$$\alpha_f(t) = \frac{C'_n(t)}{C_{n_\alpha}} \qquad [3.30]'$$

While *f'* models the pressure gradient, the unsteady boundary layer response must also be accounted for. In Equations 3.31 and 3.32, the unsteady trailing edge flow separation point is calculated by applying a deficiency function to the effective separation point. The time constant

T_f is also determined experimentally by examining the unsteady development of the boundary layer.

$$f_n'' = f_n' - D_{f_n} \quad [3.31]$$

$$D_{f_n} = D_{f_{n-1}} e^{\left(\frac{-\Delta s}{T_f}\right)} + \left(f_n' - f_{n-1}'\right) e^{\left(\frac{-\Delta s}{2T_f}\right)} \quad [3.32]$$

The unsteady normal and chord forces including trailing edge flow separation can finally be calculated using *f"* with the Kirchhoff and Helmholtz theory as shown in Equations 3.33 and 3.34.

$$C_{n_n}^f(t) = C_{n_\alpha}\left(\frac{1+\sqrt{f_n''}}{2}\right)^2 \alpha_{e_n} + C_{n_n}^{nc} \quad [3.33]$$

$$C_{a_n}(t) = \eta_e C_{n_\alpha} \sqrt{f''}\,\alpha \sin(\alpha) \quad [3.34]$$

3.4 Leading Edge Flow Separation

Experimental evidence has shown that dynamic stall is initiated at the leading edge through the development and separation of a vortical disturbance. Predicting leading edge flow separation is therefore an essential part of the L-B dynamic stall model.

Beddoes (1976, 1978, 1983) developed the criteria for predicting vortex shedding based on the pressure distribution at the leading edge. Analysis of the leading edge pressure gradient suggested that once a critical pressure is reached, leading edge separation begins. Beddoes assumed that the leading edge pressure can be correlated with the normal force on the airfoil. A critical normal force coefficient, C_{n1}, can then be defined whereby vortex shedding is initiated once exceeded. The ersatz normal force coefficient C'_n is used to check this criterion since it already contains the response of the pressure gradient. Therefore, when $C'_n > C_{n1}$, vortex shedding is initiated. Since experimental data for the unsteady pressure gradient is typically

unavailable, the critical normal force coefficient must be approximated by other means. Using the steady airfoil tables, either the maximum normal force before stall or the normal force corresponding to pitching moment stall can be used for C_{n1}.

After the flow separates, the Kirchhoff and Helmholtz formulation for chord force is no longer applicable. The critical normal force can therefore be used to check if the flow has separated and modify the chord force expression. Leishman and Beddoes (1986, 1989) introduced the piece-wise formulation shown in Equation 3.35 where Φ is defined by Equation 3.36. The variables D and F are constants equal to 2 and 1 respectively.

$$C_{a_n}(t) = \begin{cases} \eta_e C_{n_\alpha} \sqrt{f''} \alpha \sin(\alpha), & C_n' \le C_{n_1} \\ \eta_e C_{n_\alpha} \sqrt{f''} f''^{\phi} \alpha \sin(\alpha), & C_n' > C_{n_1} \end{cases} \quad [3.35]$$

$$\phi = D\left(C_n' - C_{n_1}\right) + E\left(f'' - f\right) \quad [3.36]$$

The vortex begins forming prior to separation, after which it is convected down the airfoil into the wake. While it is in the vicinity of the airfoil, it can be viewed as additional circulation that results in a contribution to lift. Leishman and Beddoes (1986) assumed that the instantaneous contribution to accumulated vortex induced normal force can be approximated by the difference between the linearized unsteady circulatory normal force and the nonlinear lift determined using the Kirchhoff and Helmholtz theory, shown in Equation 3.37 and 3.38.

$$C_{v_n} = C_{n_n}^c \left(1 - K_{n_n}\right) \quad [3.37]$$

$$K_{n_n} = \frac{\left(1 + \sqrt{f_n''}\right)}{4} \quad [3.38]$$

Until the vortex has passed beyond the airfoil and into the wake, it can continue to accumulate lift. However, due to viscous forces and turbulent mixing, the vortex decays.

Equation 3.39 gives the total instantaneous normal force from the vortex, which decays the previous strength while adding additional increments if unsteadiness causes the vortex to continue to grow. The vortex normal force time constant, T_v, is an empirically derived constant that controls the rate of vortex decay.

$$C_{n_n}^v = C_{n_{n-1}}^v e^{\left(\frac{-\Delta s}{T_v}\right)} + \left(C_{v_n} - C_{v_{n-1}}\right) e^{\left(\frac{-\Delta s}{2T_v}\right)} \qquad [3.39]$$

The vortex contributes significantly to the overall normal force so its location is monitored using τ_v, the non-dimensional vortex time parameter in semi-chords. The vortex time parameter equals zero while forming at the leading edge and at the instant of separation. At the trailing edge, τ_v equals T_{vl}, the empirically derived, non-dimensional time necessary for the vortex to convect down the airfoil. Beddoes (1976) observed that the vortex travels at $⅓$ to $½$ the free stream velocity. This is expressed non-dimensionally in semi-chords in Equation 3.40, recalling that Δs is the change in the non-dimensional distance travel by the airfoil in semi-chords.

$$\tau_{v_n} = \tau_{v_{n-1}} + 0.45\Delta s \qquad [3.40]$$

Under leading edge separated flow, τ_v continues to increase until flow reattaches, at which point it is returned to zero. For flow reattachment to occur, several criteria must be met: the ersatz normal force parameter must fall below the critical coefficient of normal force, the angle of attack must be decreasing, and the vortex must have passed the trailing edge. These criteria are summarized below.

$$C_n' < C_{n_1}$$
$$\Delta\alpha < 0$$
$$\tau_v > T_{vl}$$

With the contribution of vortex lift calculated, the total unsteady coefficient of normal force can be calculated by superposition. Equation 3.41 shows that the total normal force is the

combination of the non-circular normal force under attached flow, the circular normal force with trailing edge flow separation, and the induced normal force of the vortex. This allows the model to be applicable under unsteady forcing conditions for attached flow, trailing edge flow separation, and dynamic stall.

$$C_{n_n} = C_{n_n}^{nc} + C_{n_n}^{f} + C_{n_n}^{v} \quad [3.41]$$

Using the relations in Equations 2.1 and 2.2, the coefficients of lift and drag can then be found, shown in Equations 3.42 and 3.43 where C_{d0} is the coefficient of drag when the steady C_l=0.

$$C_{l_n} = C_{n_n}\cos(\alpha_n) + C_{a_n}\sin(\alpha_n) \quad [3.42]$$

$$C_{d_n} = C_{n_n}\sin(\alpha_n) - C_{a_n}\cos(\alpha_n) + C_{d_0} \quad [3.43]$$

3.5 Subsystem Interaction

When dynamic changes in the pressure and velocity gradients occur, they propagate through the entire flow field. This leads to couplings between the different subsystems outlined in Sections 3.2 to 3.4. Leishman and Beddoes (1986, 1989) and Leishman (1988) accounted for these interactions by modifying the empirical time constants at certain stages of the dynamic stall process. Section 3.5.1 describes modifications to previous equations to allow time constant modification and Section 3.5.2 provides the algorithmic logic for changing the time constants.

3.5.1 Adapted equations for time constant modification

To keep the model generalized for a wide range of application, only the boundary layer response time constant T_f and the vortex normal force time constant T_v are modified. To accomplish this, the exponentials in the deficiency functions using these time constants are raised to powers determined by the logic outlined in Section 3.5.2. Two indices are used as the power of the exponentials, σ_1 and σ_3. An additional index σ_2 was used in early implementations of the L-

B model so the numbering σ_1 and σ_3 is still used for consistency with the legacy notation. Equation 3.32 from the trailing edge flow separation model is redefined as Equation 3.44 where E_f and E_f^l are defined by Equations 3.45 and 3.46 respectively.

$$D_{f_n} = D_{f_{n-1}} E_f + \left(f_n' - f_{n-1}' \right) \sqrt{E_f^l} \quad [3.44]$$

$$E_f = e^{\left(\frac{-\Delta s}{T_f} \right)} \quad [3.45]$$

$$E_f^l = \left(E_f \right)^{\sigma_1} \quad [3.46]$$

To determine vortex lift, Equation 3.39 is similarly redefined by Equations 3.47 to 3.49.

$$C_{n_n}^v \left(t \right) = C_{n_{n-1}}^v E_v^l + \left(C_{v_n} - C_{v_{n-1}} \right) \sqrt{E_v^l} \quad [3.47]$$

$$E_v = e^{\left(\frac{-\Delta s}{T_v} \right)} \quad [3.48]$$

$$E_v^l = \left(E_v \right)^{\sigma_3} \quad [3.49]$$

3.5.2 Logic for time constant modification

The logical hierarchy for modifying σ_1 and σ_3 was summarized by Leishman (2011). Modifications to σ_1 are based primarily on whether trailing edge flow is separating or reattaching. Table 3.1 contains the hierarchy of logic checks for separating flow and Table 3.2 covers the logic checks for reattaching flow. The tables are structured sequentially such that when a logic check passes, it overrides the previous value.

Table 3.1: Time constant logic for separating trailing edge flow, $f''_n<f''_{n-1}$

Criteria	Modification	Physical Justification
$C'_{n_n} \le C_{n_1}$	$\sigma_1 = 1$	The default value for separating flow.
$C'_{n_n} > C_{n_1}$	$\sigma_1 = 1.75$	Leading edge flow separation has begun resulting in accelerated trailing edge separation point movement.
$f''_{n-1} \le 0.7$	$\sigma_1 = 2$	If the flow separation point is less than the position x/c = 0.7, further separation occurs very quickly.
$K_\alpha < 0$	$\sigma_1 = 2$	When the angle of attack is decreasing yet trailing edge flow separation is still occurring, the boundary layer time constant is relaxed to allow rapid reorganization of the boundary layer.

Table 3.2: Time constant logic for reattaching trailing edge flow, $f''_n>f''_{n-1}$

Criteria	Modification	Physical Justification
$C'_{n_n} \le C_{n_1}$	$\sigma_1 = 0.5$	The default value for reattaching flow.
$0 \le \tau_v \le T_{vl}$	$\sigma_1 = 0.25$	Restricts trailing edge flow reattachment if the vortex is in the process of shedding.
$K_\alpha > 0$	$\sigma_1 = 0.75$	When the angle of attack is increasing yet trailing edge flow reattachment is still occurring, the boundary layer time constant is relaxed to allow rapid reorganization of the boundary layer.

To modify the rate of vortex formation and decay, modifications are made to σ_3. Table 3.3 outlines the hierarchy of logic checks that override previous values.

Table 3.3: Time constant logic governing vortex formation and decay

Criteria	Modification	Physical Justification
$T_{vl} \le \tau_v \le 2T_{vl}$	$\sigma_3 = 3$	After the vortex passes the trailing edge, it decays more rapidly.
$f''_n > f''_{n-1}$	$\sigma_3 = 4$	If flow is reattaching, vortex decay further increases.
$0 \le \tau_v \le T_{vl}$	$\sigma_3 = 1$	The default value, used during vortex shedding.
$0 \le \tau_v \le T_{vl}$ $K_\alpha < 0$	$\sigma_1 = 2$	If the vortex is shedding but angle of attack is decreasing, then vortex decay is increased.
$K_\alpha < 0$	$\sigma_3 = 4$	If the previous four conditions do not apply, but angle of attack is decreasing, experimental evidence suggests that the vortex decays very rapidly.
$f''_n > f''_{n-1}$ $K_\alpha < 0$	$\sigma_3 = 1$	The default value, used when flow is reattaching and angle of attack is decreasing.

CHAPTER 4

DYNAMIC STALL MODEL IMPLEMENTATION AND 2D VALIDATION

4.1 Model Development

A Beddoes-Leishman dynamic stall model was developed in Matlab using the theory outlined in Chapter 3. The model was written to replace the use of 2D look-up tables during time marching simulations in WInDS, using wind speed and angle of attack at a given blade node and outputting C_l and C_d. An initialization step at the beginning of simulations calculates relevant model coefficients from the 2D steady airfoil data and uses the same Matlab variables and data structures as WInDS. While the model was written specifically for coupling with WInDS for 3D simulations, it can also be used as a standalone 2D model using a driver script to provide the inputs for time marching simulations.

Table 4.1 gives the default indicial coefficients and time constants that were used for all subsequent sections. The indicial coefficients, A_1, A_2, b_1, and b_2, were defined by Leishman and Beddoes (1986) and the time constants T_p, T_f, T_v, and T_{vl}, were defined by Gupta and Leishman (2006). While the user has the option to change these constants, they should not be considered tunable parameters. When available, airfoil specific time constants should be used, derived using system identification techniques for periodically unsteady experimental data.

Table 4.1: Empirical coefficients inherent to the model

T_p	T_f	T_v	T_{vl}	A_1	A_2	b_1	b_2
1.7	3.0	6.0	11.0	0.3	0.7	0.14	0.53

The user has the option to select the TE separation point model, either Equation 3.26 or 3.27, and to display the fits to the 2D steady data. Using the three function fit from Equation 3.27 tends to provide better results for the thick airfoils typically used for wind turbine applications,

however Equation 3.26 may occasionally work better for thin airfoils outboard on the blade. It is essential that the user verifies the fitness of the steady TE separation point model in order to achieve accurate results.

4.2 Experimental Data Set

Two-dimensional, oscillating experimental data are available through NREL from wind tunnel tests conducted at The Ohio State University (OSU) Aeronautical and Astronautical Research Laboratory. One of the specific goals of the experiments was to examine the dynamic stall behavior of thick airfoils representative of those used on wind turbine blades. For a given test, an airfoil was oscillated at a constant frequency and the aerodynamic forces were recorded. This was repeated over a range of reduced frequencies, mean values for angle of attack, amplitudes of angle of attack, and Reynolds numbers for several airfoils. The details for the experimental setup can be found in Ramsay et al. (1995), and the relevant modelling parameters are summarized in Table 4.2.

Table 4.2: Summary of OSU modelling parameters

Chord, c (m)	0.457
Reynolds number, Re ($x10^6$)	0.75, 1.0, 1.25, 1.4
Angle of attack pitch amplitude, α_{amp} (°)	5.5, 10
Mean angle of attack, α_{mean} (°)	8, 14, 20
Pitch reduced frequency, k	0.026, 0.053, 0.78

OSU experimental conditions were replicated to validate the functionality of the dynamic stall model. Steady airfoil data from the OSU wind tunnel were also used for consistency. Representative sample results for the S809 airfoil are presented in this section. The S809 was selected since it is also used in the experimental data set presented in Section 5.2. Results for additional test cases can be found in Appendix A. Table 4.3 shows the coefficients calculated during model initialization for the steady airfoil data at different Reynolds numbers. Figure 3.2 shows fits to the steady airfoil data using the coefficients in Table 4.3 for $Re = 1.0 \times 10^6$. Again,

it is important to note that accuracy model predictions are highly dependent on the accuracy of Kirchhoff/Helmholtz trailing edge flow separation fits at low angles of attack.

Table 4.3: Model coefficients calculated from steady data

Re	**7.5 x 10^5**	**1.0 x 10^6**	**1.25 x 10^6**
C_{n_α} [rad^{-1}]	7.150	6.684	6.864
C_{n_1}	0.9702	1.0093	1.1376
C_{n_2}	2.1840	2.1815	2.2754
C_{d_0}	0.0017	0.0017	0.0010
α_0 [°]	0.905	0.908	0.927
α_1 [°]	8.07	8.57	7.98
α_2 [°]	17.1	18.1	18.2
c_1	1.0	1.0	1.0
c_2	0.0268	-0.0999	-0.0937
c_3	0.0178	0.0304	0.0225
a_1	-0.107	-2.51 x 10^{-4}	-0.0022
a_2	3.824	2.680	2.387
a_3	2.409 x 10^7	1.875 x 10^{11}	1.659 x 10^{11}
S_1	4.519	47.723	35.022
S_2	-12.367	-8.193	-8.006
S_3	-65.562	-91.746	-91.279

4.3 Selection of the Critical Normal Force Coefficient

When comparing model performance to the experimental data, chord force is not accurately predicted using Equation 3.35. The transition to the post stall expression is highly sensitive to the value selected for the critical normal force. Furthermore, C_{n1} is a variable in the post stall expression so a poorly selected value causes erroneous results. Using the maximum steady normal force for C_{n1} yields accurate results for unsteady normal force, but causes preemptive transition to the post stall expression for chord force. Sensitivity analysis shows that higher values for C_{n1} give better results for chord force but overpredict normal force due to

unrealistically delaying separation of the leading edge vortex. It is clear that an alternate criteria is needed for chord force.

Under steady conditions, the maximum normal force occurs soon after the first break point α_1. Figure 3.2 however, shows that the expression for chord force using the Kirchhoff/ Helmholtz theory holds for high angles of attack until the second break point α_2 is reached. Rather than using the onset of leading edge flow separation as the criteria, a second critical normal force C_{n2} corresponding to α_2 is used. Since the ersatz normal force, C'_n, is the pressure lagged potential normal force under thin airfoil theory, C_{n2} is calculated using thin airfoil theory where $\alpha = \alpha_2$, shown in Equation 4.1. Equation 3.35 is then modified to give Equation 4.2.

$$C_{n_2} = C_{n_\alpha}\alpha_2 + C_{n_0} \qquad [4.1]$$

$$C_{a_n}(t) = \begin{cases} \eta_e C_{n_\alpha}\sqrt{f''}\alpha\sin(\alpha), & C_n' \le C_{n_2} \\ \eta_e C_{n_\alpha}\sqrt{f''}f''^{\phi}\alpha\sin(\alpha), & C_n' > C_{n_2} \end{cases} \qquad [4.2]$$

Figure 4.1 shows an example of chord force using C_{n1} and C_{n2} as the criteria compared to OSU experimental data. This test case uses the S809 airfoil where Re = 1.0×10^6, k = 0.078, $\alpha_{amplitude}$ = 10°, and α_{mean} = 14°. The critical normal forces are C_{n1} = 1.0093 and C_{n2} = 2.1815. Both methods initially predict the same chord force using the pre-stall Kirchhoff/ Helmholtz expression. However, using C_{n1} results in an early transition to the post-stall expression and delayed transition back as angle of attack decreases. This causes significant under prediction of chord force and over prediction of drag compared to the experimental data. Using C_{n2} provides an excellent fit, although negative chord forces shown in the experimental data are over predicted because Equations 3.35 and 4.2 yield positive result for $0° \le \alpha \le 180°$.

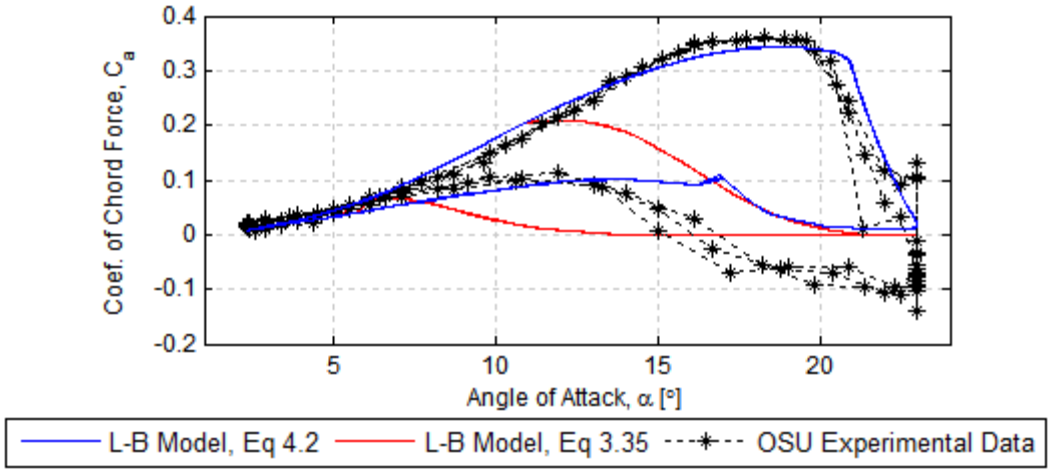

Figure 4.1: Sample results for chord force and drag using Eq. 3.35 and 4.2

4.4 Model Validation against 2D Data

S809 airfoil test cases are modeled in which Re = 1.0×10^6, k = [0.026, 0.04, 0.078], $\alpha_{amplitude}$ = 10°, and α_{mean} = [8, 14, 20]°. Three to four pitching cycles are available for each OSU test case. A sine wave is fit to OSU angle attack data and used as the input for the model, since the OSU experiments were designed to only excite a single frequency at a time. Figure 4.2 shows minor deviations from a pure sine wave, which could account for some of differences between the model performance and the OSU data near peak angle of attack. The OSU data also shows some cycle-to-cycle variability for the aerodynamic loads, largely attributed to turbulence under detached flow. Figures 4.3 to 4.8 compare model results against the experimental data, showing the coefficients lift and drag plotted against angle of attack.

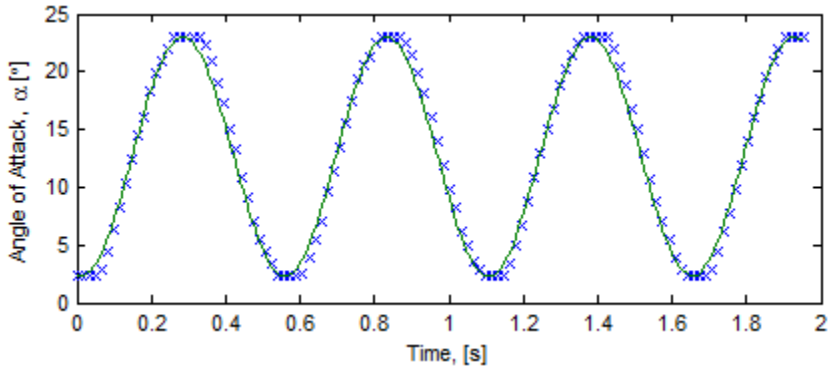

Figure 4.2: Example sine wave fit to OSU angle of attack data

In Figure 4.3, 4.4, and 4.5, both the model and experimental results show typical dynamic stall lift hysteresis. Stall is delayed while the angle of attack is increasing, resulting in greater lift compared to the steady data. Reattachment is also delayed when the angle of attack is decreasing, resulting in less lift than predicted by the steady data. The hysteresis is more pronounced for higher reduced frequencies and approaches the steady case for lower reduced frequencies. The most consistent deviation from the experimental data is the overprediction of lift when angle of attack is decreasing and flow has not yet reattached, exhibited across all cases. Additionally, for α_{mean} = 8° and 14°, lift is overpredicted for high angles of attack while angle of attack is increasing.

The unsteady drag response to periodic pitching is much closer to the steady case than the lift model. Drag follows the steady data almost exactly until flow separates, highlighting the importance of predicting the point of transition to the post stall formulation of chord force. The model fits the drag data well, although peak drag is under predicted when α_{mean} = 8° and transient spikes are not predicted for deep stall when α_{mean} = 14°.

Overall, the model results agree with the experimental data well and are comparable to results obtained by Gupta and Leishman (2006). When comparing the model results to the experimental data, it should be kept in mind that the LB method is a parsimonious approach. Rather than model the full pressure and velocity response of the flow field, simplified physics and sensitive experimental coefficients are used model the overall progression of the flow. This provides reasonable approximations to the unsteady behavior that are significantly better than using steady table look-ups. Due to inherent simplifications and assumptions in this technique, the full dynamic response of the system cannot be captured such as transient peaks in response to turbulence.

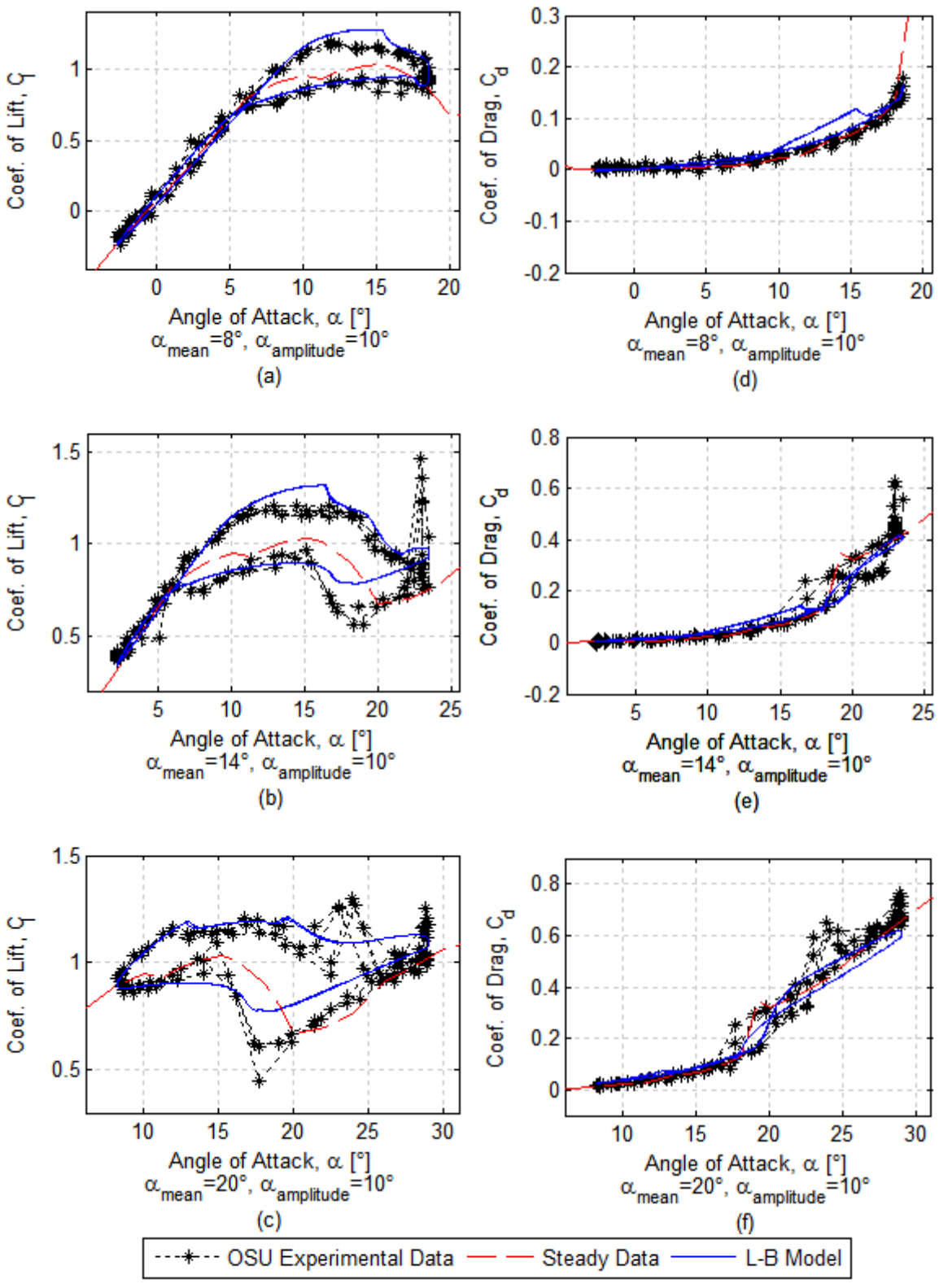

Figure 4.3: C_L and C_D for the S809 Airfoil with time varying α, k = 0.026, Re = 1.0×10^6

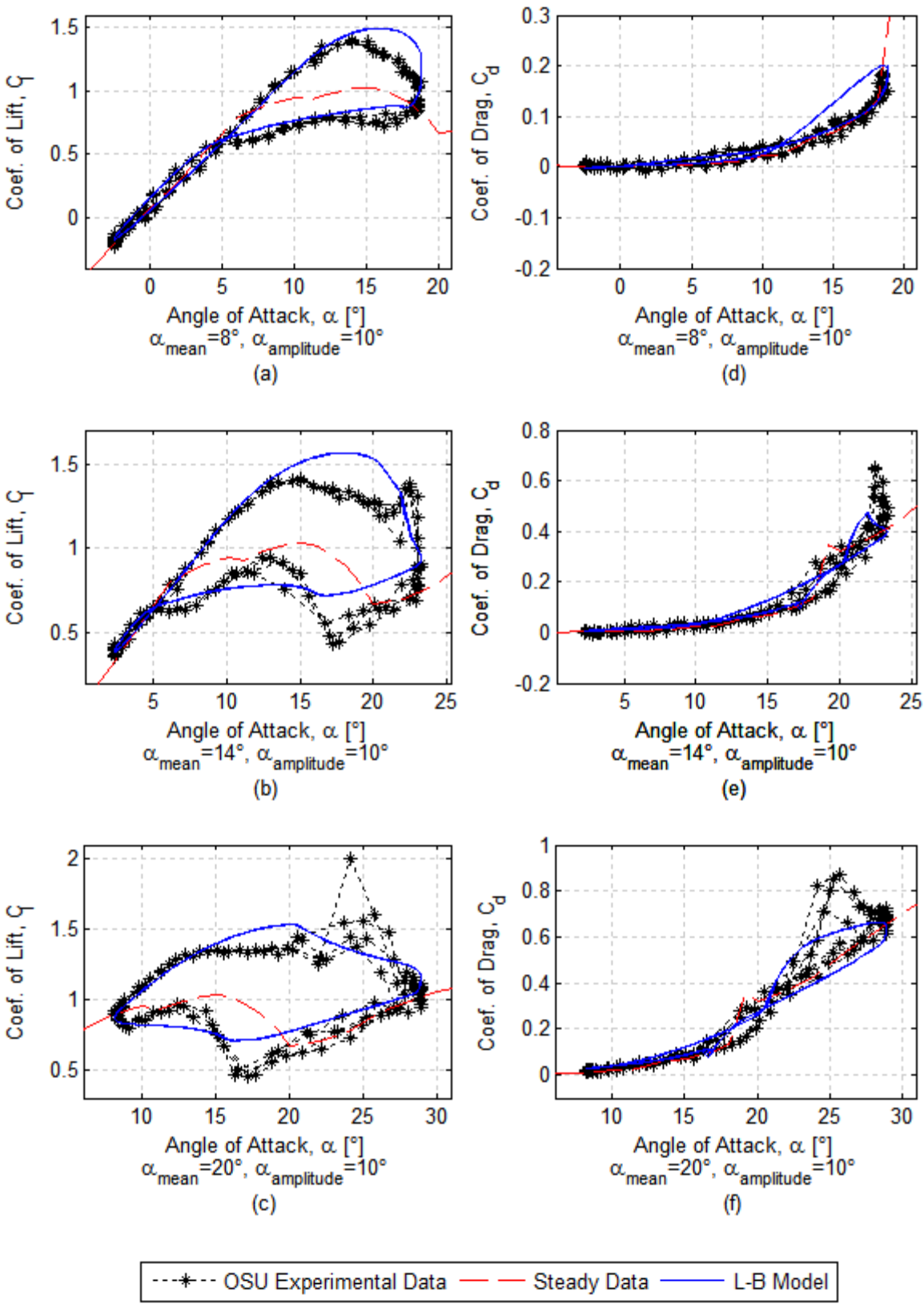

Figure 4.4: C_L and C_D for the S809 Airfoil with time varying α, k = 0.053, Re = 1.0×10^6

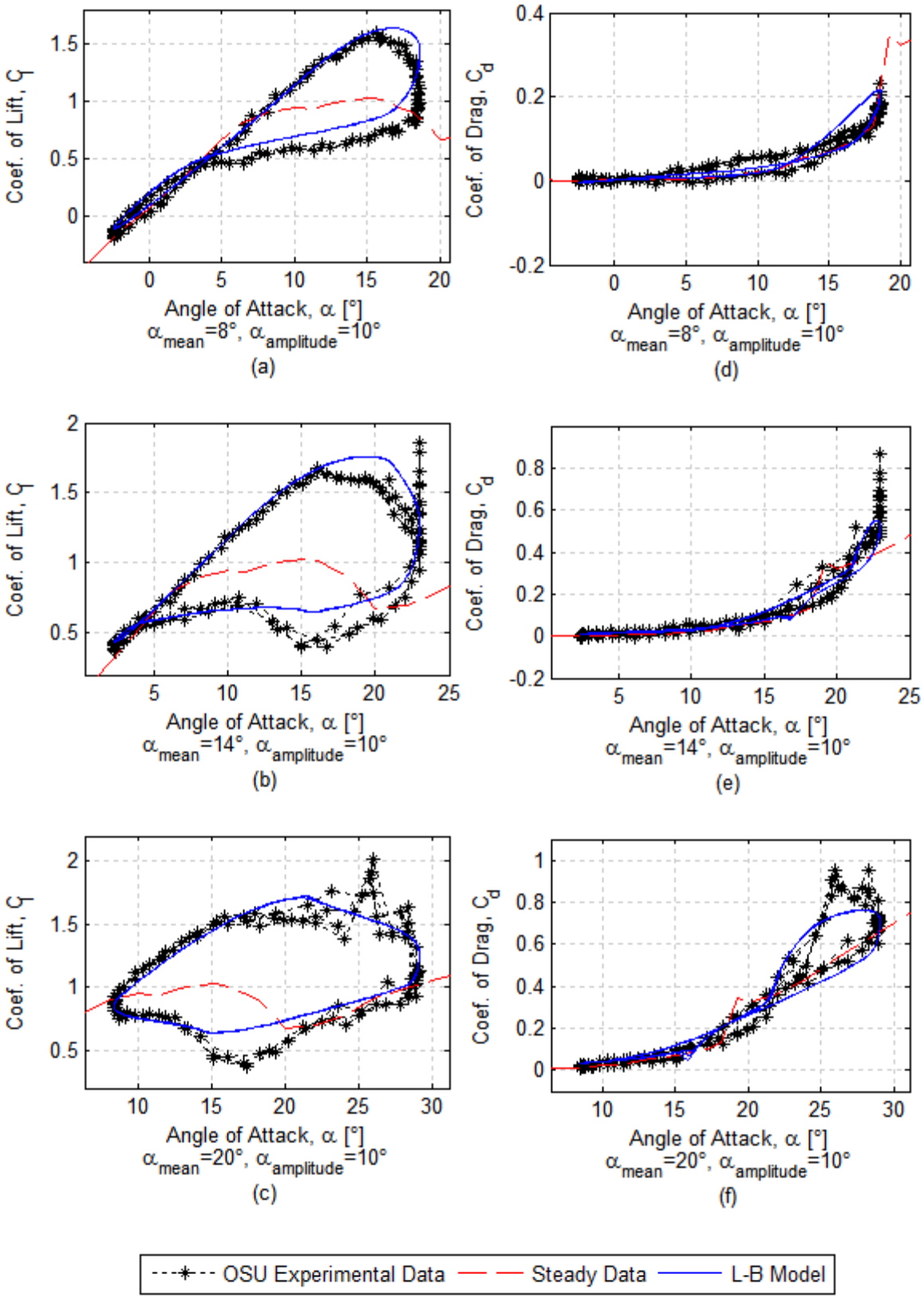

Figure 4.5: C_L and C_D for the S809 Airfoil with time varying α, k = 0.078, Re = 1.0×10^6

CHAPTER 5

DYNAMIC STALL COUPLED WITH WInDS

5.1 Model Integration

Accurate prediction of lift along the blade span is essential to the utility of WInDS. Bound circulation strength, Γ, is calculated using the instantaneous lift according to the Kutta-Joukowski theorem, Equation 2.9, at nodes along the blade for every time step. According to Kelvin's circulation theorem, circulation in the domain cannot change with time. Therefore changes in the instantaneous bound circulation strength cause equal and opposite vorticity to be shed into the wake and convected downstream. Using the Biot-Savart law, the wake induction changes the velocity field at the blade, affecting the instantaneous angle of attack and thus lift and bound vorticity.

WInDS uses fixed point iteration for root finding to solve the coupling between bound vortex filament circulation strength and wake induction. Algorithm 2 developed by Sebastian (2012) summarizes the fixed point iteration scheme used by WInDS.

Algorithm 2: Fixed-Point Iteration in WInDS

Data: Turbine geometry and wake properties
Results: Updated bound circulation strength

1 **while** $\Delta\Gamma_{bound} \geq tolerance$
2 Use Biot-Savart law to compute induced velocities on the lifting-ling due to influence of bound and wake filaments
3 Compute span-wise angles of attack from induced velocities
4 Compute/table look-up C_l and C_d
5 Compute new bound circulation strength via Kutta-Joukowski theorem
6 Multiply difference between old and new bound circulation strengths by a relaxation factor. "Relaxed" update is applied to bound circulation strength
7 Update shed and trailed filaments to satisfy Kelvin's theorem

The WInDS source code was modified to include the dynamic stall model, which the user has the option of turning on or off. When in use, the L-B model replaces 2D aerodynamic table look-ups at Step 4 during fixed point iteration. The outputted coefficient of lift from the L-B

model is used directly by WInDS to calculate bound circulation strength using the Kutta-Joukowski theorem, and distributed lift and drag are used to calculate global model performance metrics such as total rotor thrust, torque, and power. Several modifications were required to prevent stability and accuracy problems once the L-B model was integrated into WInDS.

By combining the L-B dynamic stall model with a free vortex wake model, induced forces from shed vortices are effectively double counted as discussed by Coton et al. (2002). The L-B method includes induced forces on the airfoil by the LE vortex as it forms and then separates and convects downstream. Similarly, WInDS uses the Biot-Savart law to induce a velocity field on the blade from shed vortex filaments in the wake. Since the L-B model includes blade scale unsteady viscous effects that WInDS cannot model, it is the more useful approach. The problem is resolved by not including the shed vortices from a given node when applying the Biot-Savart law to calculate the induced velocity on that bound node. All trailing vortices and the shed vortices from all other nodes still induce forces on the given node.

Use of the dynamic stall model could also cause stability problems during fixed-point iteration due to the piece-wise axial force model, Equation 4.2. On very rare occasions, the solution for C'_n is very close to C_{n2} for a given blade node and time step. As fixed point iteration gradually approaches this value, it can trigger a change in the axial force expression being used, for example C'_n was less than C_{n2} but is now greater. Changing expressions for axial force caused a cascade of non-linear changes to propagate in the next iteration. The subsequent angle of attack change can cause C'_n to again become less than C_{n2}, resulting in a loop where the convergence criteria is never met. The dynamic stall model was modified to detect this behavior and force the model to use the pre-stall expression for axial force when it arises, as it is the more stable of the two expressions. This is a very rare occurrence so there is a negligible effect on the overall model performance.

In general, coupling two dynamic models causes convergence of the fixed point iteration to be more sensitive. For test cases that are highly unsteady, such as those with rotor yaw or platform motion, smaller relaxation factors must be used for stability, approximately 0.05 to 0.20. An optional feature was added to WInDS that tunes the relaxation factor at the beginning of a simulation to find a stable operating point. This feature should be used with care, however, as in some cases it chooses unnecessarily small relaxation factors, resulting in significantly longer simulation run times and potentially prevents true convergence before the maximum number of iteration is reached. Tuning occurs at the first time step, but future work could allow for dynamic relaxation factor tuning throughout the simulation to increase stability and reduce simulation run time or employ more robust root finding techniques.

5.2 Model Validation against 3D Experimental Data

5.2.1 Experimental data set

Experimental data from Phase VI of the NREL Unsteady Aerodynamic Experiment (UAE) was used to validate WInDS. The testing campaign used a fully instrument wind turbine in controlled conditions in the 24.4 m x 36.6 m wind tunnel at the NASA Ames Research Center. Full details about the experimental setup and available data can be found in Hand, et al. (2001).

Sequence S data was used for validation. These used steady wind speeds between 5 m/s and 25 m/s with 0° to 180° yaw error. The turbine has a 10 m rotor, upwind with two blades, at a constant pitch of 3° and 0° pre-coning. Booms extending off the blades to measure incident flow angles were removed for this test sequence so the flow was minimally disturbed by instrumentation. Aerodynamic forces were determined by integrating measurements at chord-wise distributed pressure taps at blade span (r/R) locations 0.3, 0.466, 0.633, 0.80, and 0.95.

Appendix B contains diagrams of the UAE test rotor blades and distributed blade properties in Table B.1. The blades use the S809 airfoil from span locations 0.267 to 1. OSU

steady airfoil data at $Re = 0.75x10^6$ was used for the S809, shown in Table B.2 in Appendix B from Hand, et al. (2001). The blades transition from a cylinder to the S809 from 0 to 0.267 span. This part of the blade cannot be modelled because there are no available airfoil data for the transitional sections.

5.2.2 Results: Steady wind

Data is available for the UAE rotor for steady wind speeds of 7, 10, 13, 15, 20, and 25 m/s and 0° yaw angle. Modelling was performed using WInDS with and without the dynamic stall model and with FAST. FAST is a widely used and accepted aero-elastic design code in industry, used for IEC certification testing, so it is included to depict typical disparities between model predictions and experimental data. Further examples of model performance against this data set are provided in Simms, et al. (2001), which was a blind model comparison against UAE Sequence S data. The FAST model for the UAE rotor is distributed with FAST as Certification Test 10. Model results for span distributed coefficients of normal and axial force, thrust and torque on a single blade, and the total aerodynamic rotor power were compared to the UAE data.

Figure 5.1 compares the span-wise distributed average coefficients of normal and axial force for several wind speeds. WInDS tends to underpredict the coefficient of normal force near the blade root and overpredict near the tip. The predictions at the 0.3 span location are particularly poor. This is likely caused by not modelling the transitional airfoils below 0.267, causing unrealistic behavior near the root. The coefficients of normal force with and without dynamic stall are approximately equal up to 15 m/s. For 20 m/s and 25 m/s, using dynamic stall significantly improves predictions at most blade locations. This can be attributed to the average angle of attack, shown in Figure 5.2, where solid and dashed lines represent WInDS with and without dynamic stall respectively. Since the blades are at fixed pitch angles, the turbine operates at high angles of attack at high wind speeds, especially near the blade root. The dynamic stall model is better able to predict the normal force post stall than when using steady data.

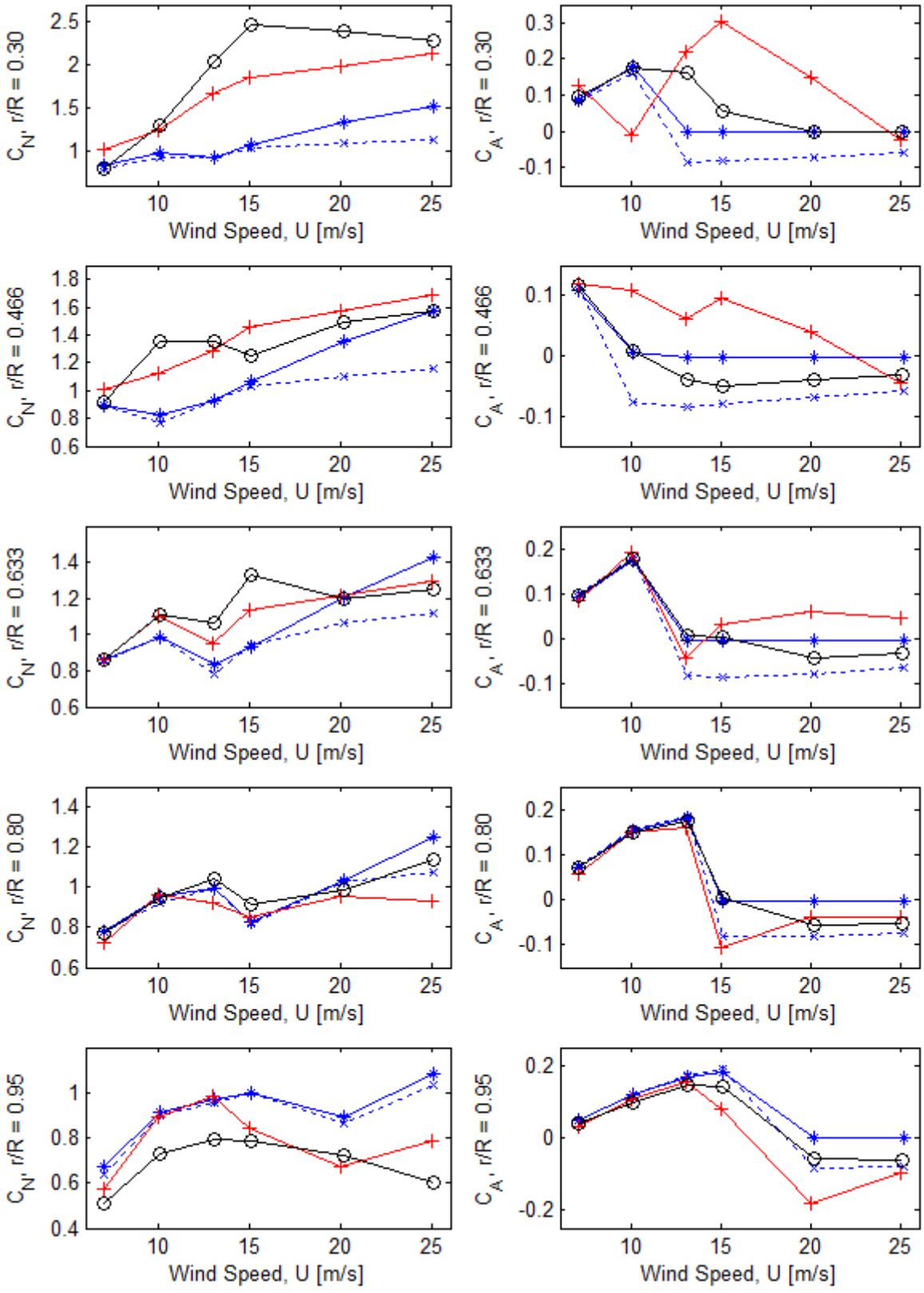

Figure 5.1: Average blade span distribute C_N and C_A for steady wind

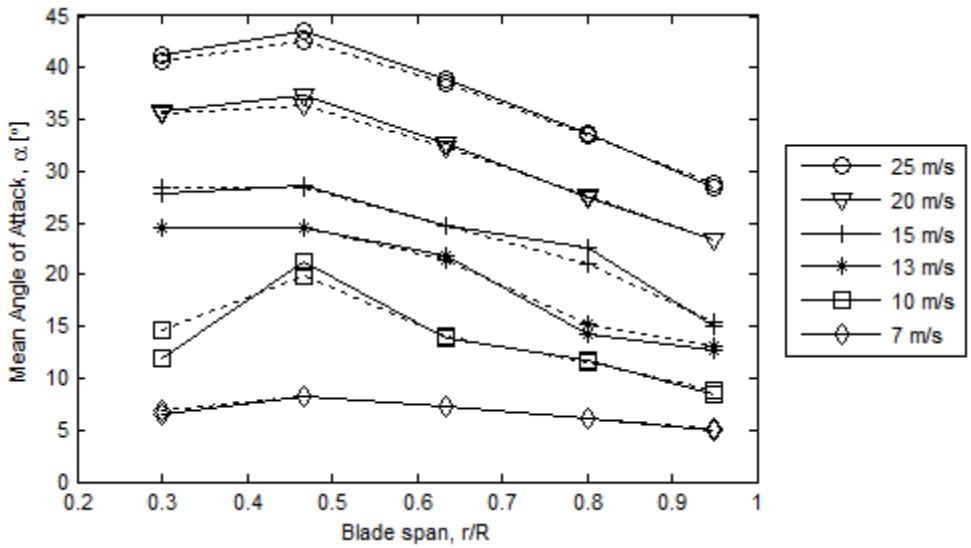

Figure 5.2: Average blade span distributed angle of attack predicted by WInDS for steady wind;

Solid lines for WInDS with D.S., Dashed lines for WInDS without D.S.

Predictions by WInDS for the coefficient of axial force match the experimental data quite well. Similar to normal force, there are insignificant differences between WInDS with and without the dynamic stall model for attached flow conditions. Post-stall however, using dynamic stall tends to overpredict axial force, while the base version of WInDS underpredicted. This can be attributed to the inability of the dynamic stall axial force model to predict forces less than zero.

Figure 5.3 shows the average torque and thrust per blade as well as the average rotor power. Table 5.1 summarizes the percent error between model predictions and the experimental data. Thrust is calculated quite well despite difficulties predicting the span wise coefficients of normal force, over and under predictions average out to approximately the correct solution. Improvements in predicting the coefficient of normal force using the dynamic stall model in post stall conditions are reflected in the thrust data where prediction error decreases by 8.9% and 13.1% for 20 m/s and 25 m/s respectively. The torque per blade and rotor power are significantly underestimated by WInDS without the dynamic stall model as a result of consistently under

predicting the coefficient of axial force. Using the dynamic stall model reduces prediction error of torque per blade by 18-40% and rotor power by 19-64% for wind speeds greater than 10 m/s.

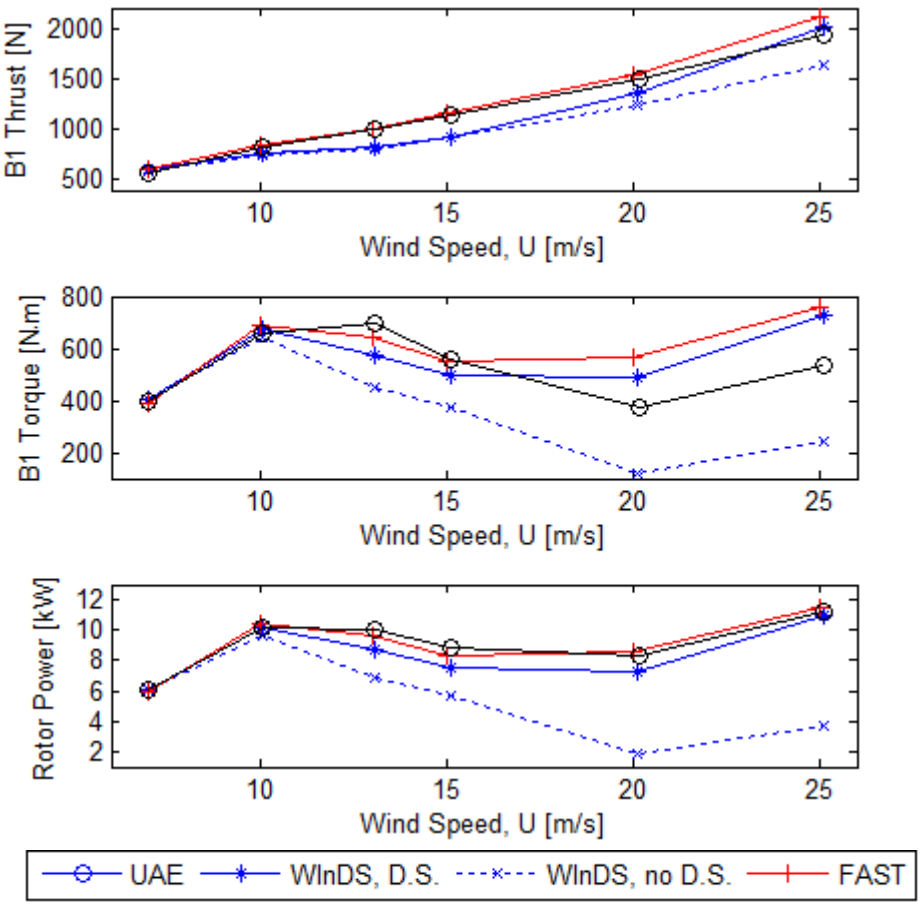

Figure 5.3: Average thrust and torque per blade and total aerodynamic rotor power for steady wind

Table 5.1: Average percent error between model predictions and UAE data for steady cases

		Wind Speed [m/s]					
		7	10	13	15	20	25
Blade 1 Thrust	WInDS (%)	1.37	-10.70	-19.00	-18.02	-17.63	-15.87
	WInDS, D.S. (%)	4.04	-8.07	-16.96	-18.21	-8.77	3.56
	Improvement with D.S. (%)	-2.67	2.63	2.04	-0.20	8.86	12.31
Blade 1 Torque	WInDS (%)	1.90	-2.60	-33.44	-32.45	-68.28	-54.46
	WInDS, D.S. (%)	2.08	2.16	-14.81	-10.52	27.38	35.33
	Improvement with D.S. (%)	-0.18	0.43	18.63	21.92	40.89	19.14
Rotor Power	WInDS (%)	1.65	-5.68	-32.69	-37.28	-74.56	-67.76
	WInDS, D.S. (%)	0.10	-1.17	-13.64	-16.62	-10.66	-3.79
	Improvement with D.S. (%)	1.54	4.51	19.05	20.66	63.89	63.96

There is a discrepancy in the torque and power trends for the UAE data in Figure 5.3. This is a result of different measuring techniques being employed, both with inherent weaknesses. The torque data is the estimated aerodynamic torque for the instrumented blade, determined by integrating the pressure at taps distribute along the blade. The rotor power was determined by measuring the torque on the low speed shaft using a strain gauge. While both turbine blades had the same shape and airfoil distribution, the blades had different weights as a result of one being heavily instrumented, causing the rotor to be unbalanced. Furthermore, the instrumented blade had additional roughness due to the pressure taps, potentially changing its stall behavior and causing the two blades to have different loading profiles. This caused significant cyclical loading on the low speed shaft, combined with cyclical gravity loads, which are reflected in the strain gauge measurements. The estimated blade torque from the pressure data was used for comparisons with model predictions because these cyclical loads are not present. Rotor power measured by the low speed shaft strain gauge was used because loading on the non-instrumented blade is unknown and it is not safe to assume it was the same as the instrumented blade.

5.2.3 Results: Unsteady aerodynamics from rotor yaw

Unsteady aerodynamic loading is modelled for UAE Sequence S test cases with steady wind and non-zero rotor yaw. Rotor misalignment with the wind causes sinusoidal variations in the angle of attack as the blades move towards and away from the wind, which can produce dynamic stall. Table 5.2 summarizes the unsteady angle of attack variations for various yaw test cases as calculated by WInDS with the dynamic stall model. Due to the velocity profile and chord distribution along the blade, the reduced frequency increases near the blade root and slightly with increased yaw angles. Higher wind speeds reduce the unsteadiness as a result of a larger proportion of the velocity from the free stream wind rather than the rotor rotation. Most

importantly, higher yaw angles cause larger amplitude angle of attack oscillations resulting in a more dramatic dynamic stall response.

Table 5.2: Unsteady variations in angle of attack for UAE Sequence S yawed cases calculated by WInDS with dynamic stall

r/R	Wind Speed [m/s]	10			13		15		
	Yaw Angle [°]	10	30	60	10	30	10	30	60
0.30	Reduced frequency, k	0.183	0.184	0.192	0.159	0.164	0.148	0.154	0.157
	Mean angle of attack, α_{mean} [°]	13.1	13.4	6.9	24.3	20.6	27.2	24.0	21.6
	Angle of attack amp., α_{amp} [°]	3.5	11.0	14.9	5.0	16.5	5.5	17.3	40.4
0.47	Reduced frequency, k	0.118	0.118	0.121	0.108	0.110	0.102	0.104	0.109
	Mean angle of attack, α_{mean} [°]	14.0	14.7	6.2	24.3	21.4	28.0	25.9	17.4
	Angle of attack amp., α_{amp} [°]	2.2	7.9	8.4	3.3	10.3	4.0	12.6	22.4
0.63	Reduced frequency, k	0.080	0.080	0.082	0.076	0.077	0.073	0.074	0.077
	Mean angle of attack, α_{mean} [°]	13.8	11.7	5.1	21.1	18.0	24.4	21.9	12.8
	Angle of attack amp., α_{amp} [°]	1.5	4.1	4.6	2.4	6.8	2.6	8.2	12.6
0.80	Reduced frequency, k	0.054	0.055	0.055	0.053	0.053	0.052	0.052	0.053
	Mean angle of attack, α_{mean} [°]	11.3	9.6	4.1	15.4	14.2	18.8	17.7	9.0
	Angle of attack amp., α_{amp} [°]	1.0	2.6	2.6	1.1	4.7	4.0	5.7	6.3
0.95	Reduced frequency, k	0.039	0.039	0.039	0.038	0.038	0.038	0.038	0.038
	Mean angle of attack, α_{mean} [°]	8.3	7.0	3.1	12.4	10.4	14.4	12.7	6.4
	Angle of attack amp., α_{amp} [°]	0.6	1.4	1.5	1.1	2.7	1.3	3.0	3.7

Figure 5.4 shows an example of dynamic stall occurring over a single rotor cycle during the WInDS simulation of the 10 m/s, 30° yaw test case at r/R = 0.3. The angle of attack profile is similar to Figure 4.6b, showing comparable response in full 3D testing as in 2D, with significant deviations from the steady airfoil data. Without the dynamic stall model active, the coefficient of normal force follows the steady airfoil data exactly.

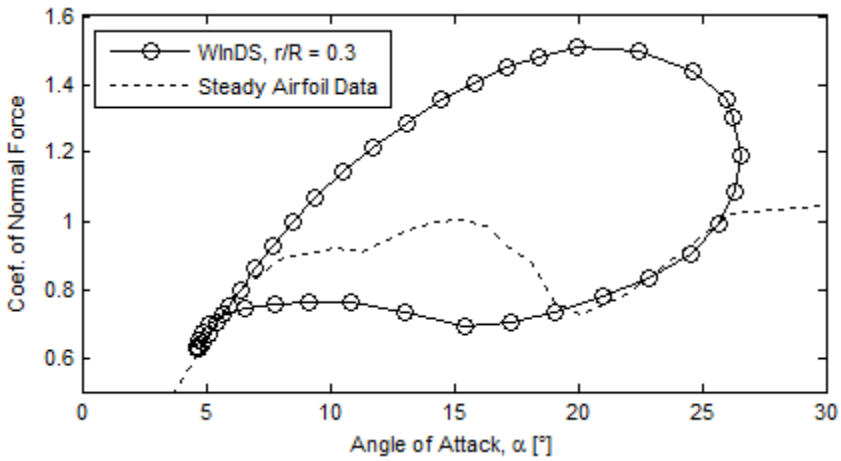

Figure 5.4: Example of dynamic stall occurring during a WInDS simulation

UAE Sequence S, U = 10 m/s, Yaw = 30°, r/R = 0.3

Once initial transients settle, WInDS simulations show cycle to cycle repeatability as the unsteady forcing conditions remain constant. The UAE data follow cycle to cycle trends, but with significant variability due to turbulent fluctuation, especially for unattached flow. To account for this, the UAE data is averaged in 1° azimuth angle bins for at least thirty cycles. Figure 5.5 shows WInDS and FAST coefficient of normal and axial force results for a single rotor cycle compared to the averaged UAE data for the 10 m/s, 30° yaw test case.

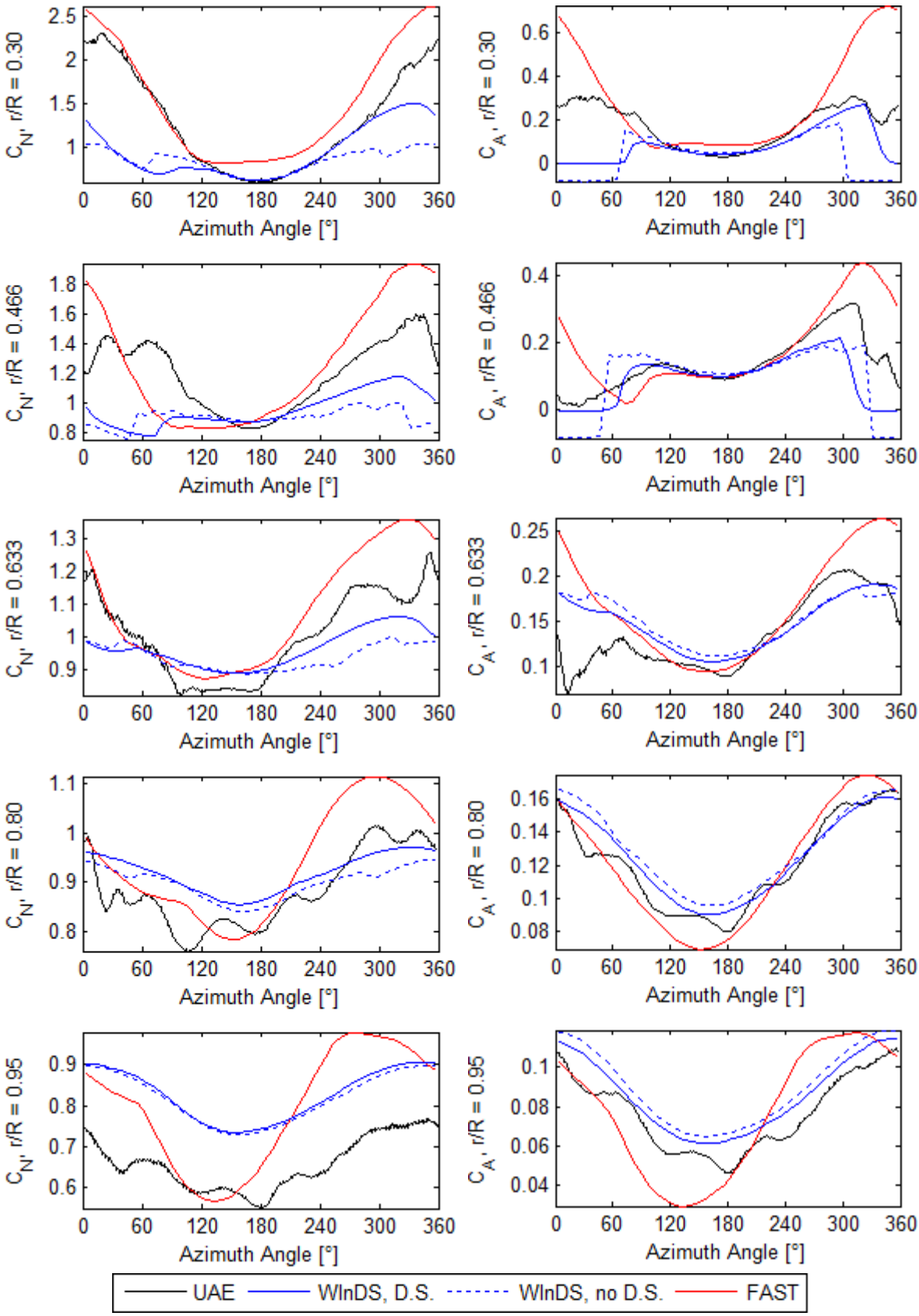

Figure 5.5: Span distributed C_N and C_A for UAE Seq. S, 10 m/s, 30° yaw

A similar trend can be seen as with the steady cases, in which coefficient of normal force is underpredicted near the blade root and overpredicted near the blade tip. Near the blade root where conditions are highly unsteady, WInDS with dynamic stall significantly improves the coefficient of normal force predictions. Minor qualitative improvements to the axial force predictions are also achieved, especially predicting the onset of flow separation near the root and with less over prediction near the blade tip.

The most concerning discrepancy between WInDS and the experimental data is the underprediction of peak normal forces due to preemptively shedding the leading edge vortex. The instrumented blade had additional roughness from the pressure taps that could have increased the severity of dynamic stall. It is likely to also be partially a result of three-dimensional stall delay, a widely acknowledged yet poorly understood phenomenon. As wind turbine or helicopter rotors rotate, flow separation tends to be delayed further than what is measured by two dimensional pitch oscillation experiments. Several empirical correction models have been proposed, summarized by Breton (2008), which typically modify the steady two-dimensional airfoil tables along the blade span. The L-B dynamic stall model is inherently a 2D model so stall delay effects are currently unaccounted for in WInDS. Stall delay is beyond the scope of this work, but is an import consideration for future development of WInDS. The work of Wang, et al (2013) looks particularly promising to this end; 3D modifications to the Kirchhoff-Helmholtz model were presented which could improve the accuracy of the L-B model.

When the yaw angle is further increased to 60°, the angle of attack changes so rapidly that rotor/wake interaction effects dominate the unsteady blade element viscous effects. As a result, the solution with and without dynamic stall converge and match the experimental data quite well as shown in Figure 5.6 for the 10 m/s, 60° yaw case. The solutions are almost identical except for improved prediction of peak forces near the root using the dynamic stall model.

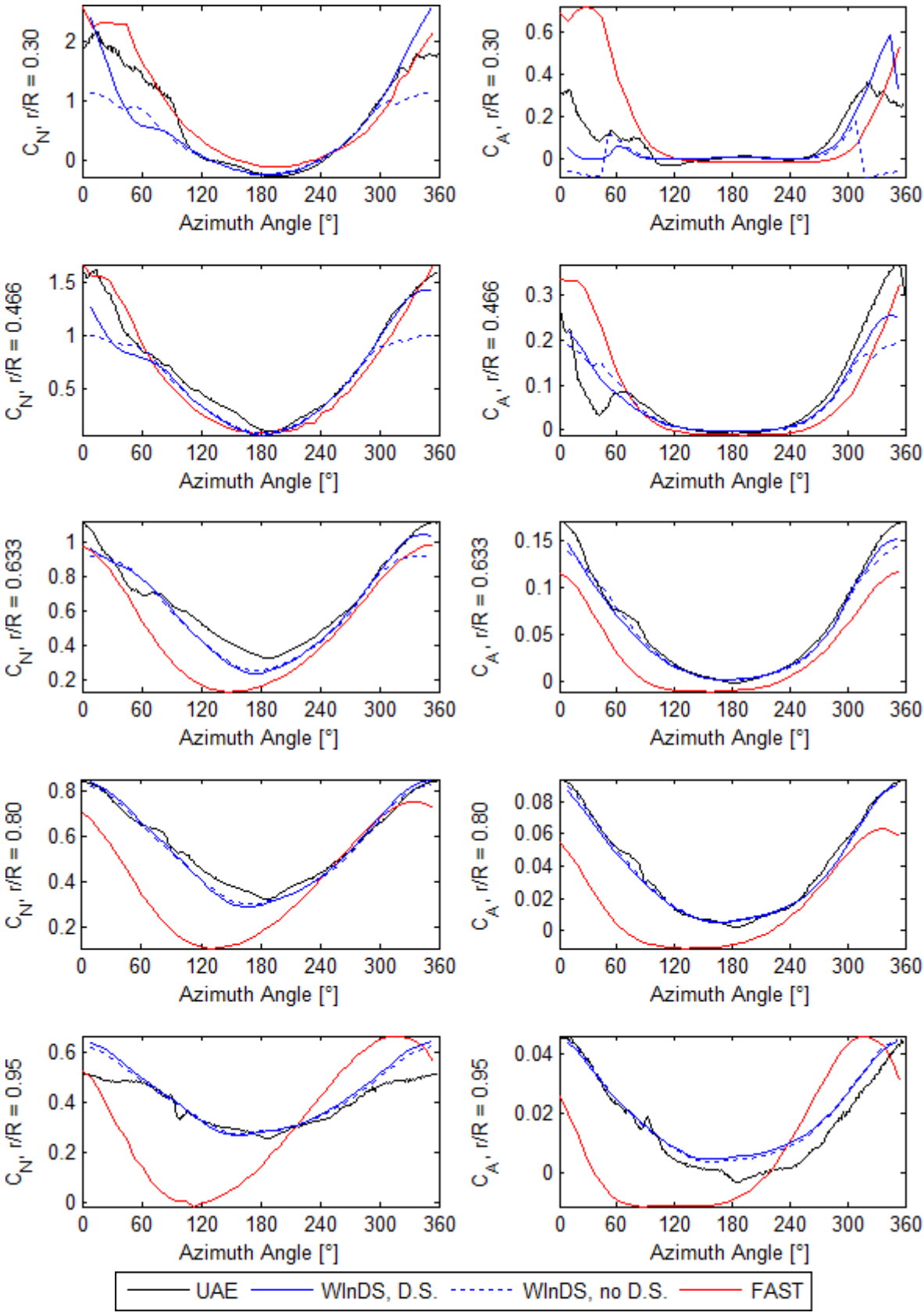

Figure 5.6: Span distributed C_N and C_A for UAE Seq. S, 10 m/s, 60° yaw

Similar to the steady data, integrating the distributed forces along the blade to determine the thrust, torque, and power tends to average out predictions errors. The thrust and torque per blade are well predicted by WInDS using the dynamic stall model in Figure 5.7 for the 10 m/s, 30° yaw case. WInDS and FAST predictions for power poorly fit the trend in the experimental data, but the average values are still quite close. This discrepancy is caused by the strain gauge on the low speed shaft that was used to collect power data. Cyclical loading from the unbalanced rotor and gravity cause shaft bending, resulting in cyclical measurement error that does not reflect the aerodynamic torque. Table 5.3 summarizes the thrust, torque, and power results for all yawed test cases. The root mean square (RMS) error is used to quantify the model fitness to the experimental data. Using the dynamic stall model improves the accuracy of WInDS in all cases. Mean values in Table 5.4 are also significantly improved. Appendix C provides additional supplemental figures for yawed test cases.

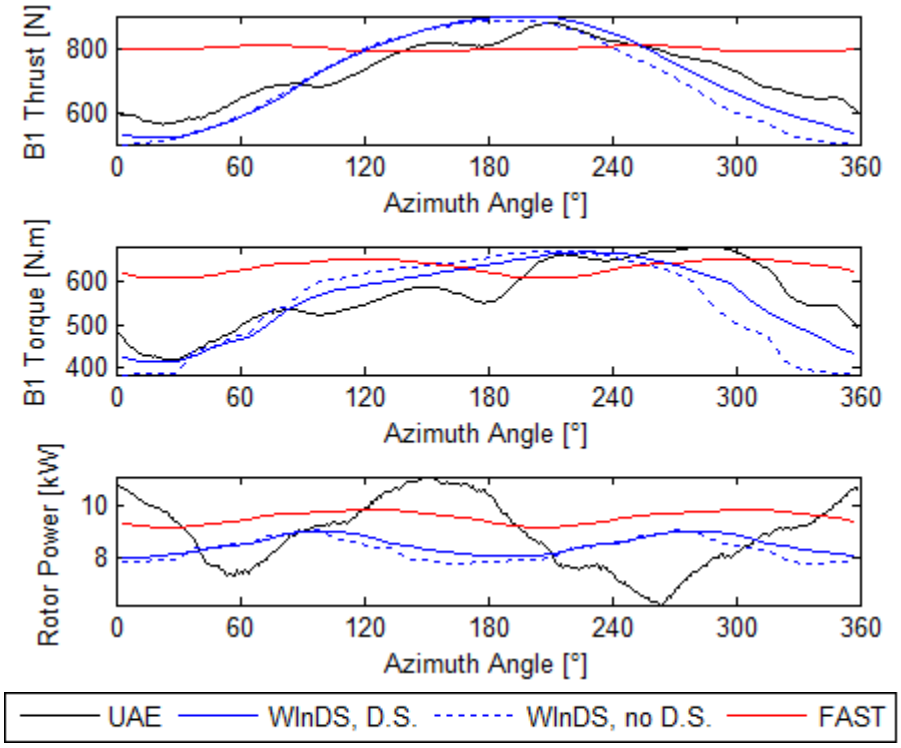

Figure 5.7: Thrust and torque per blade and total aerodynamic rotor power for UAE Sequence S, 10 m/s, 60° yaw

Table 5.3: RMS error between model predictions and UAE data for unsteady cases

	Wind Speed [m/s]	10			13		15		
	Yaw Angle [°]	10	30	60	10	30	10	30	60
Blade 1 Thrust	WInDS (N)	81.1	75.4	40.4	180.9	150.8	229.7	211.7	97.6
	WInDS, D.S. (N)	56.2	54.5	38.5	152.9	110.3	201.5	152.6	74.4
	Improvement w. D.S. (%)	30.7	27.8	4.7	15.5	26.9	12.3	27.9	23.8
Blade 1 Torque	WInDS (N·m)	67.6	84.9	26.8	194.4	169.7	283.4	246.3	119.0
	WInDS, D.S. (N·m)	41.0	49.8	17.9	56.5	94.7	91.2	117.8	84.5
	Improvement w. D.S. (%)	39.3	41.3	33.2	70.9	44.2	67.8	52.2	29.0
Rotor Power	WInDS (kW)	1.6	1.7	0.8	2.8	2.8	5.2	4.9	2.9
	WInDS, D.S. (kW)	1.3	1.6	0.7	0.9	2.1	2.1	3.4	2.6
	Improvement w. D.S. (%)	15.9	9.6	6.7	69.6	24.4	59.3	30.4	9.2

Table 5.4: Average percent error between model predictions and UAE data for unsteady cases

	Wind Speed [m/s]	10			13		15		
	Yaw Angle [°]	10	30	60	10	30	10	30	60
Blade 1 Thrust	WInDS (N)	-9.3	-3.6	-8.3	-17.5	-12.8	-20.5	-16.6	0.7
	WInDS, D.S. (N)	-6.5	-0.6	-6.7	-14.7	-8.4	-17.8	-10.8	5.4
	Improvement w. D.S. (%)	2.9	3.0	1.6	2.8	4.4	2.8	5.8	-4.6
Blade 1 Torque	WInDS (N·m)	-8.0	-1.9	-9.3	-26.7	-13.5	-47.7	-24.0	-3.7
	WInDS, D.S. (N·m)	-4.4	0.0	-6.9	-6.4	-4.0	-10.4	-3.3	0.3
	Improvement w. D.S. (%)	3.6	1.9	2.5	20.3	9.4	37.2	20.7	3.3
Rotor Power	WInDS (kW)	-11.7	-7.7	-5.5	-27.1	-18.7	-52.7	-32.9	-6.2
	WInDS, D.S. (kW)	-8.8	-5.9	-2.9	-6.8	-10.0	-19.4	-15.0	-2.3
	Improvement w. D.S. (%)	3.0	1.8	2.6	20.3	8.7	33.3	17.9	4.0

5.3 Occurrence of Dynamic Stall in FOWTs

To model FOWTs aerodynamics in WInDS, the results from FAST simulations are used to predefine structural motions. This decouples the structural kinematic and aerodynamic response in WInDS, but still gives a very reasonable approximation of the structural motions and controller response for a given set of conditions. The NREL 5MW Offshore Reference Turbine (Jonkman, et. al, 2009) is modelled on the OC3/Hywind spar-buoy (Jonkman, 2010) and the MIT/NREL TLP (Matha, 2009) floating platforms, as well as onshore as a baseline. For consistency, a similar test matrix is used as Sebastian (2012), which examined three wave and wind conditions for below rated, rated, and above rated operation, outlined in Table 5.5.

Table 5.5: Test matrix for FAST and WInDS simulations of FOWTs

	Wind Speed, U_∞ [m/s]	Rotor Speed, Ω [rpm]	Tip Speed Ratio, λ [-]	Significant Wave Height, H_s [m]	Peak Spectral Period, T_p [s]
Below-rated	6.00	8.76	9.63	1.83	12.72
Rated	11.40	12.10	7.00	2.54	13.35
Above-rated	18.00	12.10	4.43	4.09	15.33

Aerodynamic modeling in FAST is conducted with the dynamic inflow, wake induction-factor, dynamic stall and hub and tip loss models active in order to match realistic conditions as closely as possible. The free-stream wind velocity is defined as steady and uniform with no yaw or shear. Wave time series are calculated with the JONSWAP spectrum using the sea state conditions in Table 5.5. All structural and platform degrees of freedom are used to simulate typical operating conditions with the torque and pitch controllers on.

The steady state properties for the NREL 5 MW were determined by Jonkman et. al (2009) using FAST. Therefore the FAST results for onshore test cases are assumed to be the correct physical solution and used as the baseline. The NREL 5MW uses the DU series of airfoils developed at the Delft University of Technology as well as the NACA64-618 near the blade tip. The steady 2D airfoil data used by the FAST model is corrected for 3D stall effects using methods described by Du & Selig (1998) and Eggers (2003).

This empirical correction used in FAST presents modeling challenges when using WInDS with the dynamic stall model, because the Kirchhoff/Helmholtz trailing edge separation point fits do not account for stall delay modifications to the 2D steady airfoil data. Since the separation point is calculated using the data for coefficient of normal force, the normal force fits are still quite good as shown in Figure 5.8. However, the fits to the coefficient of axial force are poor at low angles of attack, where the turbine operates for the majority of the simulations. Using non-stall delayed data improves the fit considerably, although the DU series of airfoils is still not well characterized by the Kirchhoff/Helmholtz Theory.

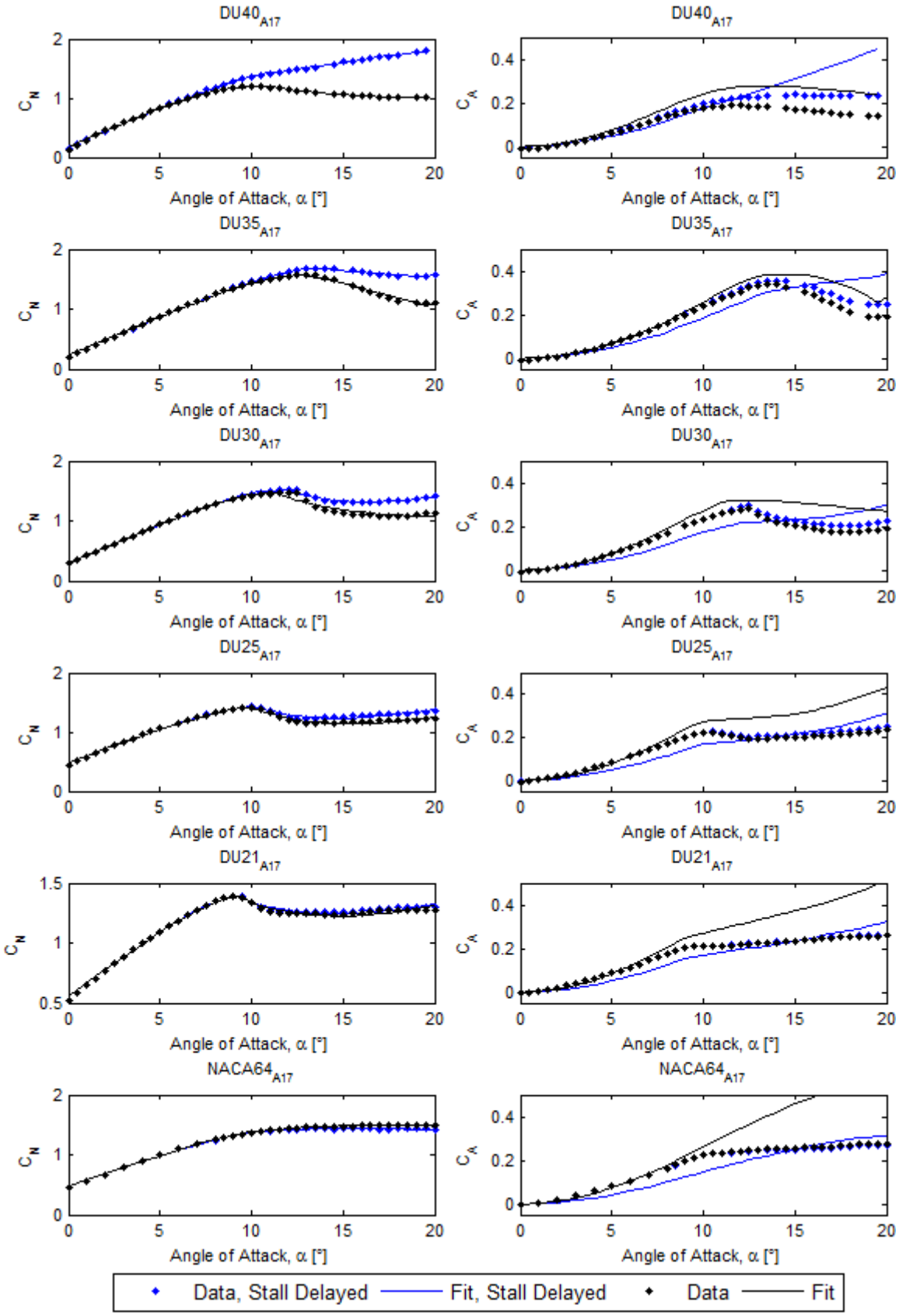

Figure 5.8: Kirchhoff/Helmholtz trailing edge fits for the NREL 5MW airfoils

Table 5.6 summarizes rotor thrust and torque for the NREL 5MW using WInDS with and without stall delayed steady airfoil data. Using the non-stall delayed data improves the torque predictions for the dynamic stall model considerably in below rated and rated conditions. However, due to poor the Kirchhoff/Helmholtz trailing edge fits for C_a, WInDS without the dynamic stall model provides better predictions for torque over the range of wind speeds. This is contrary to the results for the UAE experimental data presented in the previous section, which has superior model performance using the dynamic stall model. Kirchhoff/Helmholtz fits for the S809 airfoil data are more accurate at low angles of attack. Additionally the S809 is a very gradually stalling airfoil, causing the separation point fits to be accurate up to 18° whereas the DU series is only accurate up to about 10° for C_n and 5° for C_a.

Table 5.6: Model predictions for the NREL 5MW onshore

			Below Rated		Rated		Above Rated	
			T (N)	Q (N·m)	T (N)	Q (N·m)	T (N)	Q (N·m)
Baseline	FAST	Mean ($\times 10^6$)	0.241	1.013	0.642	4.180	0.352	4.180
Stall Delay	WInDS	Mean ($\times 10^6$)	0.250	1.083	0.654	4.257	0.333	4.092
		% Error	3.64	6.90	1.90	1.85	-5.59	-2.10
	WInDS, D.S.	Mean ($\times 10^6$)	0.245	0.701	0.639	3.134	0.336	4.303
		% Error	1.65	-30.78	-0.41	-25.03	-4.69	2.94
No Stall Delay	WInDS	Mean ($\times 10^6$)	0.250	1.085	0.649	4.227	0.324	4.002
		% Error	3.68	7.09	1.10	1.12	-8.01	-4.27
	WInDS, D.S.	Mean ($\times 10^6$)	0.245	0.883	0.632	3.714	0.326	4.396
		% Error	1.32	-12.85	-1.48	-11.15	-7.50	5.16

Thrust predictions in Table 5.6 are improved by the inclusion the dynamic stall model by about 2%. Normal force increases where dynamic stall occurs near the blade root, but also decreases outboard due to the trailing edge flow separation model resulting in a lower net thrust. While WInDS underpredicts C_a with the dynamic stall model on, it has a minor effect on the C_L predictions due to high tip speed ratios and low angles of attack. Figure 5.9 shows the percent contribution to C_L from C_a for WInDS. Changes in the percent contribution to C_L when using the

dynamic stall model are very small along the blade span. The exception is the blade node closest to the root where dynamic stall increases the average normal force and thus decrease the ratio more dramatically. Given that the Kutta-Joukowski theorem uses the coefficient of lift to calculate vortex filament circulation strengths, the wake evolution is not adversely affected by poor axial force predictions using the dynamic stall model.

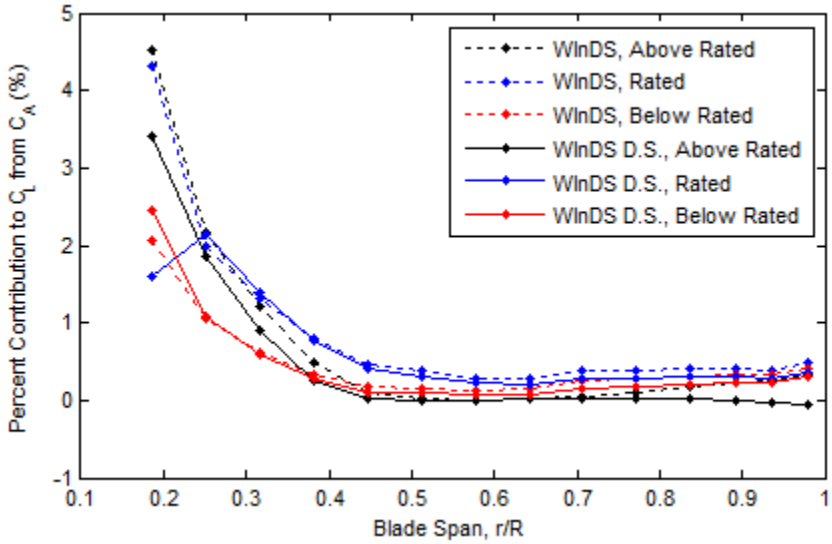

Figure 5.9: Average percent contribution to lift from axial force for WInDS

An example of the wake structure generated by WInDS is shown in Figure 5.10. The OC3/ Hywind spar buoy is simulated in above rated conditions for 120 seconds using the stall delayed airfoil data. Only the wake generated by one of the three blades is shown for clarity. Instances of dynamic stall leading edge vortex separation are observable near the blade root, highlighted and tracked in the wake in blue. Differences in the wake evolution are subtle because only the nodes closest to the blade root are significantly changed due to leading edge flow separation. As the wake propagates however, the effect becomes more apparent. Both cases become unstable but the case with the dynamic stall remains more organized, most clearly seen between 13*D* and 15*D* in Figure 5.10. This can likely be attributed to smoother variations in the coefficient of lift with the dynamic stall model on.

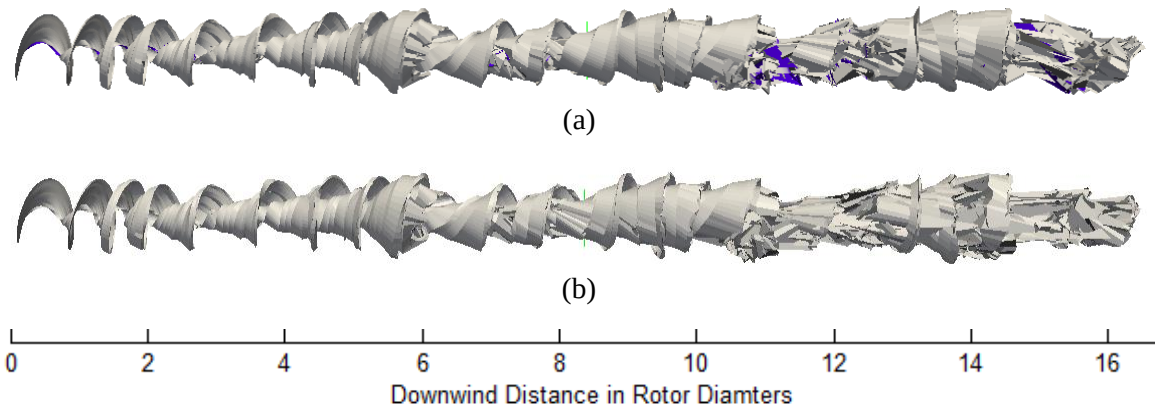

Figure 5.10: WInDS simulation wake structure after 120 seconds with the dynamic stall model (a) and without (b)

Table 5.7 summarizes the percentage of time the flow is separated at different blade nodes. There are no instances of leading edge flow separation for blade nodes beyond *r/R* = 0.252 so further outboard nodes are combined in the table. Using the non-stall delayed airfoil data, the blade node at *r/R* = 0.187 experience separated flow for the duration of the simulations in rated and above rated conditions, across all three models. There are isolated instances of platform motion decreasing the angle of attack enough to allow brief flow reattachment for the OC3/Hywind spar buoy.

Table 5.7: Percent of time flow is separated predicted by WInDS using dynamic stall

	r/R	Onshore			OC3/Hywind Spar-buoy			MIT/NREL TLP		
		Below Rated	Rated	Above Rated	Below Rated	Rated	Above Rated	Below Rated	Rated	Above Rated
Stall Delay	0.187	0.0	59.5	70.5	1.0	53.3	78.9	0.0	68.5	74.0
	0.252	0.0	0.0	0.0	0.0	0.0	1.8	0.0	0.0	0.0
	Outboard	0.0	0.0	0.0	0.0	0.0	0.0	0.0	0.0	0.0
No Stall Delay	0.187	33.3	100.0	100.0	49.7	99.7	97.8	33.3	100.0	100.0
	0.252	0.0	0.0	0.0	0.0	0.0	1.6	0.0	0.0	0.0
	Outboard	0.0	0.0	0.0	0.0	0.0	0.0	0.0	0.0	0.0

Using the stall delayed steady airfoil data, higher steady C_n values result in a higher critical normal force criteria, C_{n1}, allowing the flow to cyclically reattach. It seems counter

intuitive that flow is separated more often for the onshore turbine than the OC3/Hywind spar buoy in Table 5.7 at rated conditions. This can be explained by examining when flows separation is occurring for the onshore turbine. At rated and above rated conditions, dynamic stall and reattachment occur with every rotor rotation due to cyclical changes in angle of attack as a result of the turbine shaft tilt. The above rated case is stalled a high proportion of the time due to further delay in flow reattachment as a result of higher amplitude angle of attack variations near the root. The floating cases are less periodic than the onshore. The random waves cause platform motion that result in cycle to cycle variability in the angle of attack. As a result, flow separation is avoided for some cycles by platform motion decreasing the angle of attack or rate of change. Alternatively, flow reattachment can be prevented for multiple cycles resulting in the higher proportions of separated flow.

Figure 5.11 shows the time series for angle of attack and coefficient of lift for the MIT/NREL TLP under rated conditions at the blade node r/R = 0.187. Flow is separated at this blade node for the duration of the simulation. With the dynamic stall model, the angle of attack time series experiences a phase lag compared to the base version of WInDS. This lag is reflected in the coefficient of lift, which also experiences higher peak lift and typical dynamic stall hysteresis. Figure 5.12 shows a further outboard node, r/R = 0.252, where the flow is attached for the entire simulation. Under attached flow, the angle of attack using the dynamic stall model slightly leads the base version of WInDS. Qualitatively the C_l predictions of the two models follow the same trend, although C_l is consistently slightly lower for attached flow using the dynamic stall model. These differences are due to a combination of lower C_n predictions and the propagation of error from under0predicted C_a. The same trends hold for the OC3/Hywind Spar-buoy, however due to more significant platform motion, angle of attack changes are less periodic. Table 5.8 summarizes the variation in C_L across all cases using the non-stall delayed steady airfoil data.

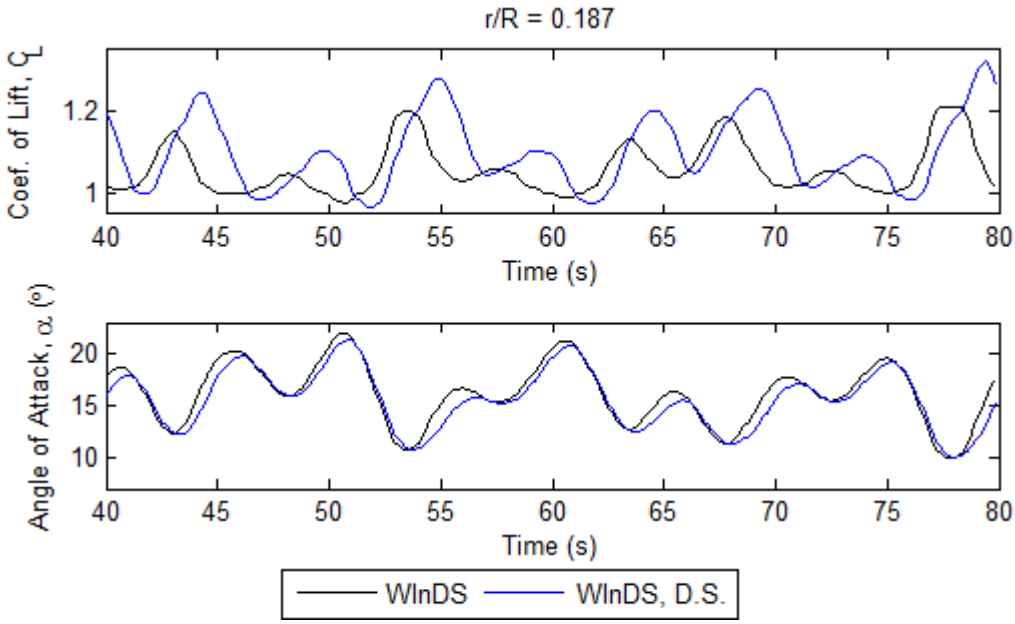

Figure 5.11: Time series of C_L and α for the NREL 5MW on the MIT/NREL TLP in rated conditions blade node r/R = 0.187, detached flow

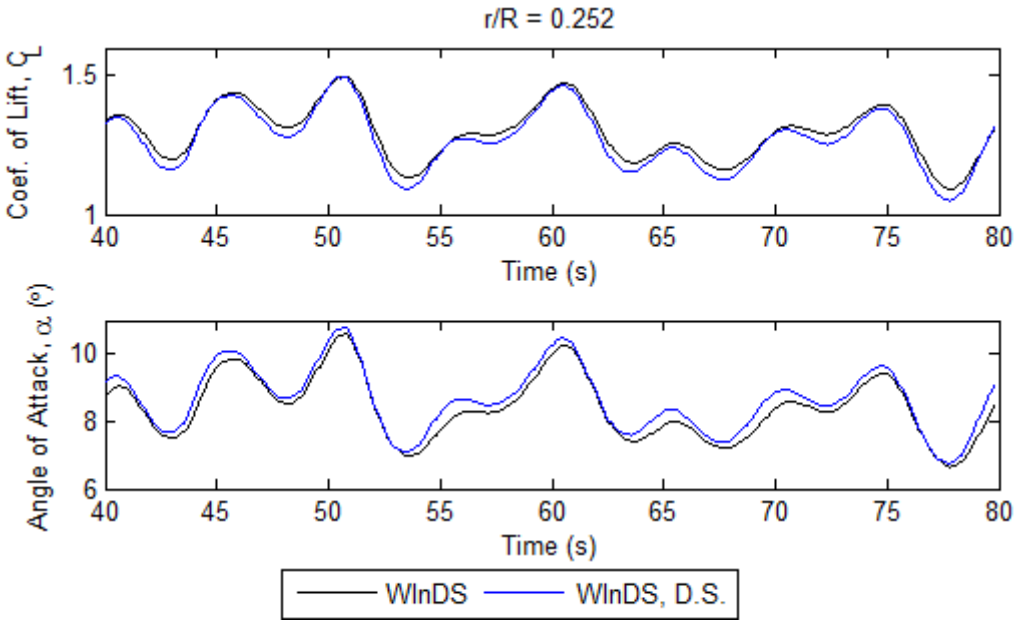

Figure 5.12: Time series of C_L and α for the NREL 5MW on the MIT/NREL TLP in rated conditions, blade node r/R = 0.252, attached flow

Table 5.8: Summary of CL at blade node r/R = 0.187

		WInDS, no D.S.				WInDS, D.S.			
		Mean	St. Dev.	Min	Max	Mean	St. Dev.	Min	Max
Monopile	Below Rated	1.165	0.037	1.102	1.210	1.149	0.046	1.077	1.233
	Rated	1.051	0.038	1.008	1.113	1.094	0.068	0.995	1.190
	Above Rated	1.038	0.046	0.983	1.125	1.086	0.080	0.978	1.211
NREL/ MIT TLP	Below Rated	1.157	0.046	1.062	1.210	1.149	0.062	1.039	1.264
	Rated	1.060	0.061	0.979	1.210	1.102	0.088	0.968	1.322
	Above Rated	1.041	0.058	0.962	1.202	1.089	0.088	0.973	1.292
OC3/ HyWind Spar	Below Rated	1.152	0.047	1.052	1.210	1.157	0.064	1.040	1.298
	Rated	1.071	0.051	0.963	1.186	1.113	0.069	0.976	1.309
	Above Rated	1.026	0.063	0.917	1.210	1.069	0.082	0.961	1.331

Figure 5.13 shows blade node *r/R* = 0.187 for the TLP at below rated conditions. There are instances of both flow separation and reattachment and the trends from the previous two figures hold respectively. Separated flow is indicated by the plot area highlighted in gray.

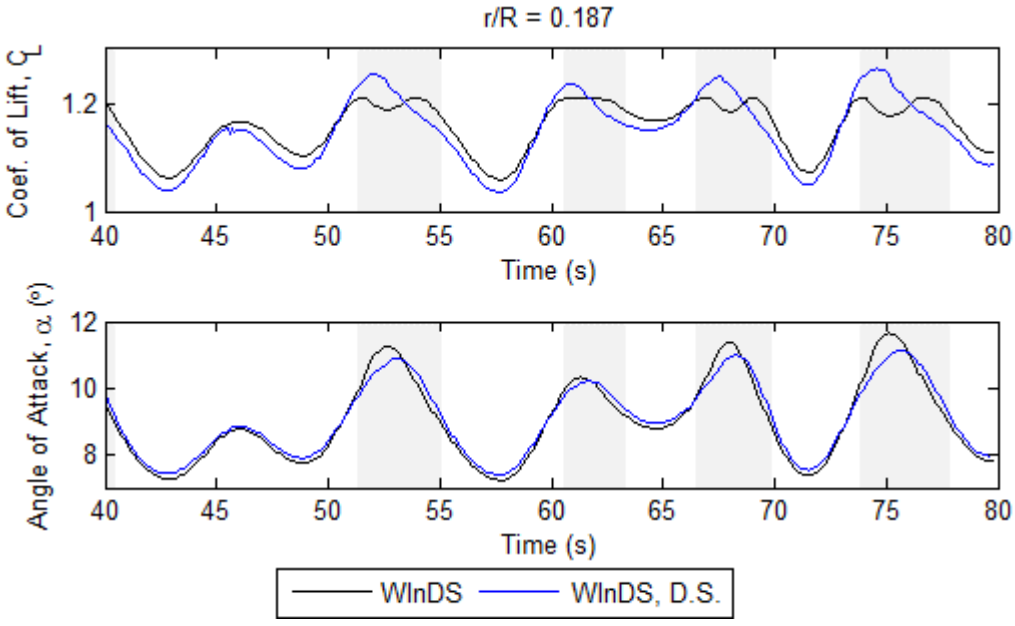

Figure 5.13: Time series of C_L and α for the NREL 5MW on the MIT/NREL TLP in below rated conditions blade node r/R = 0.187, detached flow highlighted in gray

CHAPTER 6
CONCLUSIONS AND FUTURE WORK

6.1 Concluding Remarks

Inclusion of a dynamic stall model to account for blade section level unsteadiness enables WInDS to predict aerodynamic loads during instances of dynamic stall when static 2D airfoil data is not representative of the true physical behavior. The validation work presented in this thesis shows excellent agreement with experimental data, increasing the confidence in the model for future research or design work.

The implemented Leishman-Beddoes dynamic stall model shows excellent agreement with two-dimensional unsteady pitch oscillation experimental data presented in Chapter 4 and Appendix A. An alternative criteria is defined for the transition to the stalled chord force model rather than the critical normal force criteria. A second critical normal force criteria is calculated as the coefficient of normal force under potential flow corresponding to the chord force break point angle of attack under steady conditions. As a result, lift and drag are accurately predicted for a variety of airfoils over a wide range of operating conditions included Reynolds number, mean angle of attack, angle of attack amplitude, and reduced frequency.

The dynamic stall model is integrated into WInDS as an optional alternative to two-dimensional steady airfoil look-up tables. This addition allows WInDS to model unsteady viscous and pressure effects at the blade level as well as unsteady rotor scale effects brought on by the wake. Comparisons to wind tunnel data for a full scale turbine in Section 5.2 show considerable improvement from the baseline WInDS model without dynamic stall. The improvement in aerodynamic rotor power predictions for steady cases range from 1.5% to 64%, with the largest improvements at high wind speed. Yawed cases are similarly improved, with

aerodynamic rotor power RMS error reduced by 6.7% to 69.7% and mean percent error reduced by 1.3% to 33.3%.

However, it is important to note that the model is extremely sensitive to the accuracy of Kirchhoff/Helmholtz fits to the 2D steady airfoil data. The curve fitting process is automated, but due to the high variability of aerodynamic properties for different airfoils, the routine may not always yield acceptable results. Poor fits to the data cause erroneous results, so caution should be used when applying the model to new airfoils. In these cases, fitting may need to be calculated by hand or the curve fitting routines modified for the data, which will require a significant amount of expertise on the part of the modeler. Furthermore, the dynamic stall model does not account for stall delay, so airfoil tables modified for stall delay will likely not result in suitable fits.

Sensitivity to 2D steady airfoil curve fitting is reflected in the floating simulations of the NREL 5MW. The DU airfoils used on the NREL 5MW blade are poorly characterized by the Kirchhoff/Helmholtz Theory resulting in worse prediction of rotor torque than the base version of WInDS. Thrust predictions are still improved for the NREL 5MW using the dynamic stall model however, with mean error decreasing by about 2% compared to FAST. When dynamic stall occurs, changes in the angle of attack and lift are significantly lagged compared to using steady airfoil data. Typical dynamic stall hysteresis occurs with increased peak lift. During attached flow along the majority of the blade outboard from the root, lift predictions are qualitatively similar to the base version of WInDS. Lift predictions are sufficiently accurate for analysis of wake evolution and appear to increase wake stability due to smoother load variations. Due to improved characterization of the normal force profile during the occurrence of dynamic stall, it is recommended that the dynamic stall model be used with WInDS for future analysis of FOWT wake evolution.

6.2 Future Work

6.2.1 WInDS root finding method

The combination of two dynamic models extends the fixed point iteration method to its limits. Smaller relaxation factors and higher limits on the maximum number of iterations are required, resulting in slower convergence and significantly longer simulations. This problem is exacerbated for highly unsteady cases with large yaw angles or FOWT platform motion. The use of more robust root-finding methods should be explored to avoid this problem.

6.2.2 Unsteady 3D stall effects

The Leishman-Beddoes dynamic stall model examines the unsteady response over a two-dimensional cross-section. This neglects unsteady three-dimensional effects. Several models have been developed to model stall delay, the delay in leading edge vortex shedding for rotating wings. The addition of a stall delay model will likely be a relatively simple to implement since several of the models function through modification of the steady airfoil data along the blade span. This will require reexamination of the Kirchhoff/Helmholtz trailing edge separation fits to steady airfoil data. Another phenomenon worth investigation is the span-wise propagation of dynamic stall, a phenomenon that is not well understood and not included in the Leishman-Beddoes dynamic stall model.

6.2.3 Airfoil Sensitivity

It is clear that use of the dynamic stall model in WInDS can significantly increase the global accuracy of the model. However, this is dependent on accurate characterization of the 2D steady airfoil data with Kirchhoff/Helmholtz theory curve fitting. Alternative trailing edge flow separation models or modifications to the Kirchhoff/Helmholtz theory should be explored to increase model robustness.

6.2.4 WInDS/FAST coupling

When modeling FOWTs with WInDS, platform motions must be prescribed prior to time-marching simulations. This decouples the aerodynamic and structural responses. Coupling WInDS with an existing aero-elastic computer aided engineering tool such as FAST could significantly increase the utility of WInDS predictions and give new insights into the dynamics of FOWTs. The recent release of FAST v8 significantly increased the modularity of FAST, requiring each sub-module to follow a unified framework. This should facilitate the coupling between WInDS and FAST, replacing the existing blade element momentum based aerodynamic model, AeroDyn.

APPENDIX A

SUPPLEMENTAL DYNAMIC STALL MODEL 2D VALIDATION

Section 4.4 shows sample model results for the S809 airfoil, modeled with Re = 1.0×10^6, k = [0.026, 0.04, 0.078], $\alpha_{amplitude}$ = 10°, and α_{mean} = [8, 14, 20]°. Further test cases using the OSU pitch oscillation tests are presented here. The S809 is thoroughly validated to check the accuracy of the model over a wide range of conditions. Sample results are also included for other airfoils to validate that model accuracy is not limited exclusively to the S809.

- Figures A.1 to A.9 demonstrate model performance over a range of Reynolds numbers. An extension of the results from Section 4.4, the S809 is shown at Re = [0.75, 1.25, 1.4]$\times10^6$, $\alpha_{amplitude}$ = 10°, and α_{mean} = [8, 14, 20]° at three oscillation frequencies.
- Figures A.10 to A.12 show model performance for smaller amplitude pitch oscillations. The S809 is presented where Re = 1.0×10^6, k = [0.026, 0.049, 0.077], $\alpha_{amplitude}$ = 5.5°, and α_{mean} = [8, 14, 20]°.
- Figures A.13 to A.20 provide a sample case for airfoils other than the S809. The airfoils are from three different design families, including: S801, S810, S812, S813, S825, L303, LS(1)-0417MOD, and LS(1)-0421MOD. The same test case is presented for each airfoil where Re = 1.0×10^6, $k = 0.082 \pm 0.006$, $\alpha_{amplitude}$ = 10°, and α_{mean} = [8, 14, 20]°.
- Finally, additional diagrams of the OSU experimental setup are included. Figures A.21 and A.22 show diagrams of the OSU 3x5 wind tunnel from Ramsay, et al. (1995). Figures A.23 to A.31 show the airfoil profiles for all airfoils modelled, available at <https://wind.nrel.gov/airfoils/OSU_data/>.

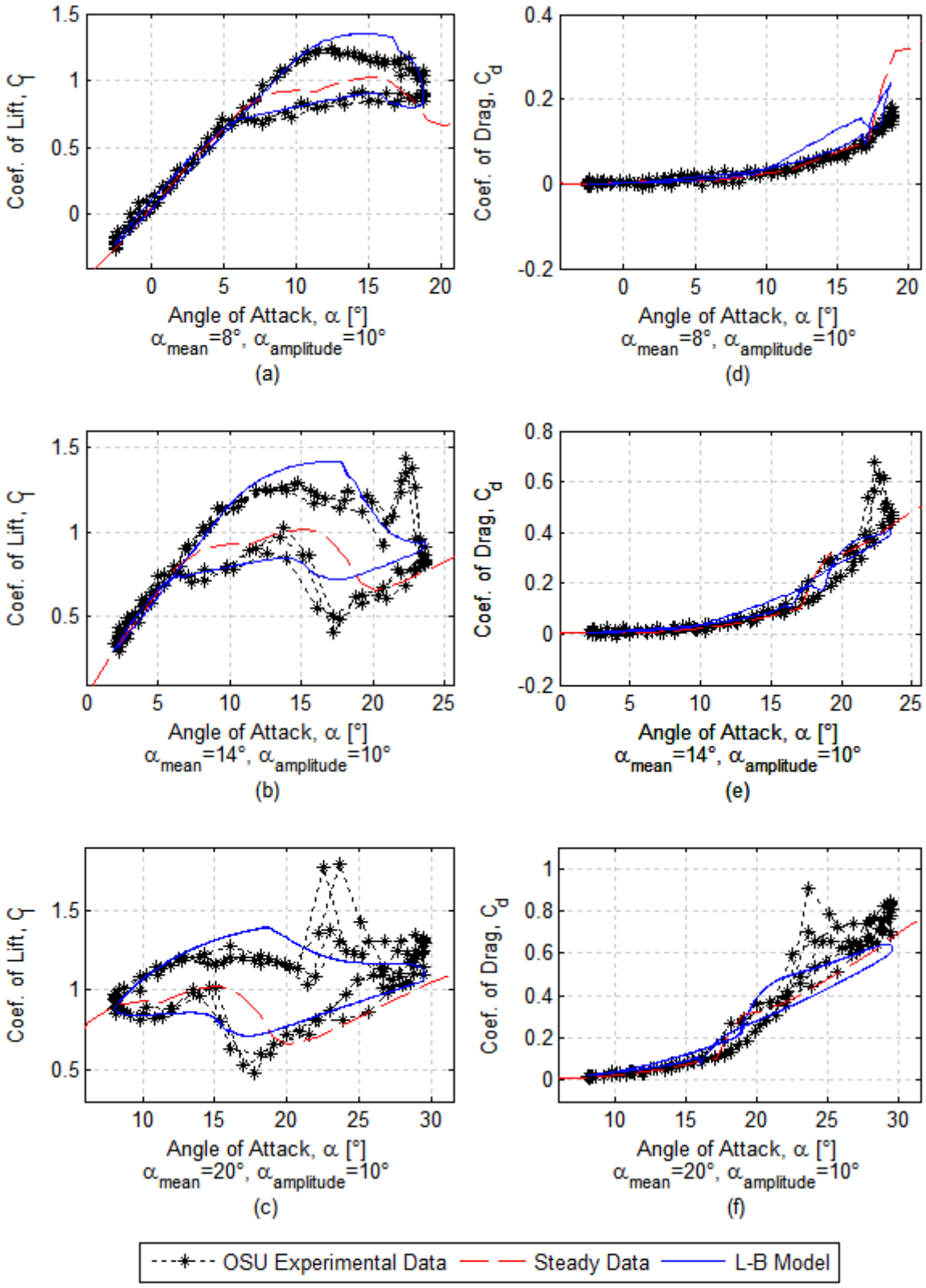

Figure A.1: C_L and C_D for the S809 Airfoil with time varying α, k = 0.033, Re = 0.75×10^6

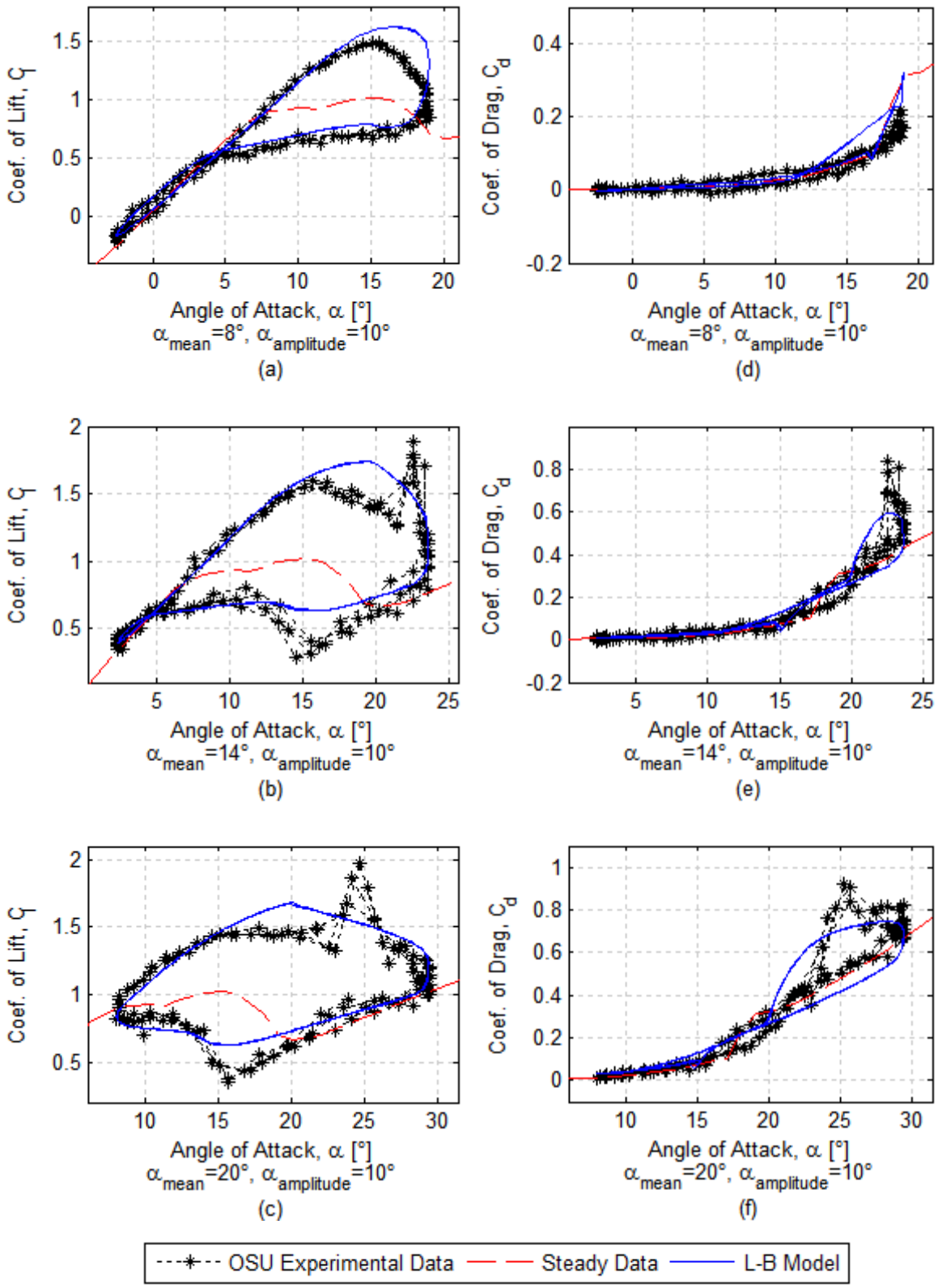

Figure A.2: C_L and C_D for the S809 Airfoil with time varying α, k = 0.069, Re = 0.75×10^6

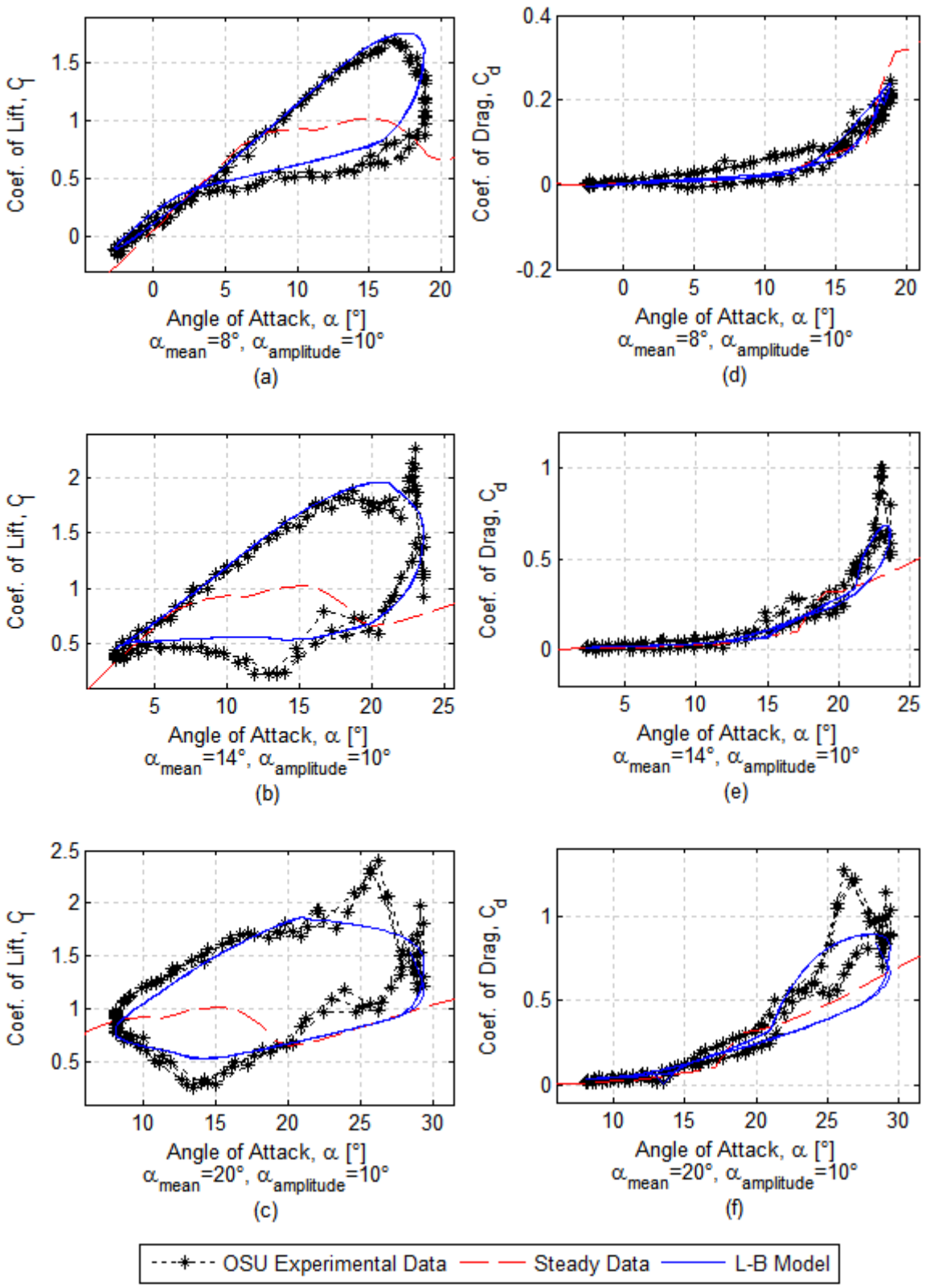

Figure A.3: C_L and C_D for the S809 Airfoil with time varying α, k = 0.100, Re = 0.75×10^6

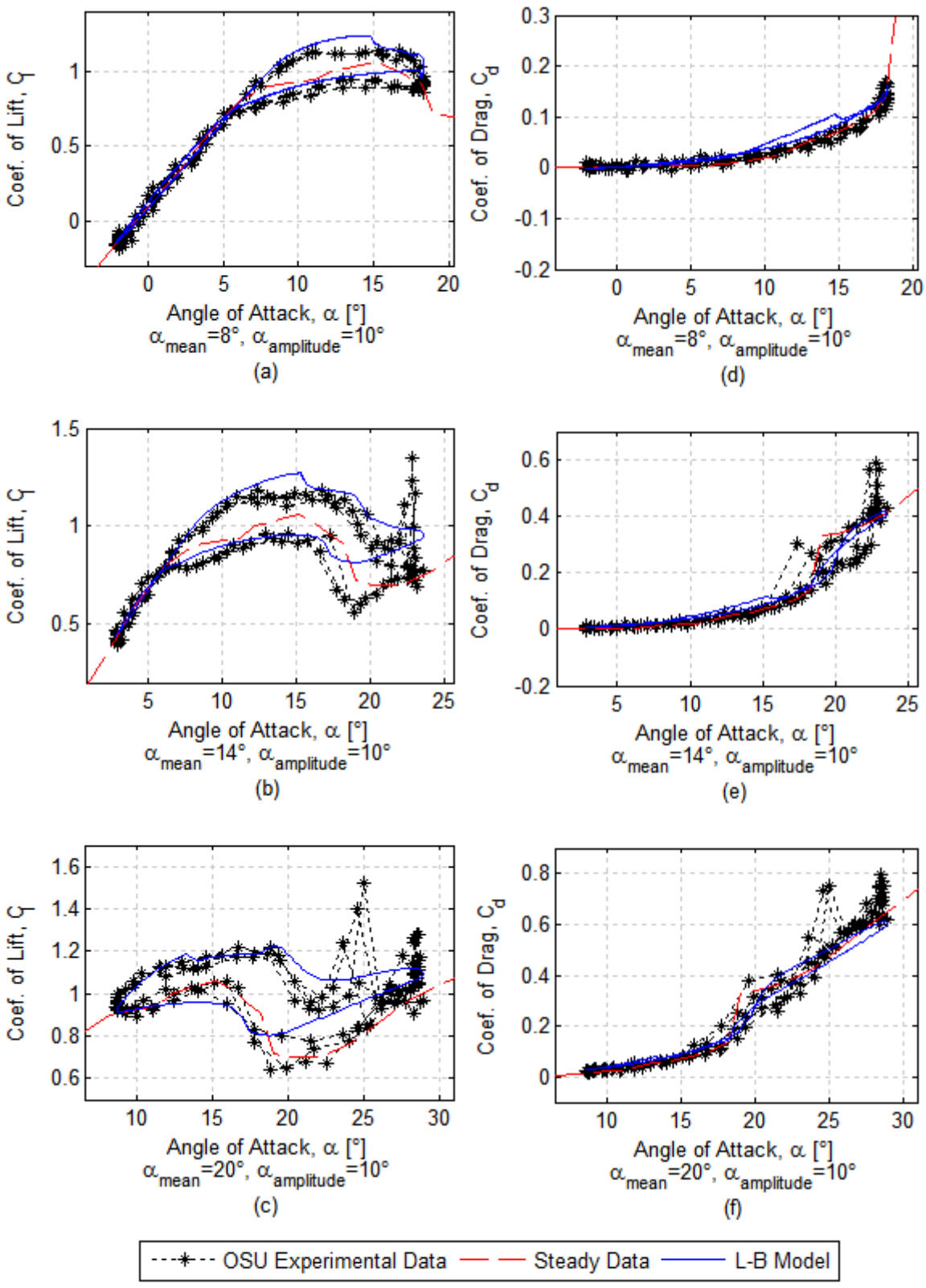

Figure A.4: C_L and C_D for the S809 Airfoil with time varying α, k = 0.020, Re = 1.25×10^6

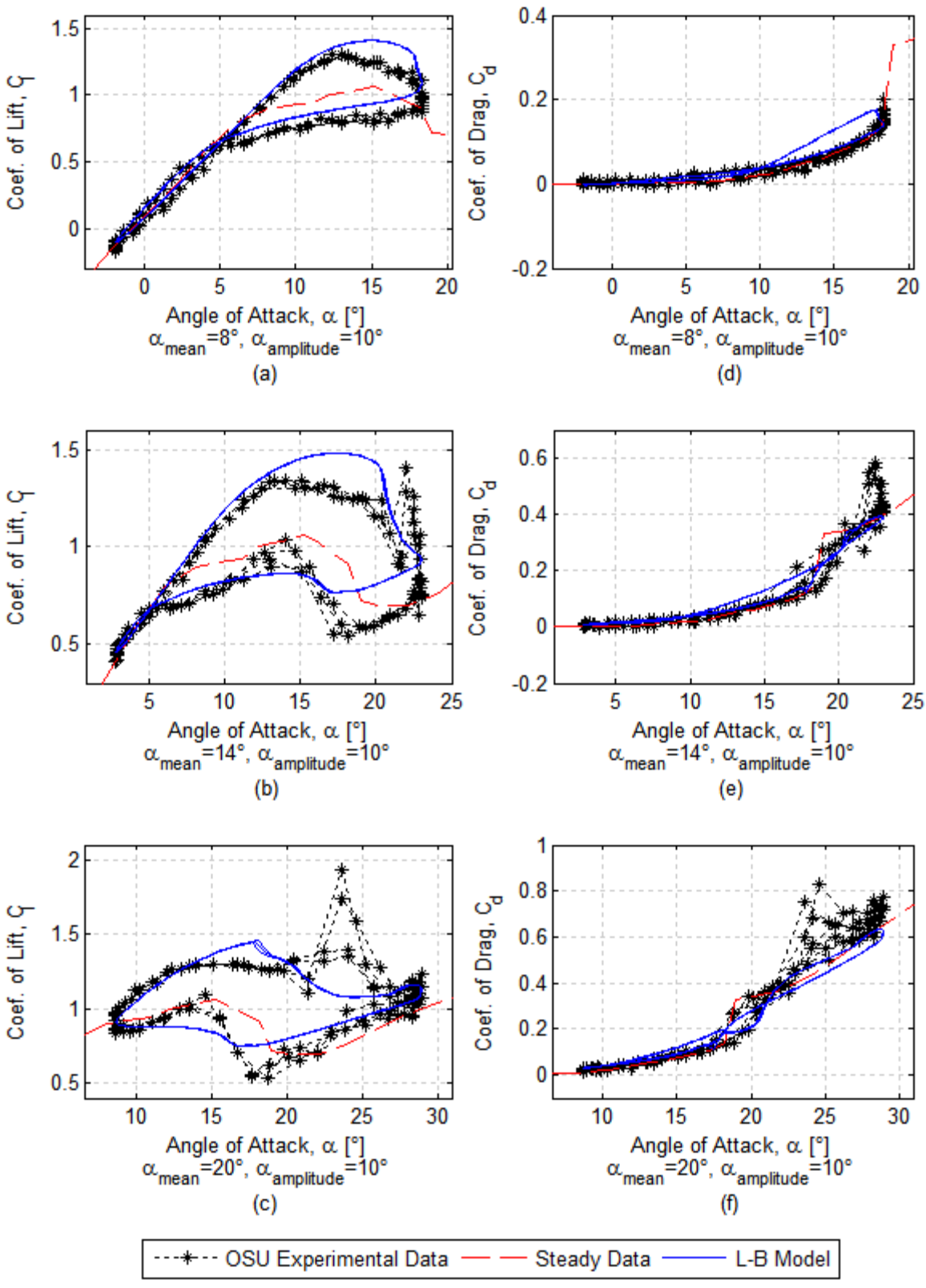

Figure A.5: C_L and C_D for the S809 Airfoil with time varying α, k = 0.040, Re = 1.25×10^6

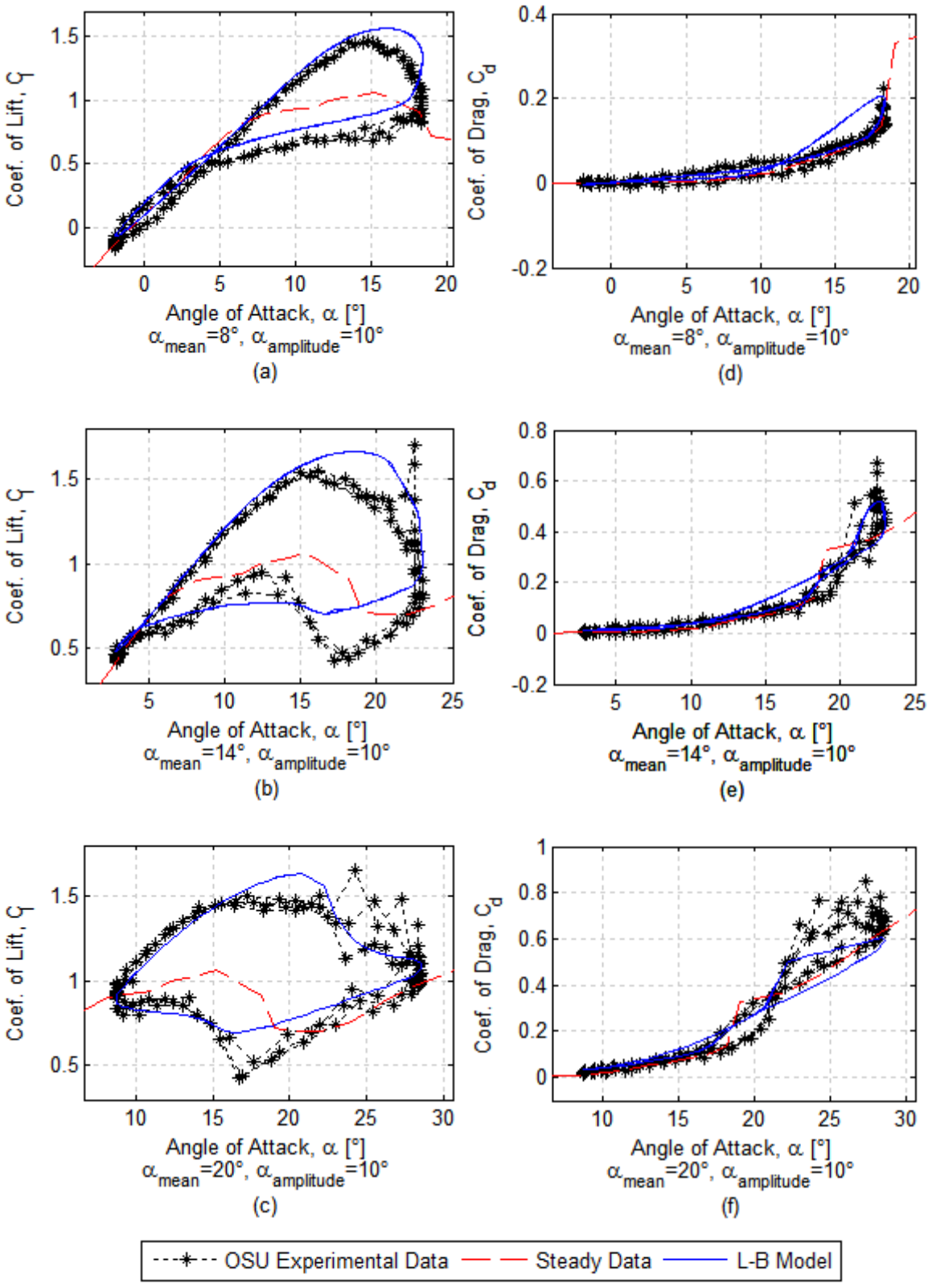

Figure A.6: C_L and C_D for the S809 Airfoil with time varying α, k = 0.062, Re = 1.25×10^6

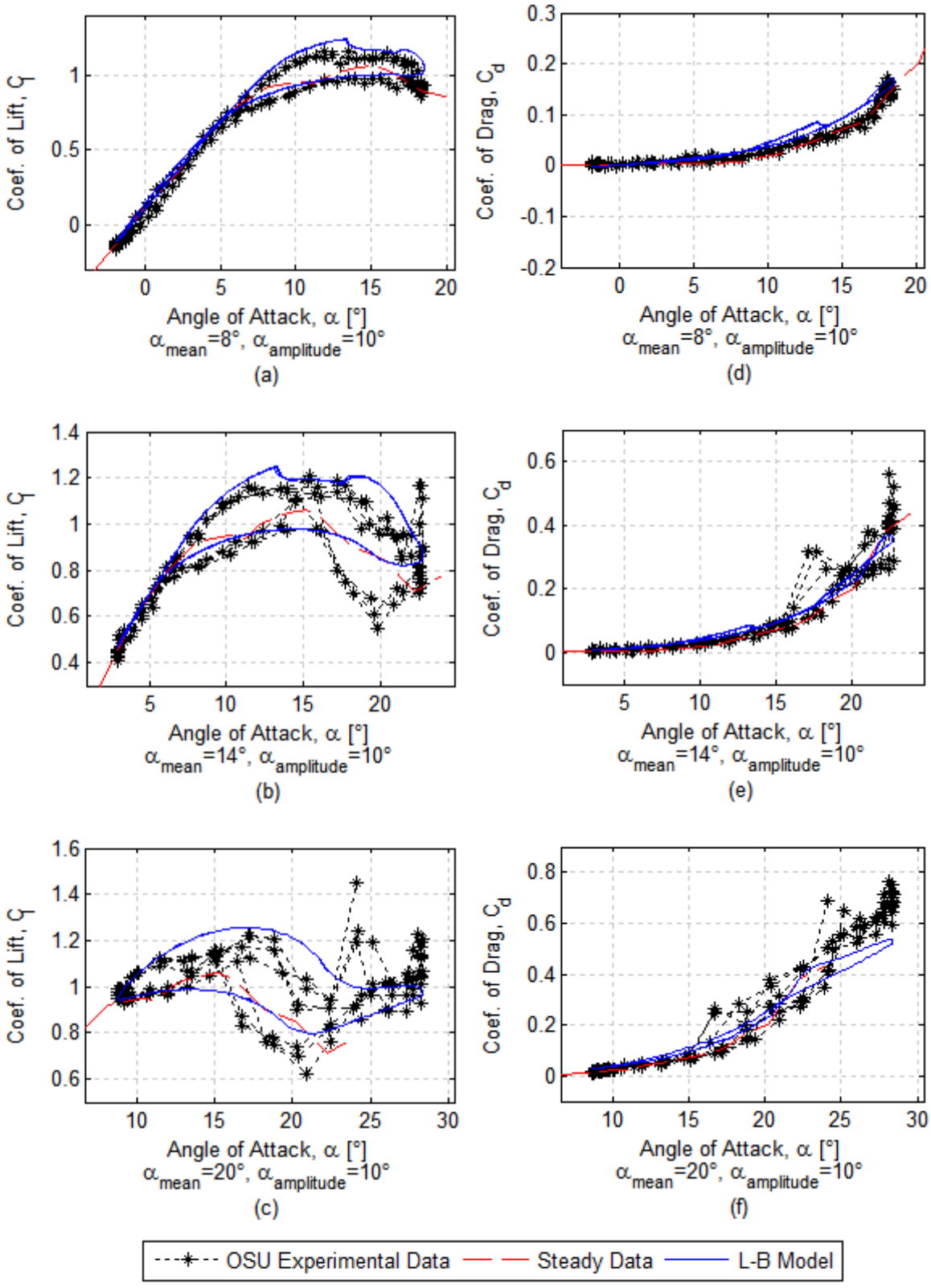

Figure A.7: C_L and C_D for the S809 Airfoil with time varying α, k = 0.018, Re = 1.40×10^6

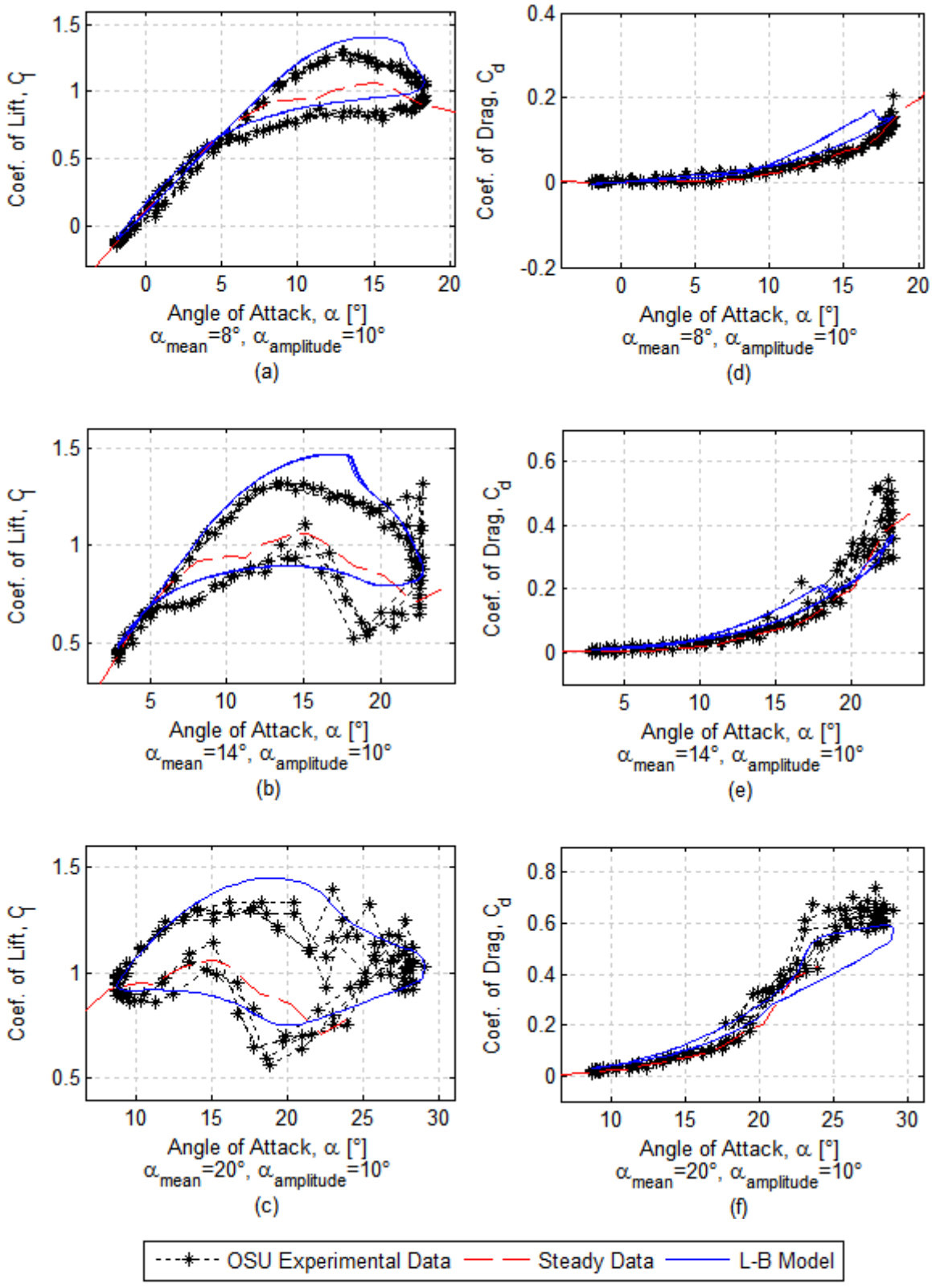

Figure A.8: C_L and C_D for the S809 Airfoil with time varying α, k = 0.035, Re = 1.40×10^6

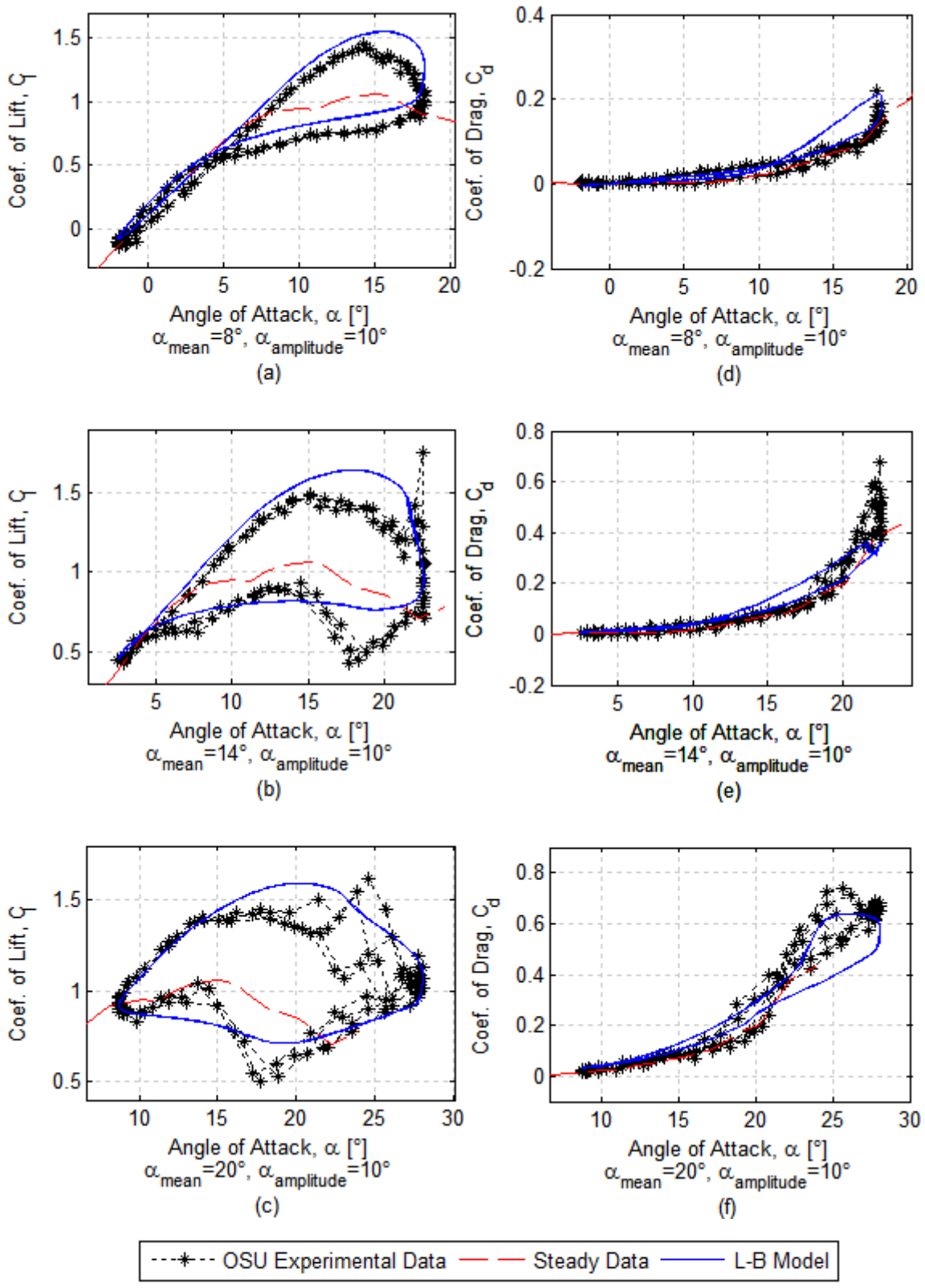

Figure A.9: C_L and C_D for the S809 Airfoil with time varying α, k = 0.053, Re = 1.40×10^6

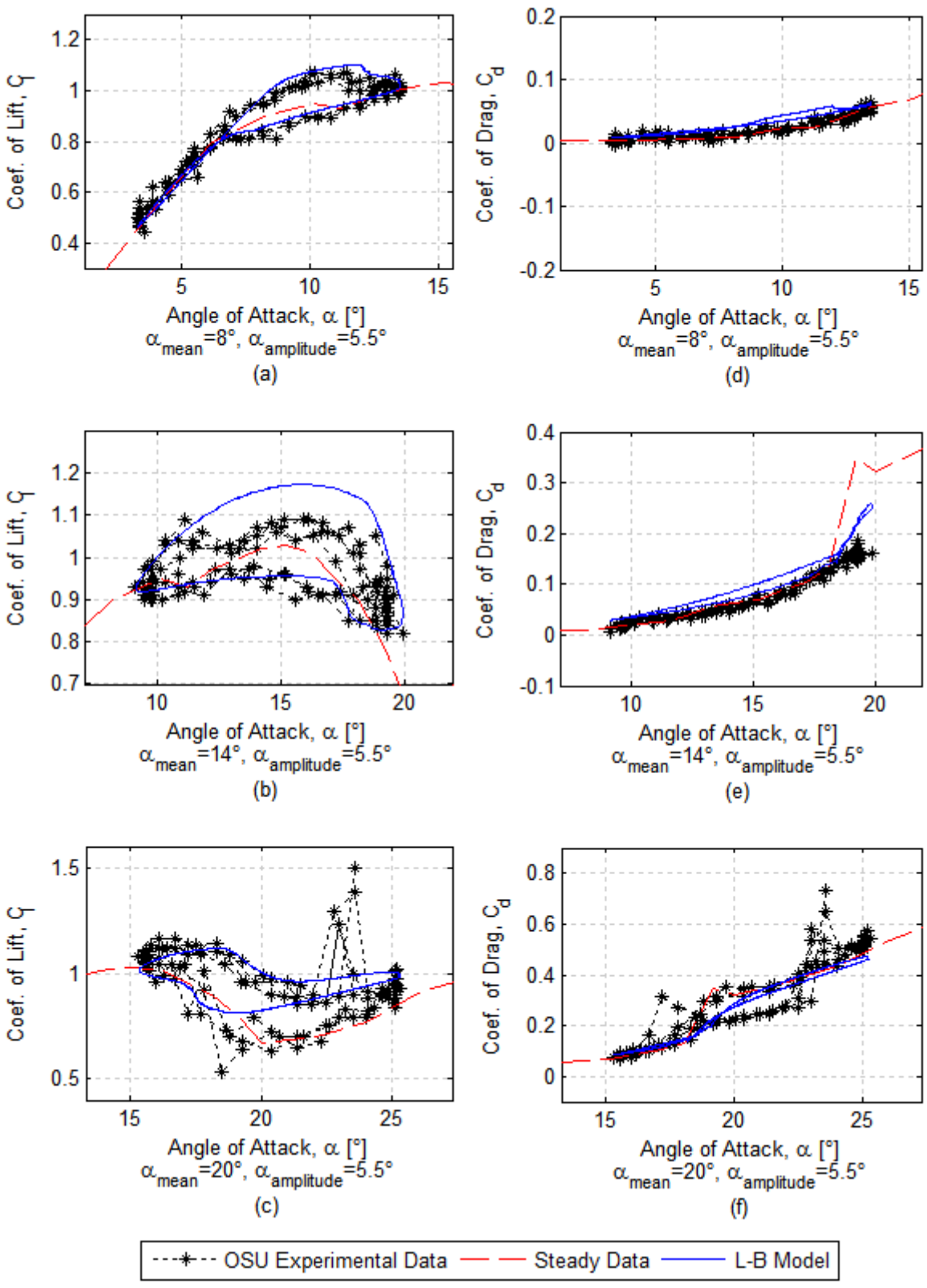

Figure A.10: C_L and C_D for the S809 Airfoil with time varying α, k = 0.026, Re = 1. 0×10^6

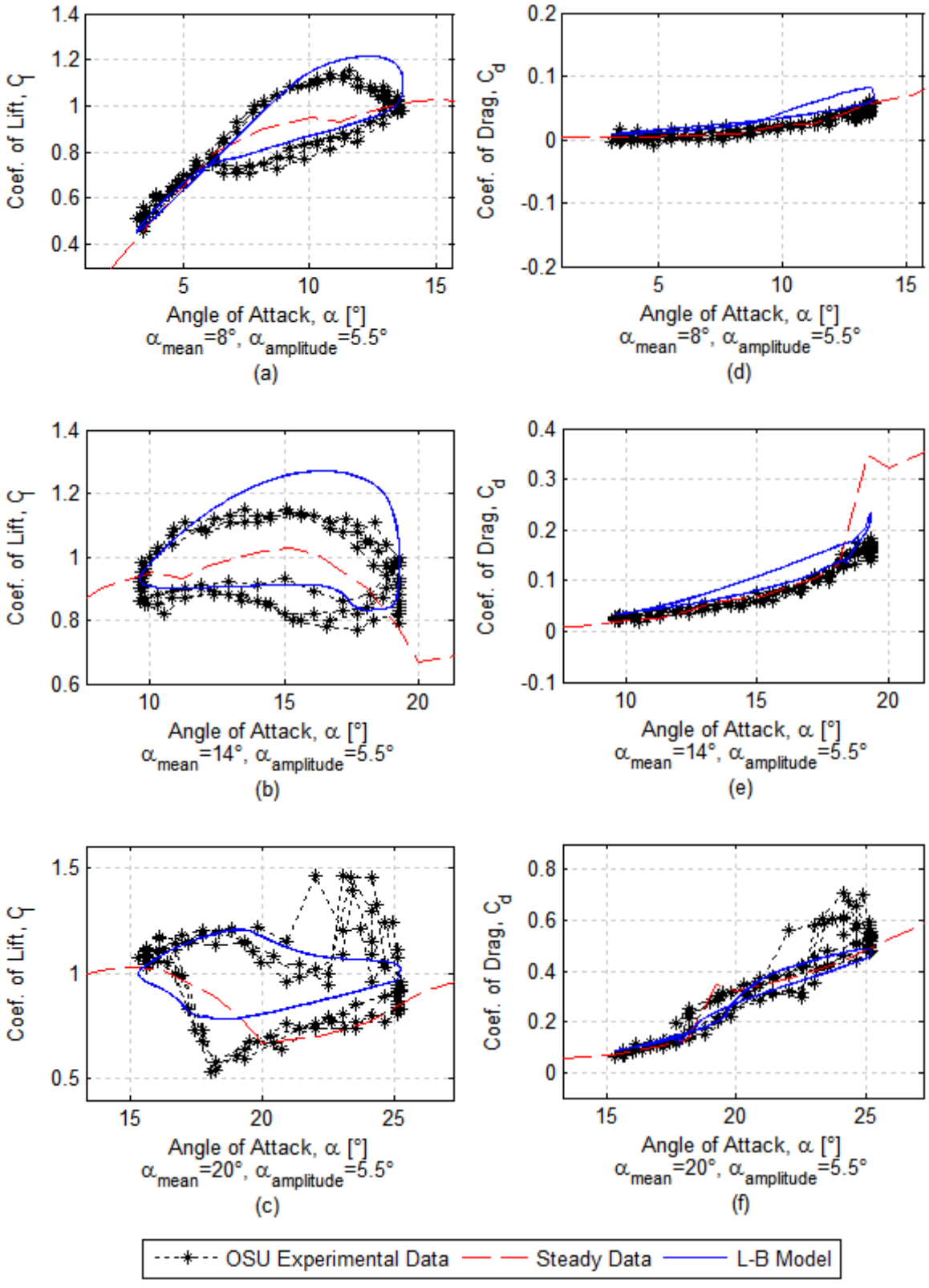

Figure A.11: C_L and C_D for the S809 Airfoil with time varying α, k = 0.049, Re = 1.0×10^6

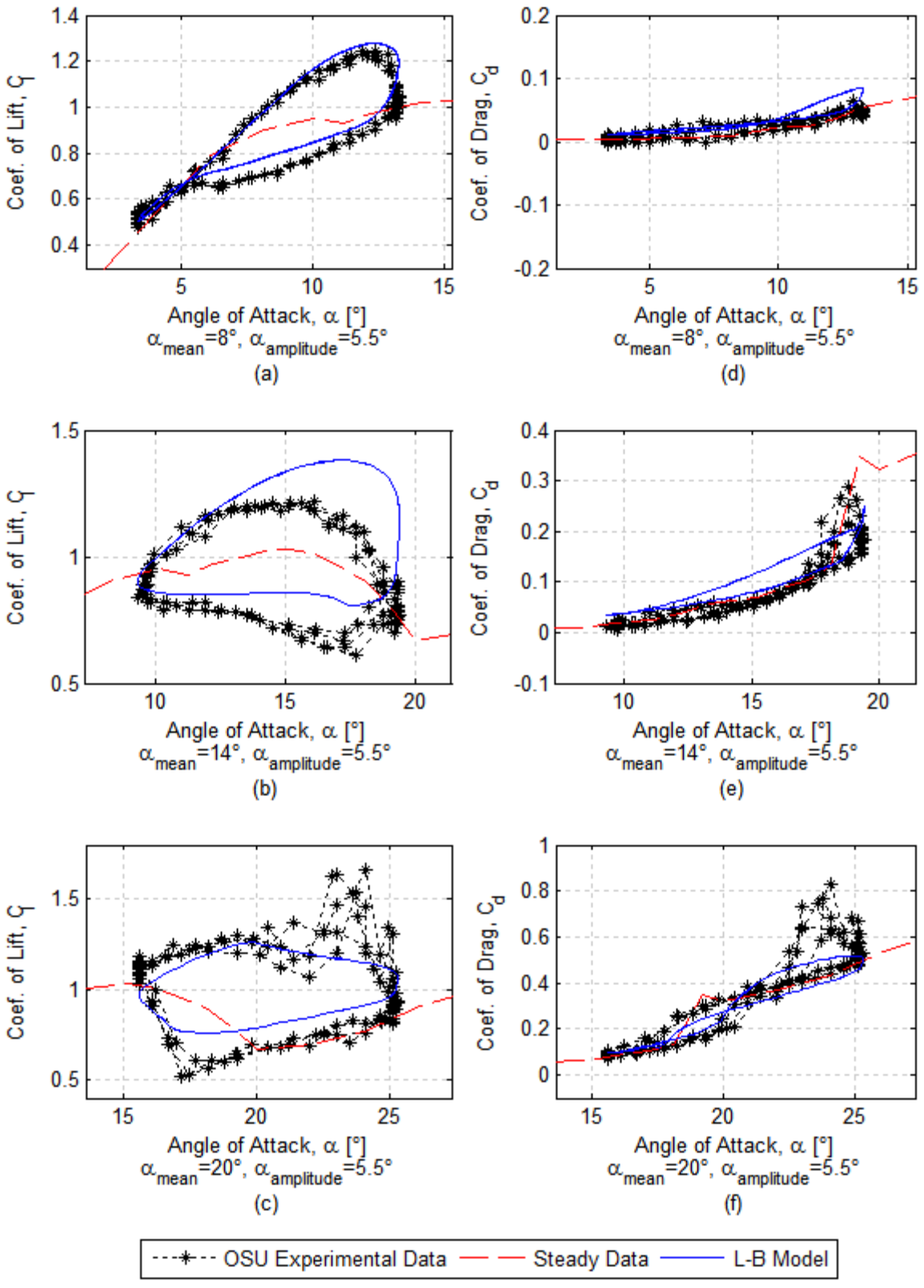

Figure A.12: C_L and C_D for the S809 Airfoil with time varying α, k = 0.077, Re = 1.0×10^6

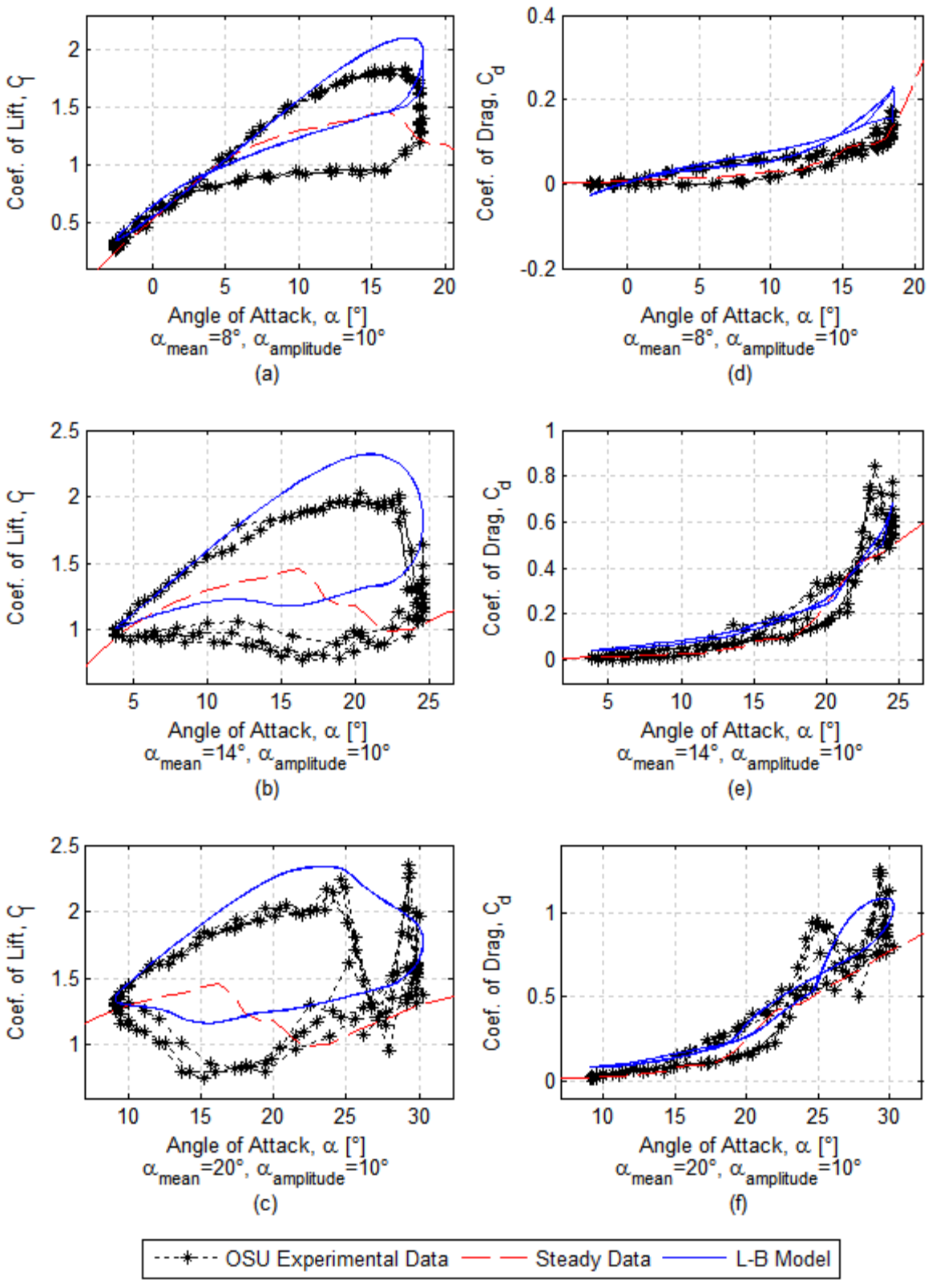

Figure A.13: C_L and C_D for the S801 Airfoil with time varying α, k = 0.079, Re = 1.0×10^6

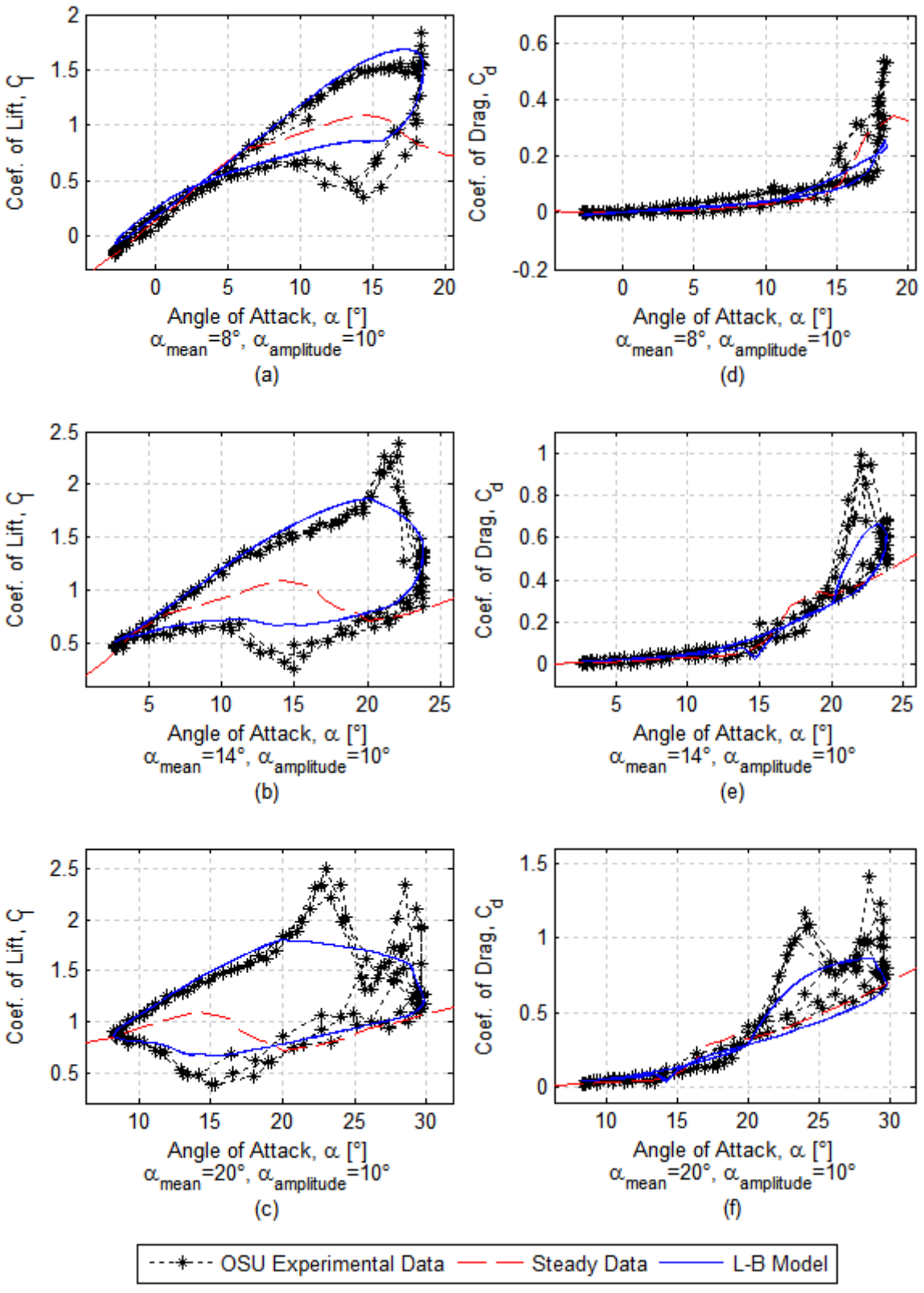

Figure A.14: C_L and C_D for the S810 Airfoil with time varying α, k = 0.082, Re = 1.0×10^6

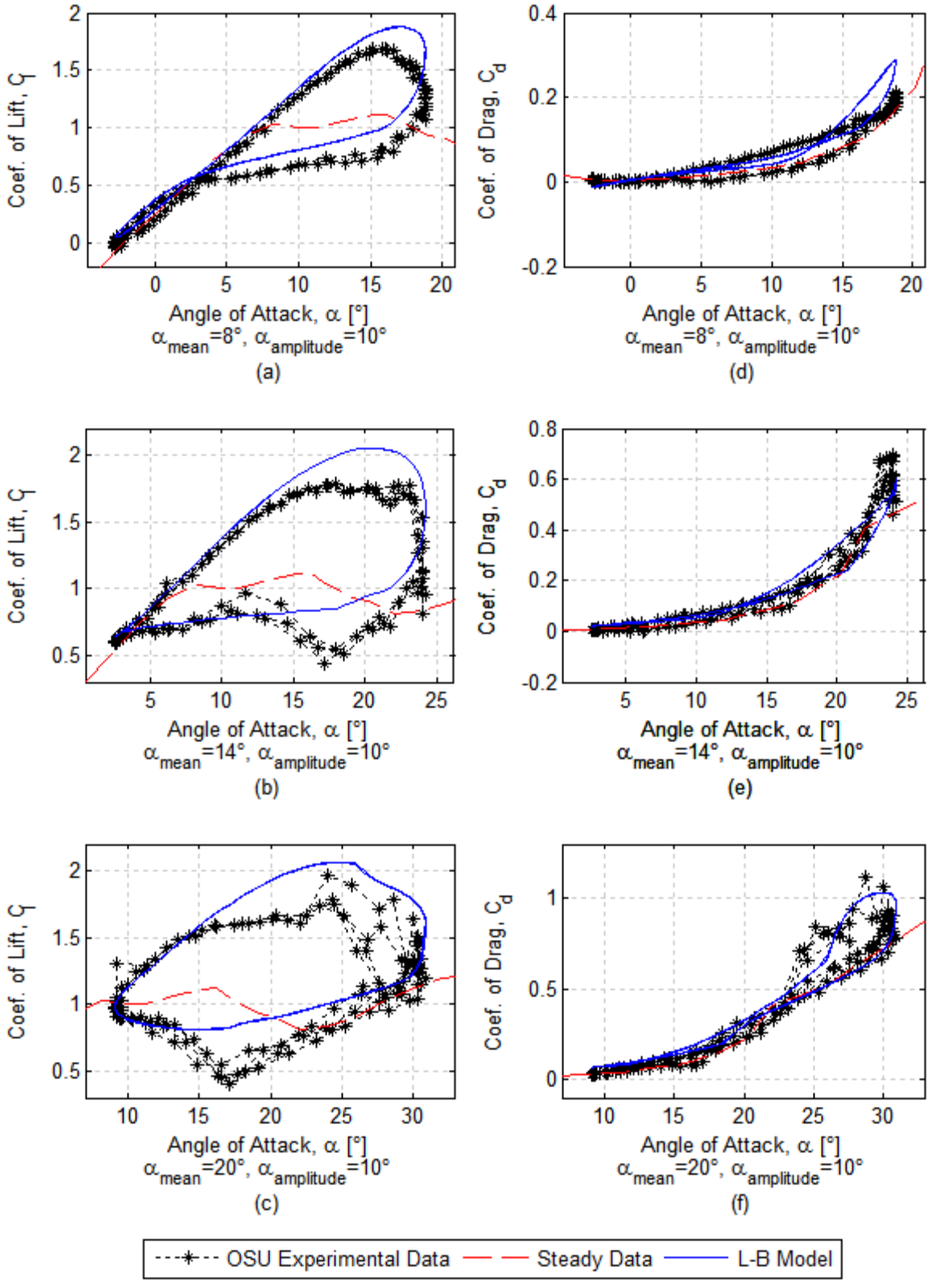

Figure A.15: C_L and C_D for the S812 Airfoil with time varying α, k = 0.088, Re = 1.0×10^6

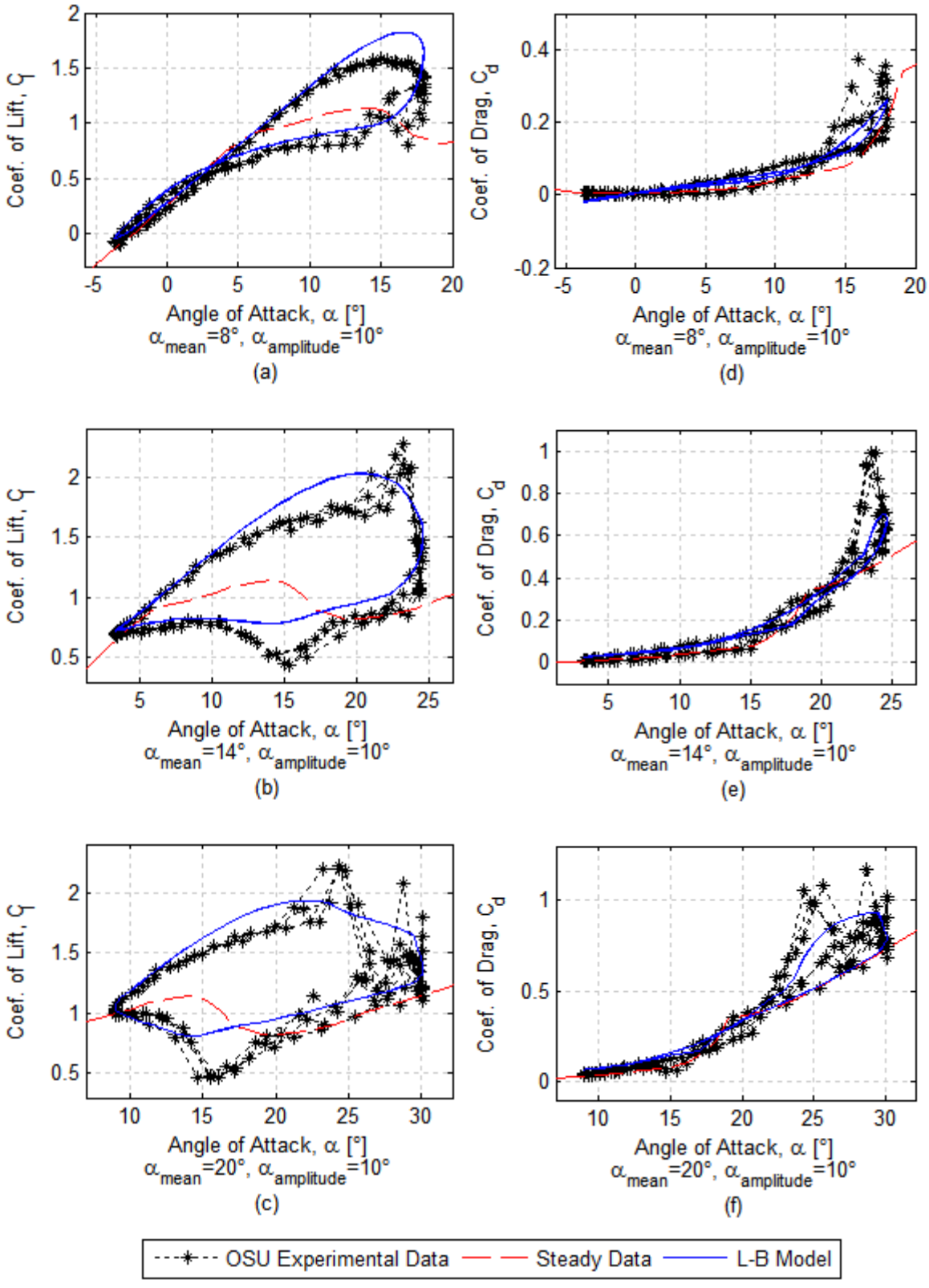

Figure A.16: C_L and C_D for the S813 Airfoil with time varying α, k = 0.083, Re = 1.0×10^6

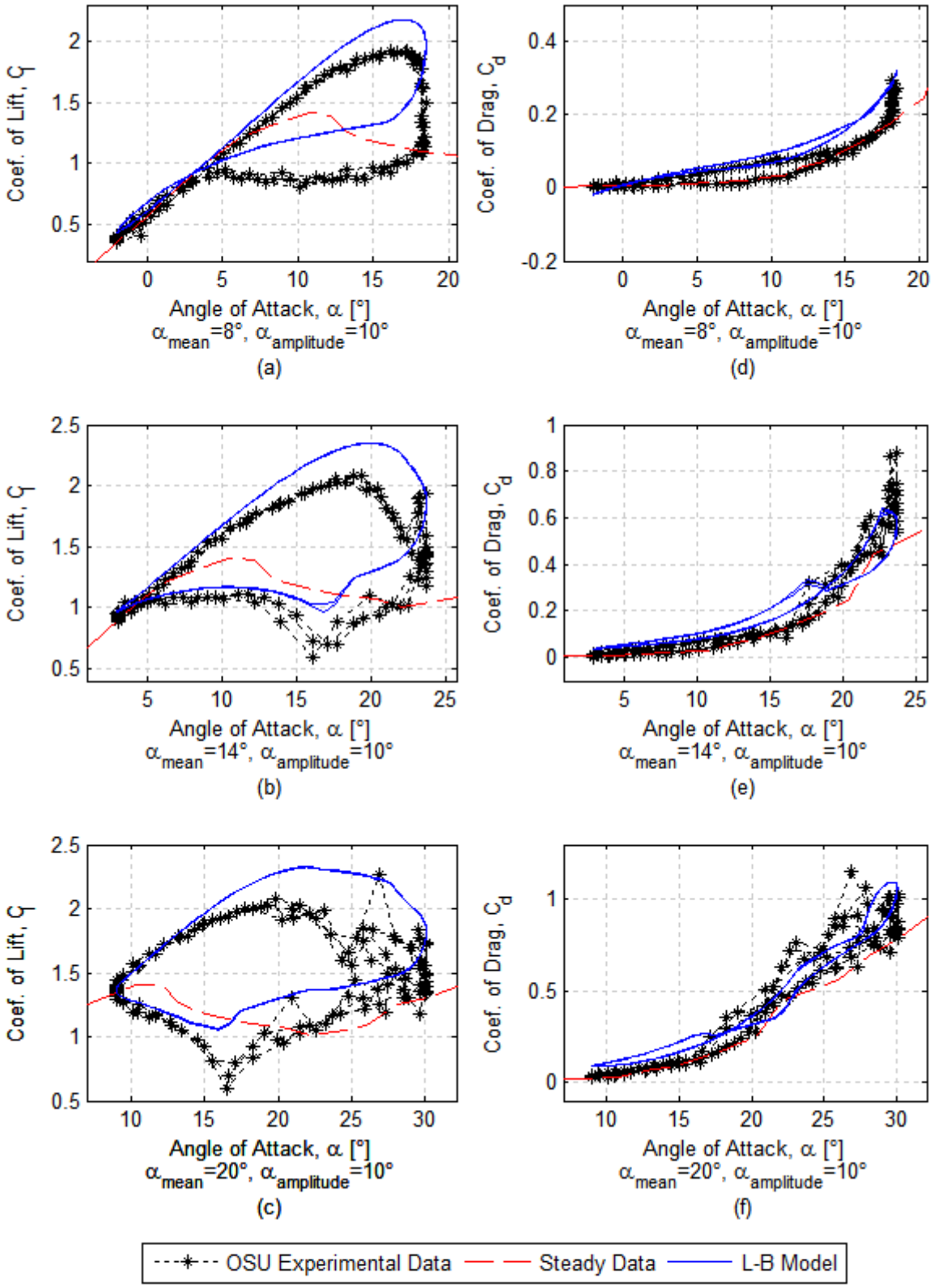

Figure A.17: C_L and C_D for the S825 Airfoil with time varying α, k = 0.081, Re = 1.0×10^6

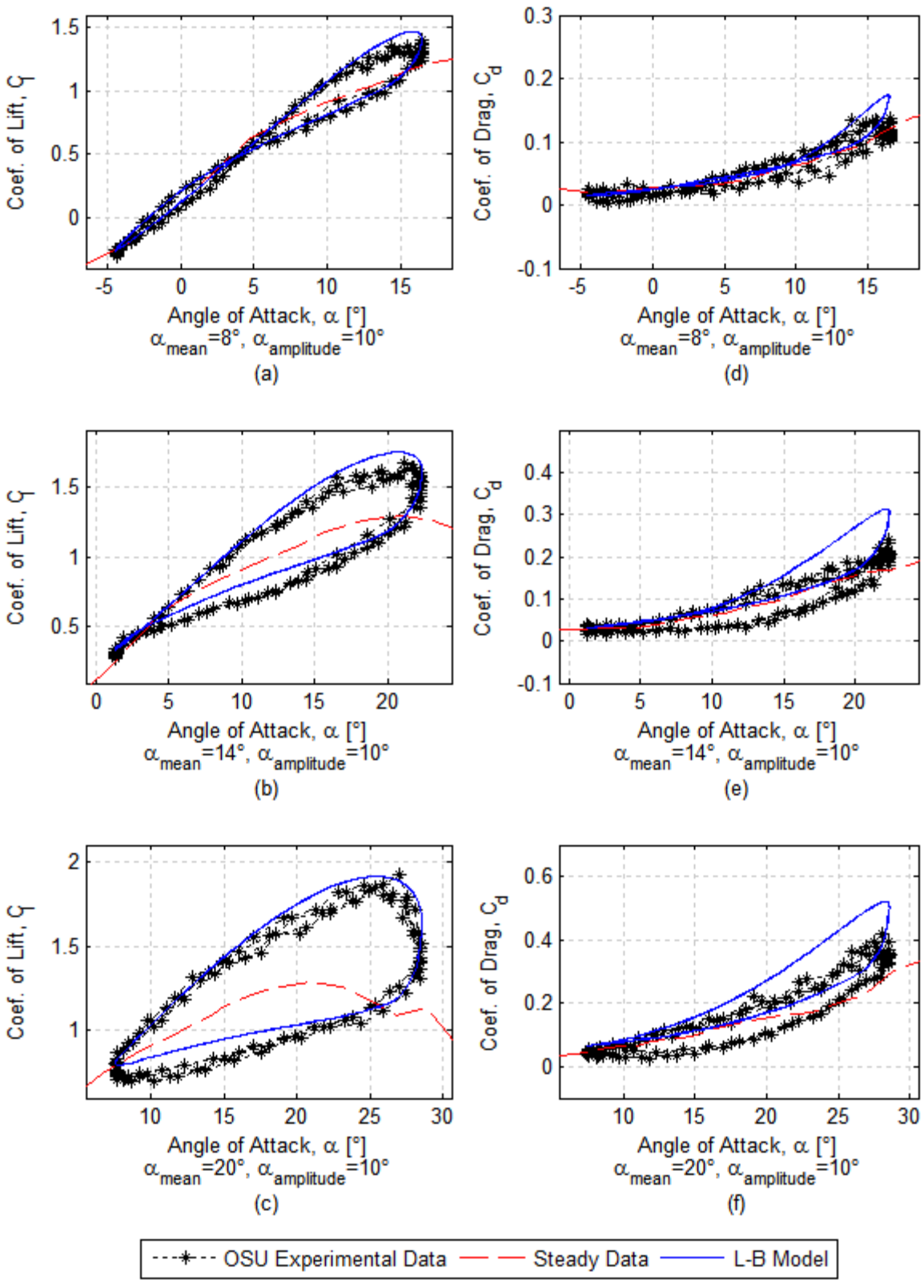

Figure A.18: C_L and C_D for the L303 Airfoil with time varying α, k = 0.078, Re = 1.0×10^6

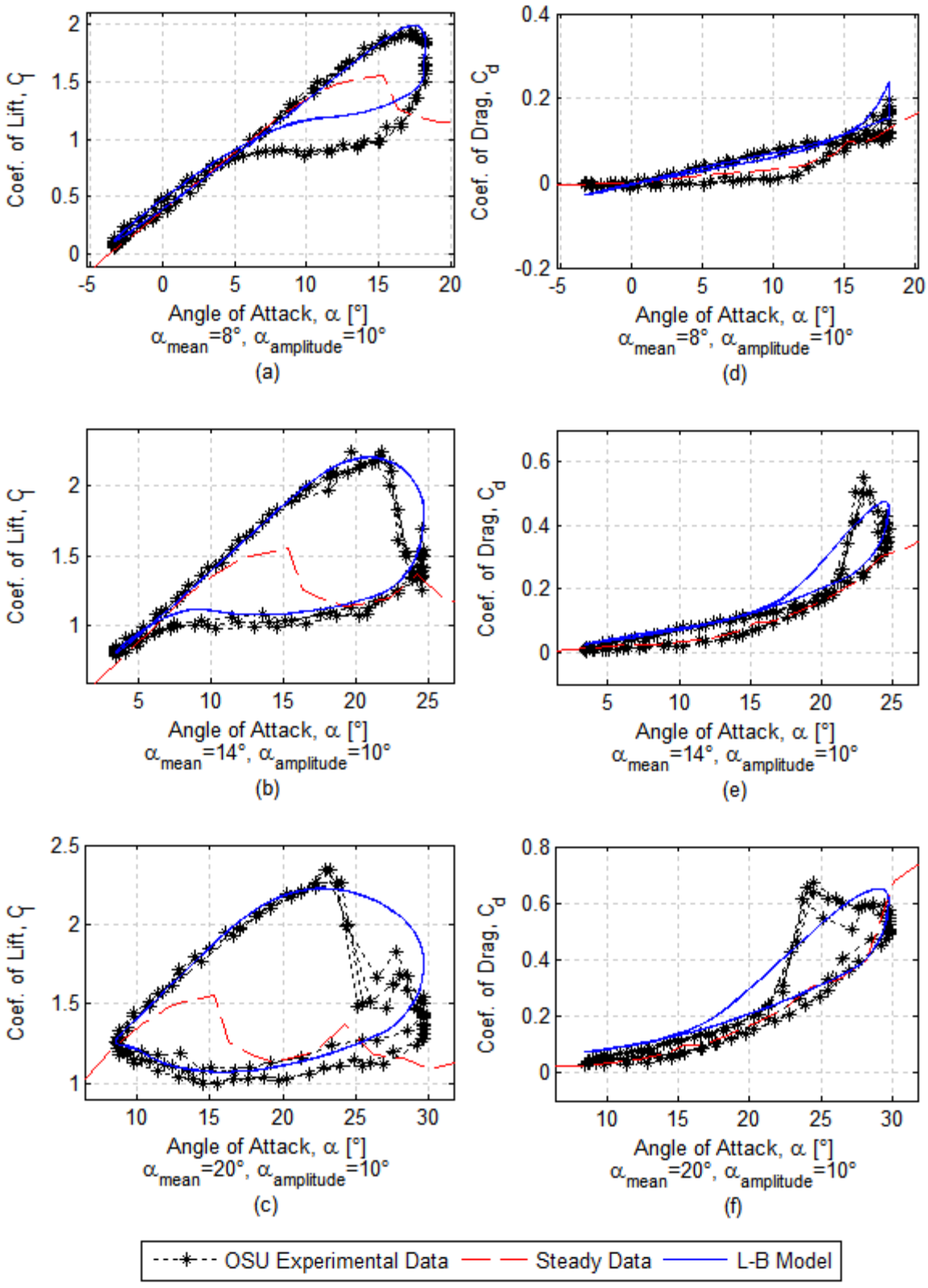

Figure A.19: C_L and C_D for the LS(1)-0417MOD Airfoil with time varying α, k = 0.082, Re = 1.0×106

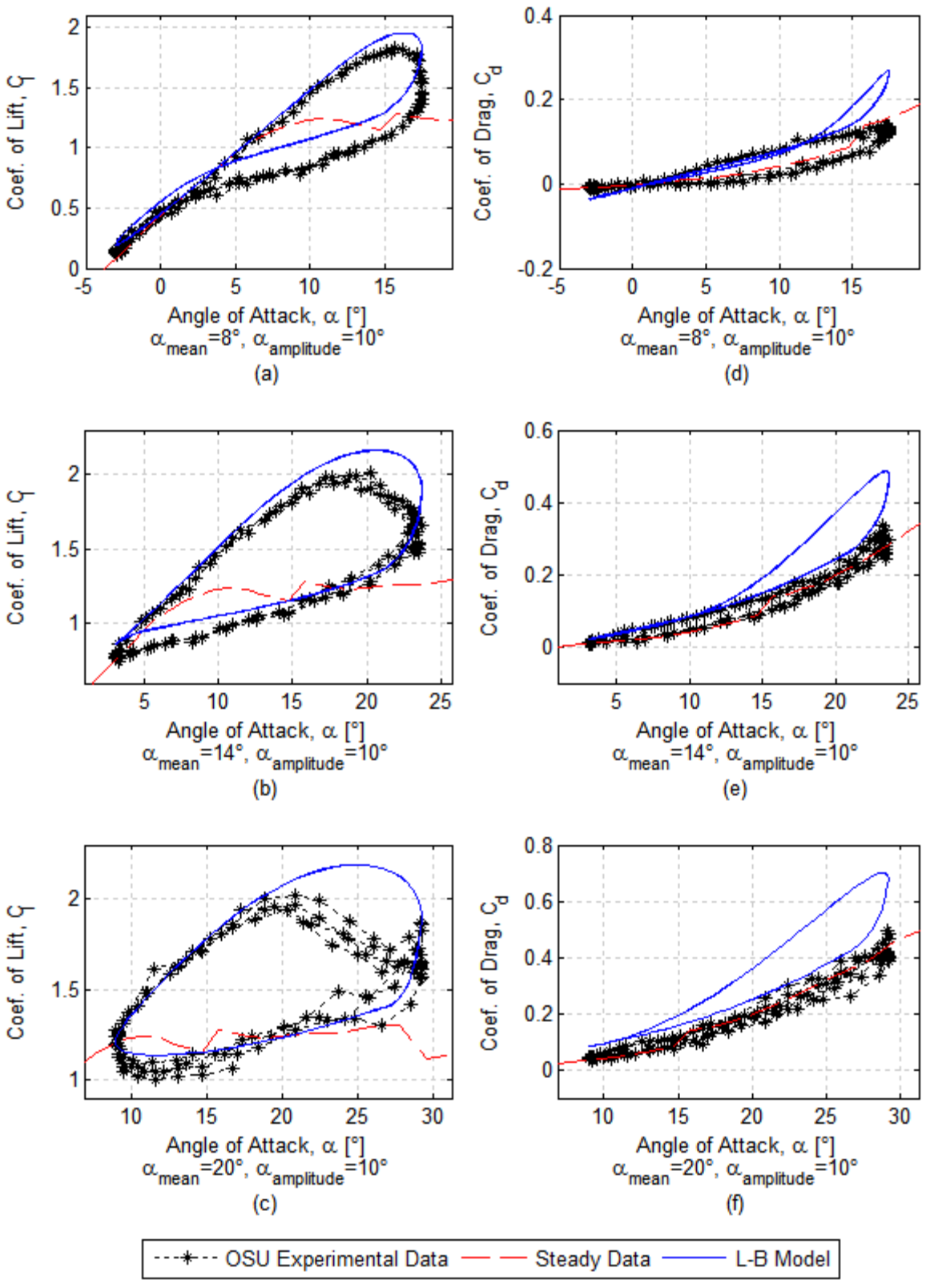

Figure A.20: C_L and C_D for the LS(1)-0421MOD Airfoil with time varying α, k = 0.082, Re = 1.0×106

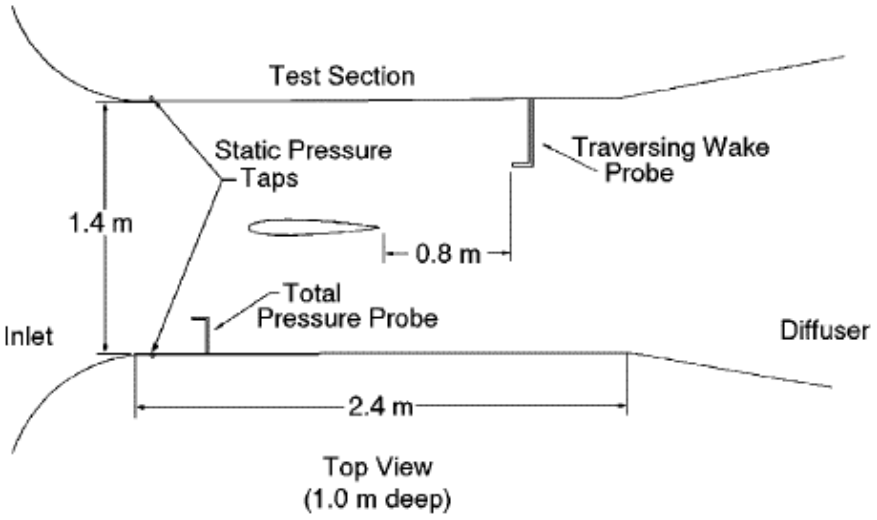

Figure A.21: Diagram of the OSU 3x5 wind tunnel

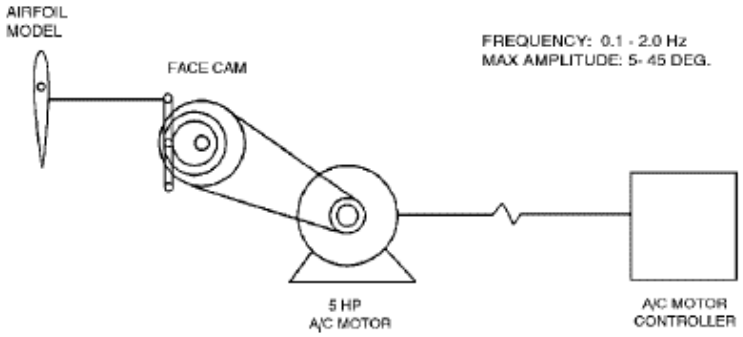

Figure A.22: Diagram of the OSU 3x5 wind tunnel pitch oscillation system

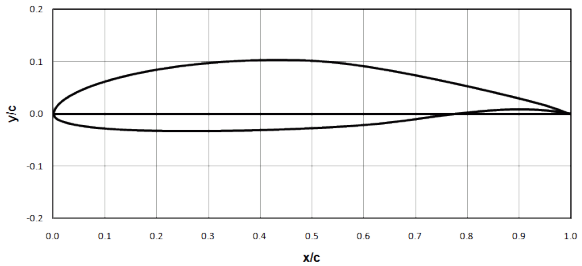

Figure A.23: S801 Airfoil Profile

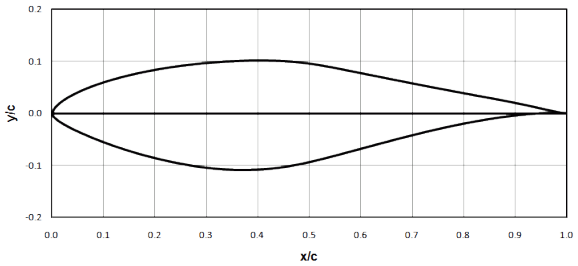

Figure A.24: S809 Airfoil Profile

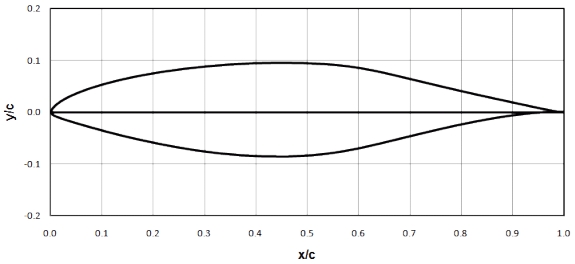

Figure A.25: S810 Airfoil Profile

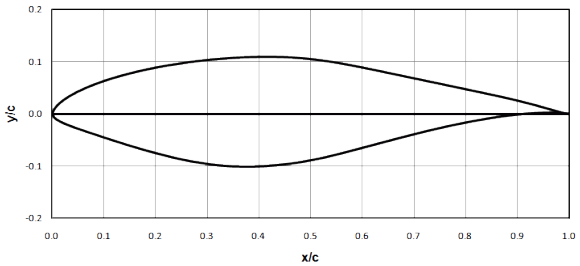

Figure A.26: S812 Airfoil Profile

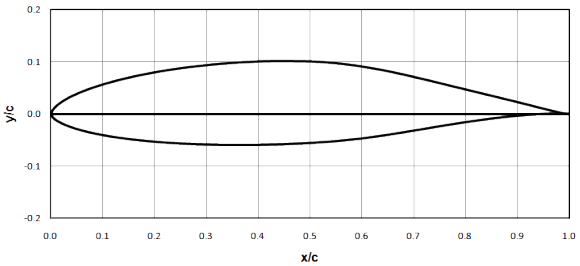

Figure A.27: S813 Airfoil Profile

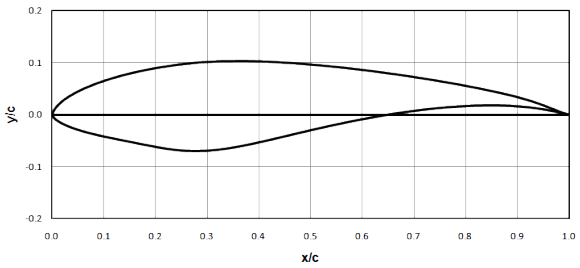

Figure A.28: S825 Airfoil Profile

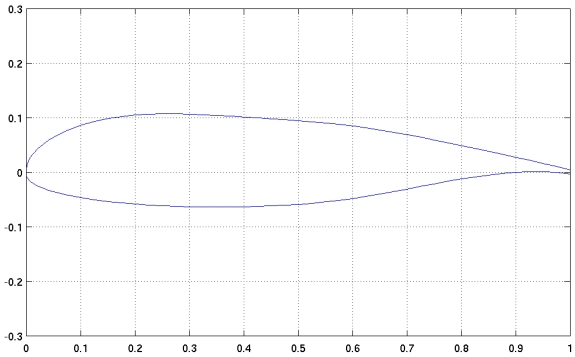

Figure A.29: NASA/Langley LS(1)-0417MOD

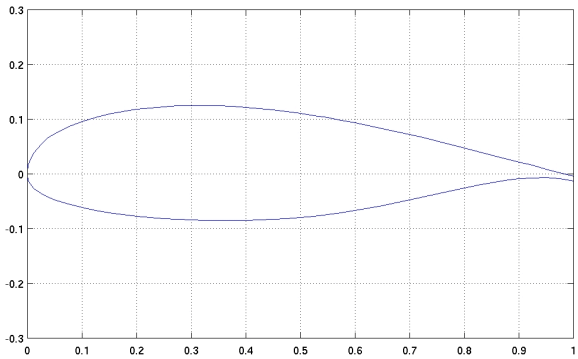

Figure A.30: NASA/Langley LS(1)-0421MOD

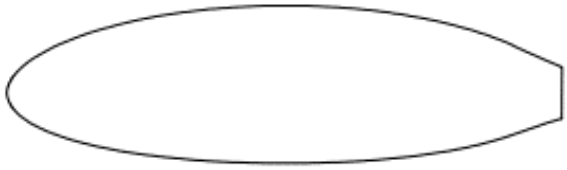

Figure A.31: L303 Airfoil Profile

APPENDIX B

SUPPLEMENTAL INFORMATION ON UAE PHASE VI TEST BLADE

Figure B.1: Photograph of the UAE Phase VI test turbine in the NASA/Ames wind tunnel

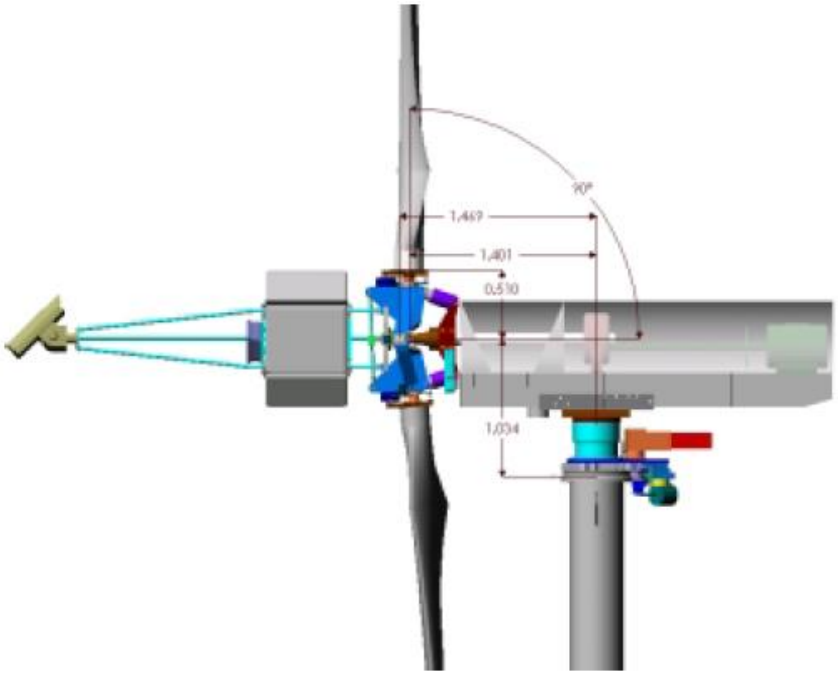

Figure B.2: Diagram of the UAE Phase VI test turbine

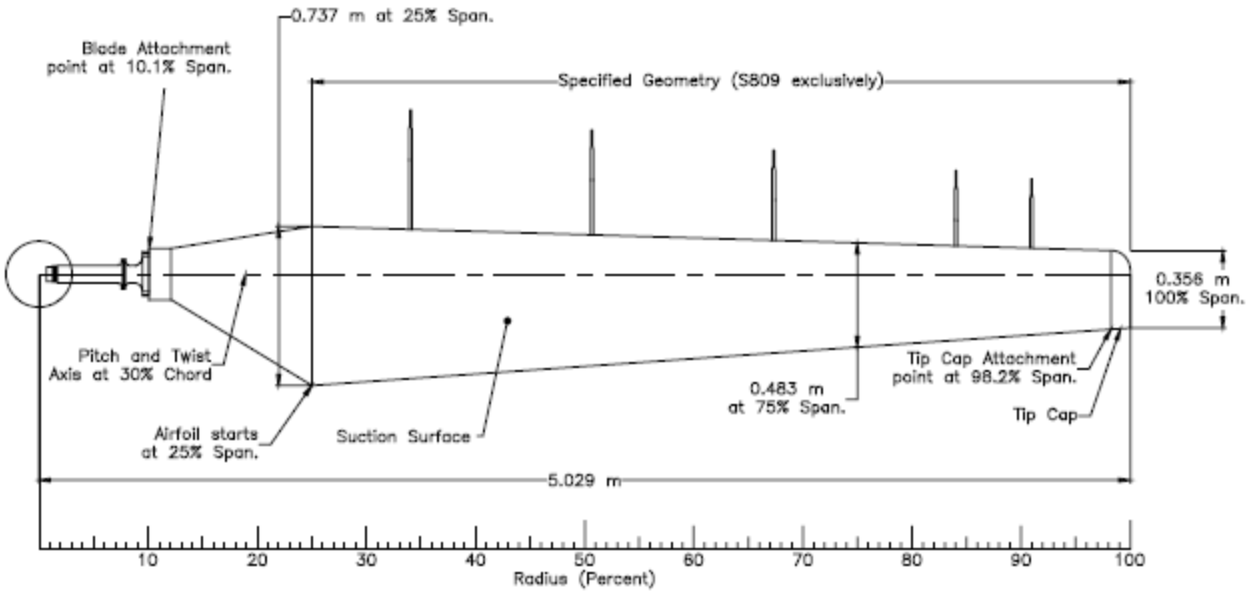

Figure B.3: Diagram of UAE Phase VI blade

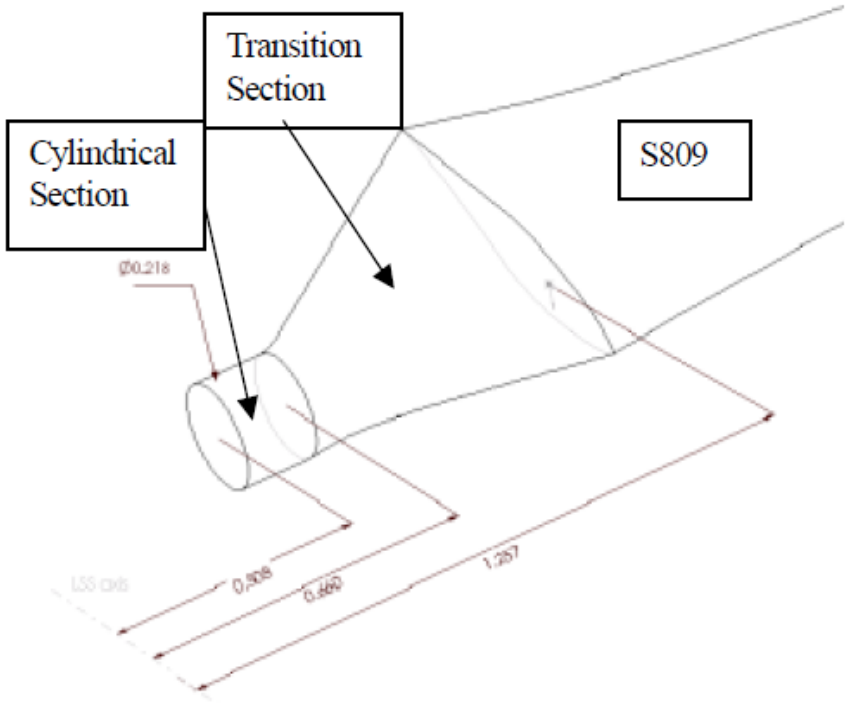

Figure B.4: UAE Phase VI blade root

Table B.1: UAE distributed blade properties

Radius [m]	r/R	Chord [m]	Twist Angle [°]	Airfoil
0.000	0.000	--	--	Hub
0.508	0.092	0.218	0.000	Hub/Cylinder
0.660	0.131	0.218	0.000	Cylinder
0.884	0.176	0.183	0.000	Cylinder
1.009	0.200	0.349	6.700	Transition
1.068	0.212	0.441	9.900	Transition
1.134	0.225	0.544	13.400	Transition
1.258	0.250	0.737	20.040	Transition
1.343	0.267	0.728	18.074	Transition/S809
1.510	0.300	0.711	14.292	S809
1.648	0.328	0.697	11.909	S809
1.952	0.388	0.666	7.979	S809
2.257	0.449	0.636	5.308	S809
2.343	0.466	0.627	4.715	S809
2.562	0.509	0.605	3.425	S809
2.867	0.570	0.574	2.083	S809
3.172	0.631	0.543	1.150	S809
3.185	0.633	0.542	1.115	S809
3.476	0.691	0.512	0.494	S809
3.781	0.752	0.482	-0.015	S809
4.023	0.800	0.457	-0.381	S809
4.086	0.812	0.451	-0.475	S809
4.391	0.873	0.420	-0.920	S809
4.696	0.934	0.389	-1.352	S809
4.780	0.950	0.381	-1.469	S809
5.000	0.994	0.358	-1.775	S809
5.029	1.000	0.355	-1.815	S809

*Table B.2: S809 Airfoil Data from OSU at Re = 750,000 **

α [deg]	C_l	C_d	C_m		α [deg]	C_l	C_d	C_m
-180	0	0.3021	0		10.2	0.93	0.0274	-0.0321
-170	0.235	0.3369	0.4		11.3	0.92	0.0303	-0.0281
-160	0.47	0.4369	0.0233		12.1	0.95	0.0369	-0.0284
-150	0.605	0.5886	0.0916		13.2	0.99	0.0509	-0.0322
-140	0.578	0.7718	0.1385		14.2	1.01	0.0648	-0.0361
-130	0.526	0.9617	0.1847		15.3	1.02	0.0776	-0.0363
-120	0.437	1.132	0.2275		16.3	1	0.0917	-0.0393
-110	0.312	1.2583	0.2626		17.1	0.94	0.0994	-0.0398
-100	0.161	1.321	0.2857		18.1	0.85	0.2306	-0.0983
-90	0	1.308	0.2936		19.1	0.7	0.3142	-0.1242
-80	-0.161	1.321	0.312		20.1	0.66	0.3186	-0.1155
-70	-0.312	1.2583	0.3152		22	0.7	0.3694	-0.1265
-60	-0.437	1.132	0.3051		24.1	0.79	0.4457	-0.1488
-50	-0.526	0.9617	0.2859		26.2	0.88	0.526	-0.1723
-40	-0.578	0.7718	0.2641		30	0.864	0.5886	-0.1927
-30	-0.605	0.5886	0.2507		40	0.825	0.7718	-0.24
-20.1	-0.56	0.3027	0.0612		50	0.751	0.9617	-0.2808
-18.1	-0.67	0.3069	0.0904		60	0.624	1.132	-0.3146
-16.1	-0.79	0.1928	0.0293		70	0.445	1.2583	-0.3398
-14.2	-0.84	0.0898	-0.009		80	0.23	1.321	-0.3553
-12.2	-0.7	0.0553	-0.0045		90	0	1.308	-0.0334
-10.1	-0.63	0.039	-0.0044		100	-0.161	1.321	-0.3787
-8.2	-0.56	0.0233	-0.0051		110	-0.312	1.2583	-0.3819
-6.1	-0.64	0.0112	0.0018		120	-0.437	1.132	-0.3719
-4.1	-0.42	-0.0004	-0.0216		130	-0.526	0.9617	-0.3526
-2.1	-0.21	-0.0003	-0.0282		140	-0.578	0.7718	-0.3308
0.1	0.05	0.0029	-0.0346		150	-0.605	0.5886	-0.3174
2	0.3	0.0056	-0.0405		160	-0.47	0.4369	-0.2723
4.1	0.54	0.0067	-0.0455		170	-0.235	0.3369	-0.5
6.2	0.79	0.0085	-0.0507		180	0	0.3021	0
8.1	0.9	0.0127	-0.0404					

* Data from Hand, et al. (2001), extended to full 360° using Viterna extrapolation method in FoilCheck (Laino & Hansen, 2002)

APPENDIX C

SUPPLEMENTAL WINDS SIMULATIONS OF UAE PHASE VI SEQUENCE S YAWED TEST CASES

This Appendix contains supplementary figures for the data summarized in Tables 5.2, 5.3, and 5.4 for UAE Phase VI Sequence S Yawed test cases modelled in WInDS. Section 5.2.3 shows results for 10 m/s with 30° and 60° yaw. Cases at 10 m/s with 10 yaw, 13 m/s with 10, 30, and 60 yaw, and 15 m/s with 10 and 30 yaw are shown in this section. Figures C.1 to C.6 show the distributed span-wise coefficients of normal and chord force. Figures C.7 to C.12 show the total thrust and torque on a single blade and the total aerodynamic power for the rotor.

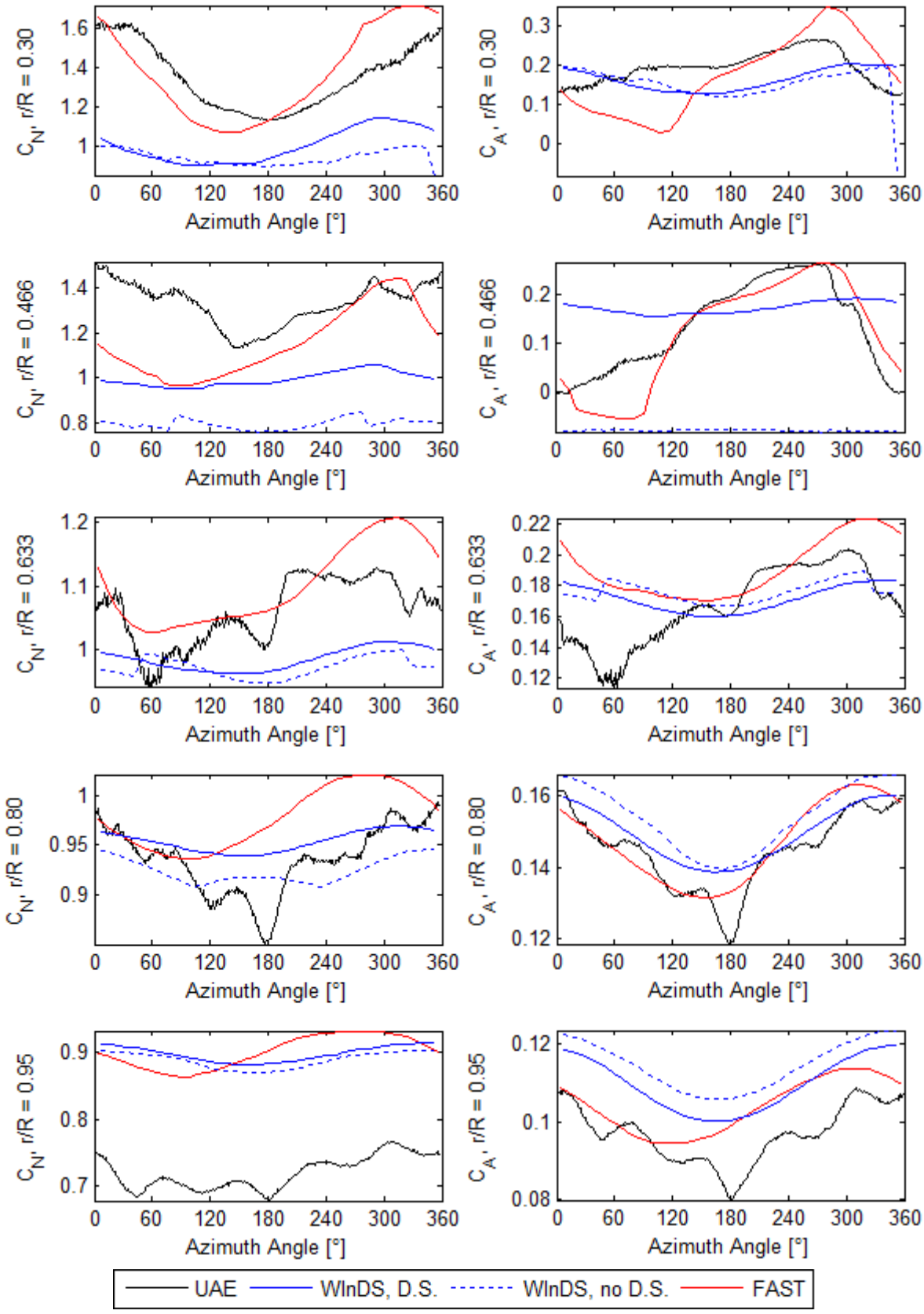

Figure C.1: Span distributed C_N and C_A for UAE Seq. S, 10 m/s, 10° yaw

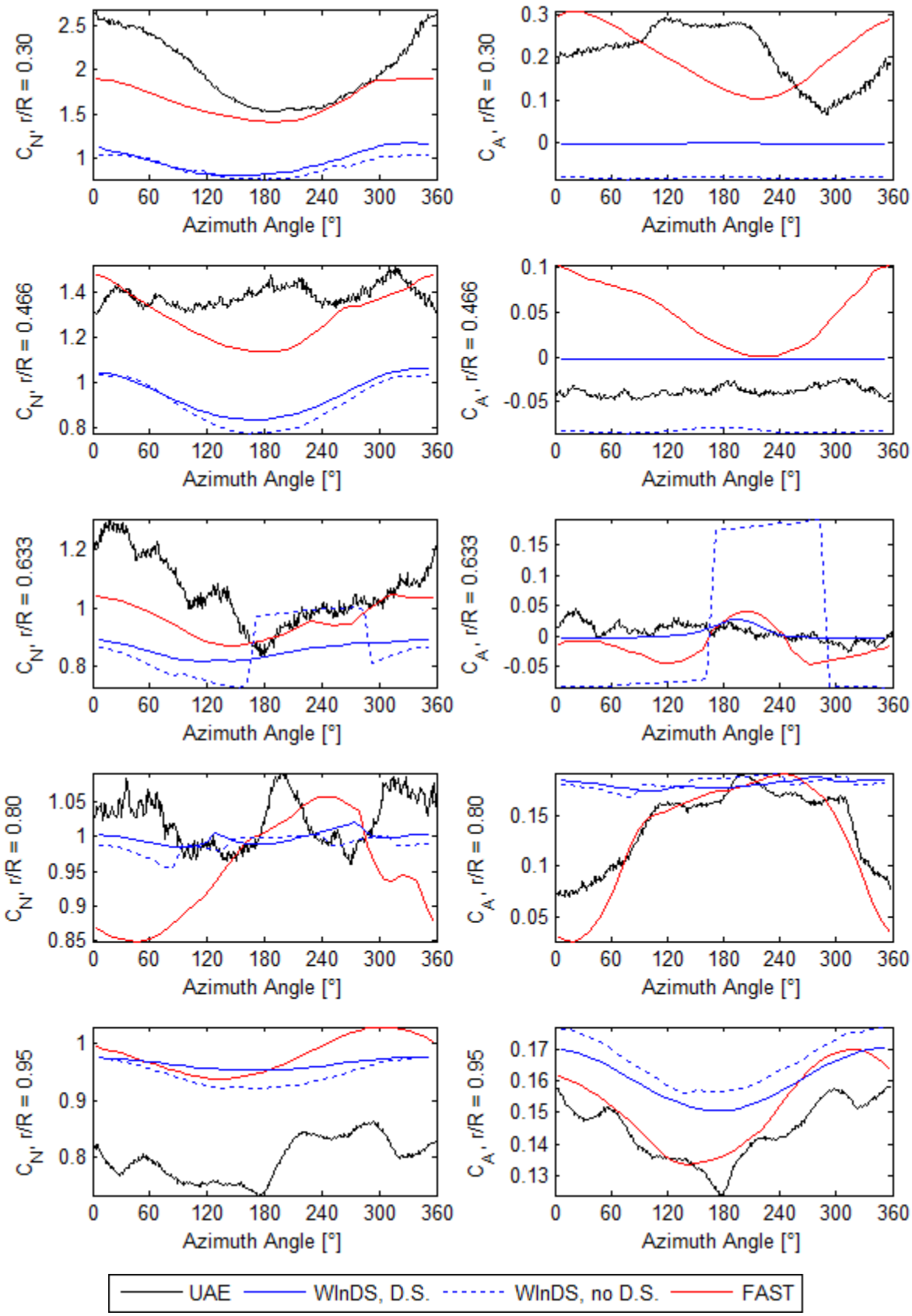

Figure C.2: Span distributed C_N and C_A for UAE Seq. S, 13 m/s, 10° yaw

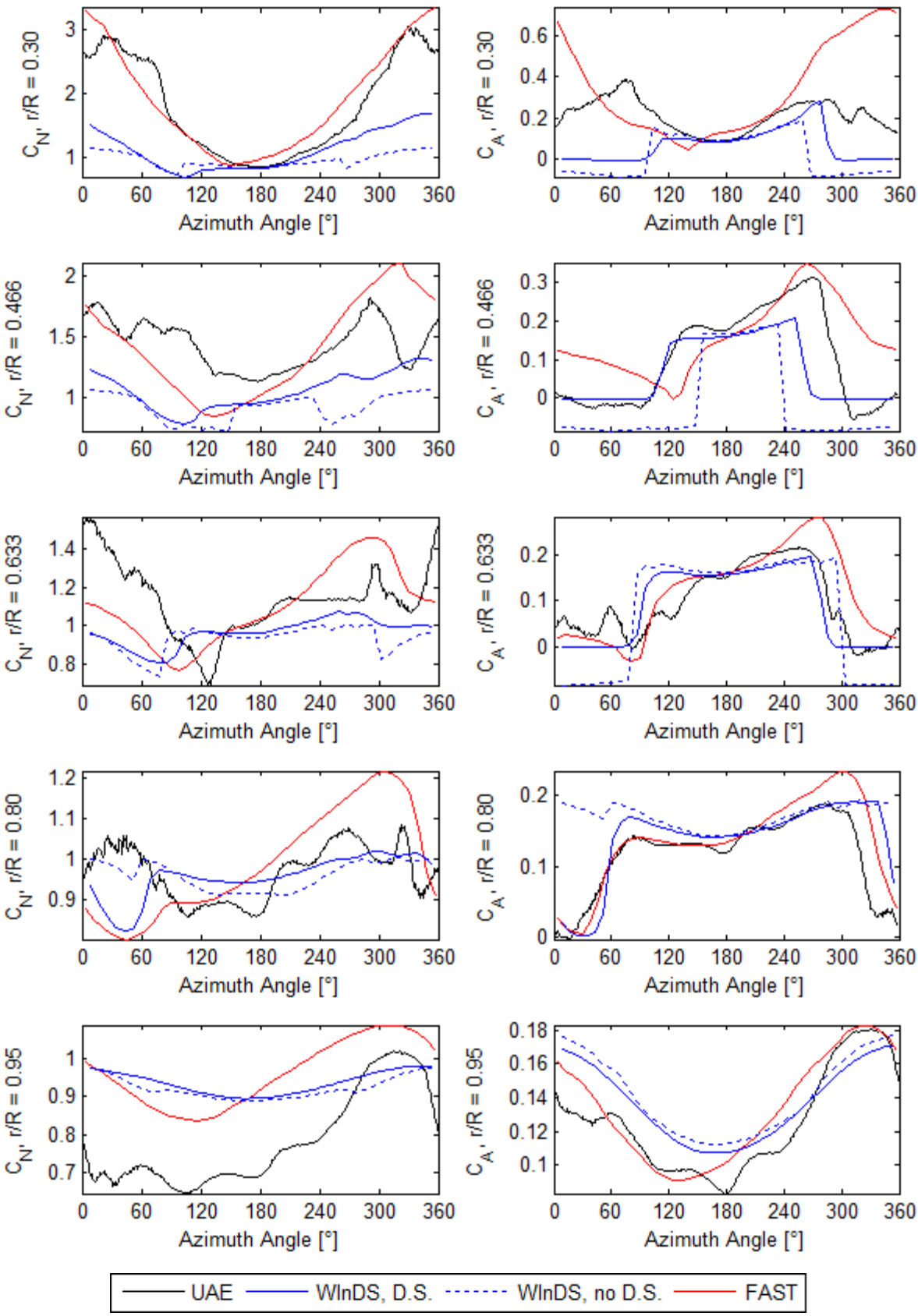

Figure C.3: Span distributed C_N and C_A for UAE Seq. S, 13 m/s, 30° yaw

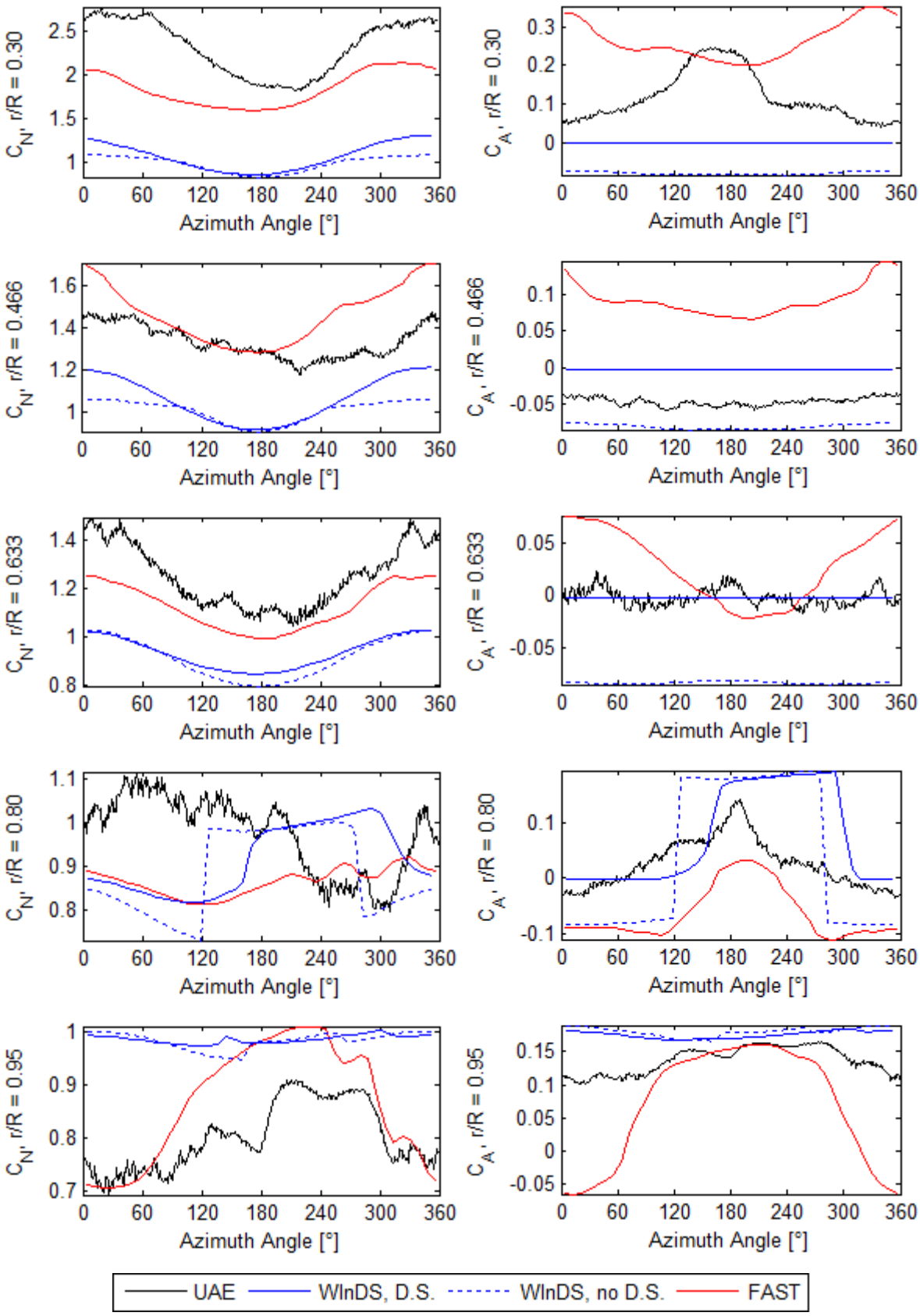

Figure C.4: Span distributed C_N and C_A for UAE Seq. S, 15 m/s, 10° yaw

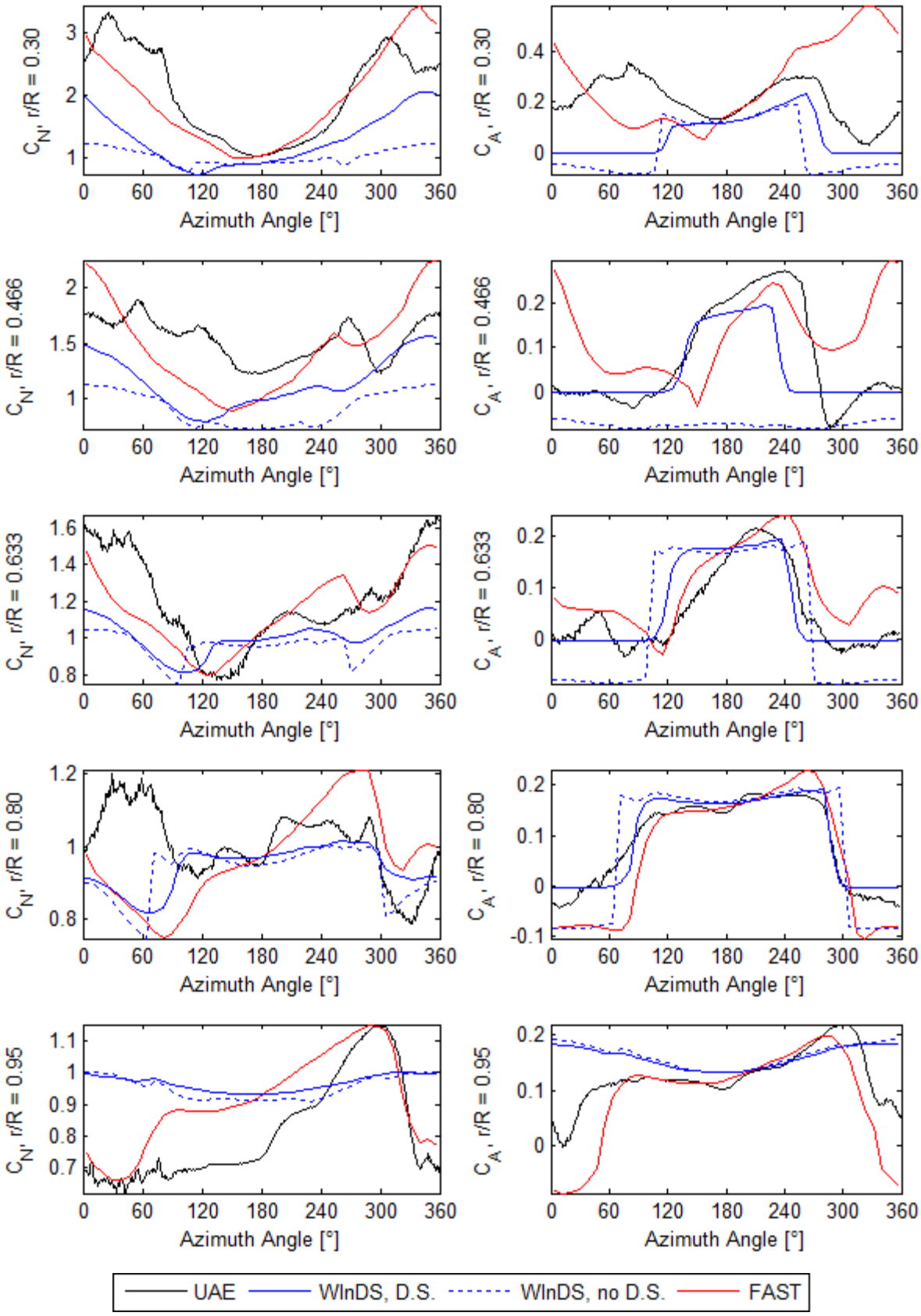

Figure C.5: Span distributed C_N and C_A for UAE Seq. S, 15 m/s, 30° yaw

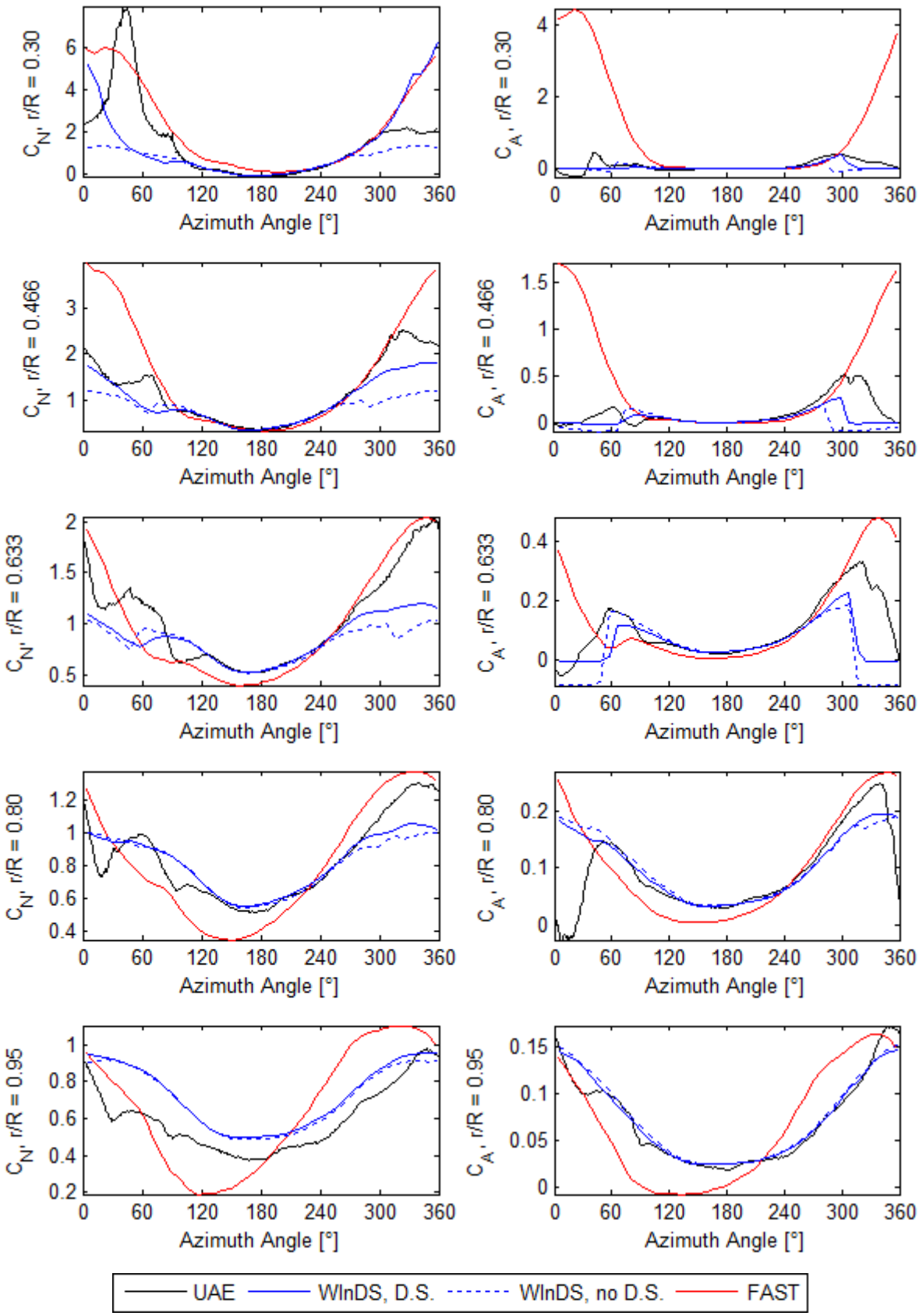

Figure C.6: Span distributed C_N and C_A for UAE Seq. S, 15 m/s, 60° yaw

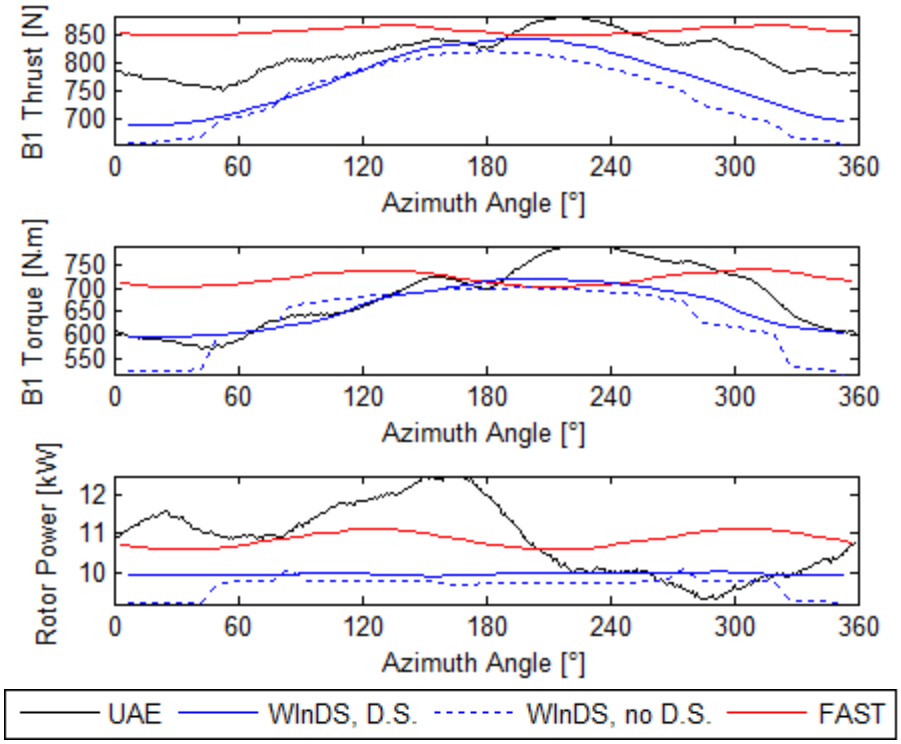

Figure C.7: Thrust and torque per blade and total aerodynamic rotor power for UAE Sequence S, 10 m/s, 10° yaw

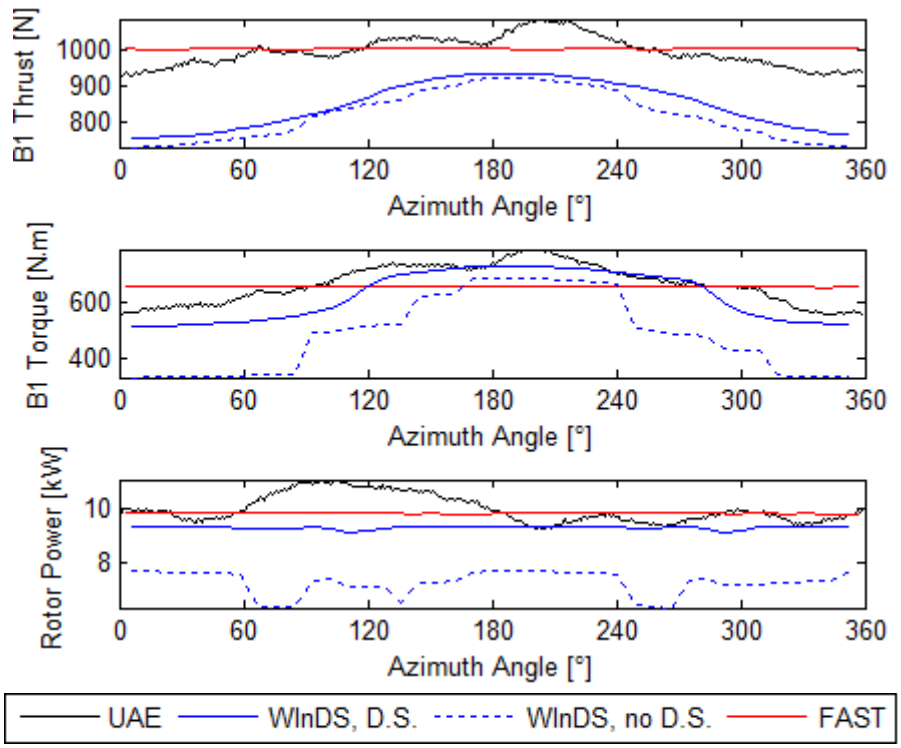

Figure C.8: Thrust and torque per blade and total aerodynamic rotor power for UAE Sequence S, 13 m/s, 10° yaw

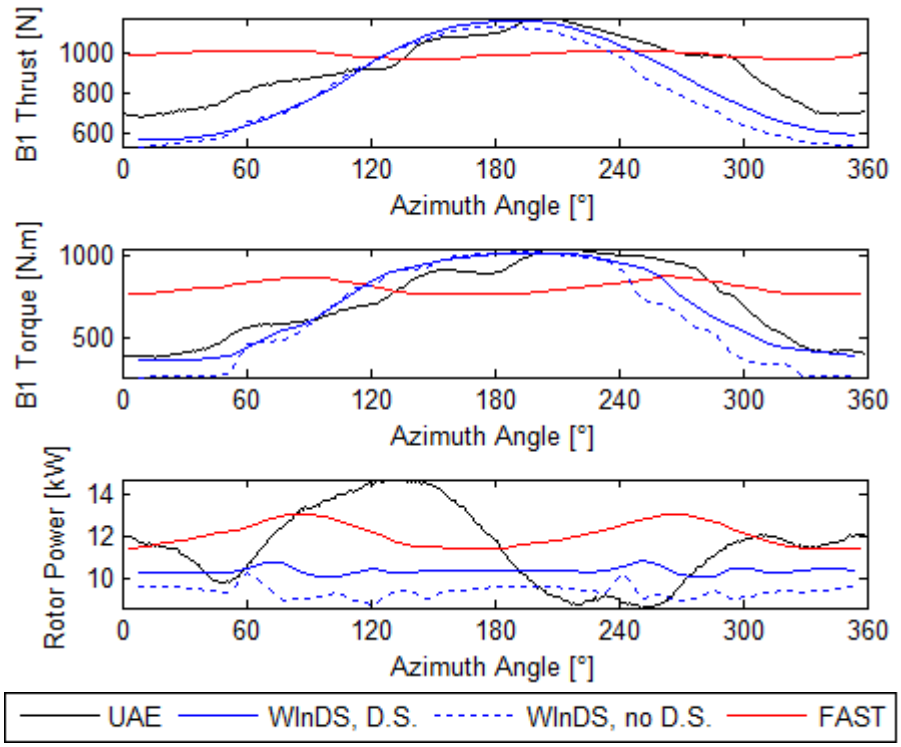

Figure C.9: Thrust and torque per blade and total aerodynamic rotor power for UAE Sequence S, 13 m/s, 30° yaw

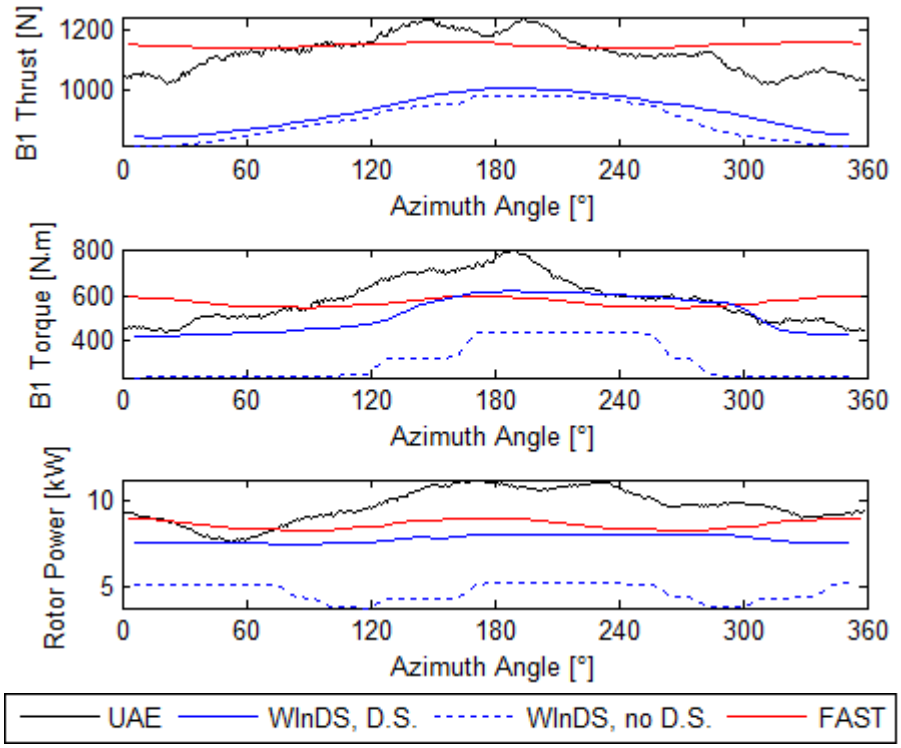

Figure C.10: Thrust and torque per blade and total aerodynamic rotor power for UAE Sequence S, 15 m/s, 10° yaw

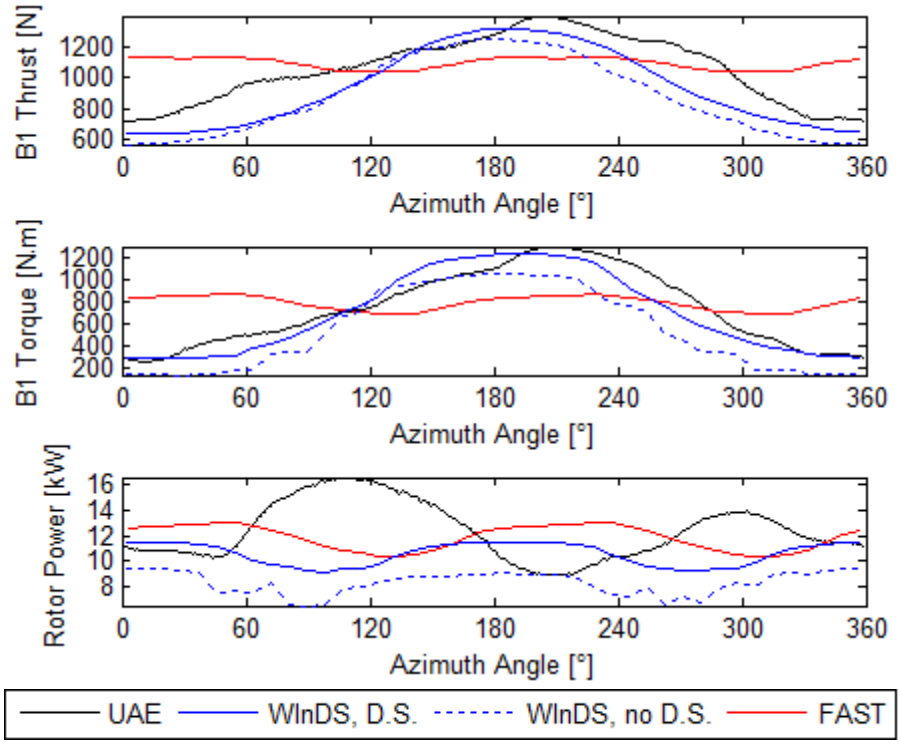

Figure C.11: Thrust and torque per blade and total aerodynamic rotor power for UAE Sequence S, 15 m/s, 30° yaw

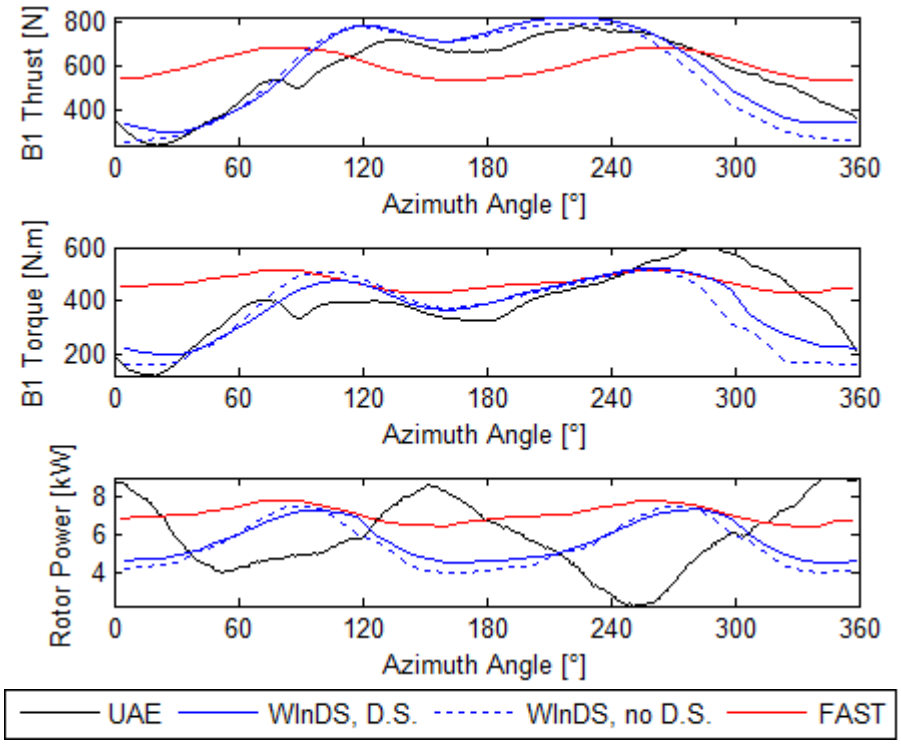

Figure C.12: Thrust and torque per blade and total aerodynamic rotor power for UAE Sequence S, 15 m/s, 60° yaw

BIBLIOGRAPHY

Abbott, I.H., von Doenhoff, A.E. 1959. "Theory of Wing Sections." 2nd Ed. Dover Publications: New York, NY.

Anderson Jr., J. D. 2007. "Fundamentals of Aerodynamics." 4th Ed. McGraw-Hill: New York, NY.

Beddoes, T.S. 1976. "A Synthesis of Unsteady Aerodynamic Effects under Dynamic Stall Conditions and Low Mach Number." Vertica, 1, no. 2, pp.113-123.

Beddoes, T.S. 1978. "Onset of Leading Edge Separation Effects under Dynamic Conditions and Low Mach Number." 34th Annual National Forum of the American Helicopter Society Proceedings, Washington, D.C., May 1978.

Beddoes, T.S. 1983. "Representative Airfoil Behavior." Vertica, 7, no. 2, pp. 183-197.

Beddoes, T.S. 1984. "Practical Computation of Unsteady Lift." Vertica, 8, no. 1, pp. 55-71.

Breton, S.-P. 2008. "Study of the stall delay phenomenon and of wind turbine blade dynamics using numerical approaches and NREL's wind tunnel tests." PhD Thesis presented to the Norwegian University of Science and Technology.

Carta, F.O. 1971. "Effect of Unsteady Pressure Gradient Reduction on Dynamic Stall Delay." Journal of Aircraft, 8, no. 10, pp. 839-840.

Coton, F.N., Wang, T., Galbraith, R.A.McD. 2002. "An Examination of Key Aerodynamic Modelling Issues Raised by the NREL Blind Comparison." Wind Energy, 5, pp. 199-212.

deVelder, N.B. 2014. "Free Wake Potential Flow Vortex Wind Turbine Modeling: Advances in Parallel Processing and Integration of Ground Effects." M.S. Thesis presented to the University of Massachusetts, Amherst.

Du, Z., Selig, M.S. 1998. "A 3-D Stall-Delay Model for Horizontal Axis Wind Turbine Performance Predictions." ASME 1998 Wind Energy Symposium, Reno, NV, 1998.

Ericsson, L.E. 1967. "Comment on unsteady airfoil stall." Journal of Aircraft, 4, no. 5, pp. 478-480.

Eggers Jr., A.J., Chaney, K., Digumarthi, R. 2003. "An Assessment of Approximate Modeling of Aerodynamic Loads on the UAE Rotor." ASME 2003 Wind Energy Symposium, Reno, NV, 2003.

Green, R.B., Galbraith, R.A.McD. 1995. "Dynamic recovery to fully attached aerofoil flow from deep stall." AIAA Journal, 33, no. 8, pp. 1433-1440.

Gupta, S., Leishman J.G. 2006. "Dynamic Stall Modelling of the S809 Aerofoil and Comparison with Experiments." Wind Energy, 9, pp. 521-547.

Ham, N.D., 1968. "Aerodynamic Loading on a Two-Diminsional Airfoil during Dynamic Stall." AIAA Journal, 6, no. 10, pp. 1927-1934.

Hand, M.M., et al. 2001. “Unsteady Aerodynamics Experiment Phase VI: Wind Tunnel Test Configurations and Available Data Campaigns.” NREL/TP-500-29955.

Huyer, S.A., Simms, D., Robinson, M.C. 1996. “Unsteady Aerodynamics Associated with a Horizontal-Axis Wind Turbine.” AIAA Journal, 34, no. 7, pp. 1410-1419.

Jones, R.T. 1938. “Operational treatment of the non-uniform lift theory in airplane dynamics.” NASA Technical Note 667.

Jones, R.T. 1940. “The Unsteady Lift of a Wind of Finite Aspect Ratio.” NACA Report 681.

Jonkman, J.M. 2007. “Dynamics Modeling and Loads Analysis of an Offshore Floating Wind Turbine.” NREL/TP-500-41958.

Jonkman, J.M. 2010. “Definition of the Floating System for Phase IV of OC3.” NREL/TP-500-47535.

Jonkman, J.M., Buhl Jr., M.L. 2005. “FAST User’s Guide.” NREL/EL-500-38230.

Jonkman, J.M., Butterfield, S., Musial, W., Scott, G. 2009. “Definition of a 5-MW Reference Wind Turbine for Offshore System Development.” NREL/TP-500-38060.

Johnson, W., Ham. N.D. 1972. “On the Mechanism of Dynamic Stall.” Journal of the American Helicopter Society, 17, no. 4, pp. 36-44.

Kaiser, M.J., Snyder, B. 2010. “Offshore Wind Energy Installation and Decommissioning Cost Estimation in the U.S. Outer Continental Shelf.” U.S. BOEMRE TA&R 648.

Kramer, M. 1932. “Increase in the Maximum Lift of an Airfoil Due to a Sudden Increase in Its Effective Angle of Attack Resulting from a Gust.” NACA Technical Memorandum 687.

Laino, D.J., Hansen, A.C. 2002. “User’s Guide to the Wind Turbine Aerodynamics Computer Software AeroDyn.” NREL Subcontract No. TCX-9-29209-01.

Landgrebe, A.J. 1995. “New Direction in Rotorcraft Computational Aerodynamics Research in the U.S.” AGARD Conference Proceedings no. 552.

Leishman, J.G. 1988. “Validation of Approximate Indicial Functions for Two Dimensional Subsonic Flow.” Journal of Aircraft, 25, no. 10, pp. 914-922.

Leishman, J.G. 1989. “Modeling Sweep Effects of Dynamic Stall.” Journal of the American Helicopter Society, 34, no. 3, pp. 18-29.

Leishman, J.G. 2002. “Challenges in Modeling the Unsteady Aerodynamics of Wind Turbines.” AIAA Paper, 40th AIAA Aerospace Sciences Meeting, Reno, NV.

Leishman, J.G. 2006. “Principles of Helicopter Aerodynamics.” Cambridge University Press: New York, NY.

Leishman, J.G. 2011. “Final Report: Assessment of ‘AeroDyn’ Theory Basis Including Unsteady Aerodynamics Modules.” NREL Subcontract No. LFC-1-11303-01 under Prime Contract No. DE-AC36-08GO28308.

Leishman, J.G., Beddoes, T.S. 1986. “A Generalized Method for Unsteady Airfoil Behavior and Dynamic Stall Using the Indicial Method.” 42nd Annual Forum of the American Helicopter Society, Washington, DC, Jun. 2-5.

Leishman, J.G., Beddoes, T.S. 1989. “A Semi-Empirical Model for Dynamic Stall.” Journal of the American Helicopter Society, 34, no. 3, pp. 3-17.

Lomax, H., Heaslet, M. A., Fuller, F. B., and Sluder, L. 1952. “Two and Three Dimensional Unsteady Lift Problems in High Speed Flight.” NACA Report 1077.

Manwell, J.F., McGowan, J.G., Rogers, A.L. 2002. “Wind energy explained.” University of Massachusetts, Amherst, USA. John Wiley and Sons Ltd.

Matha, D. 2009. “Model Development and Loads Analysis of an Offshore Wind Turbine on a Tension Leg Platform, with Comparison to Other Floating Turbine Concepts.” PhD Thesis presented to the University of Colorado, Boulder. NREL/SR-500-45891.

McAlister, K.W., Carr, L.W. 1979. “Water tunnel visualizations of dynamic stall.” Journal of Fluids Engineering, 101, no. 3, pp. 376-380.

McCroskey, W.J. 1973. “Inviscid flowfield of an unsteady airfoil.” AIAA Journal, 11, no. 8, pp. 1130-1137.

McCroskey, W.J., Carr, L.W., McAlister, K.W. 1976. “Dynamic Stall Experiments on Oscillating Airfoils.” AIAA Journal, 14, no. 1, pp. 57-63.

OSU Wind-Tunnel Test Data. Accessed at <http://wind.nrel.gov/airfoils/OSU_data/data/>.

Ramsay, R.R., Hoffmann, M.J., Gregorek, G.M. 1995. “Effects of Grit Roughness and Pitch Oscillations on the S809 Airfoil.” NREL/TP-442-7817.

Robinson, M.C., Galbraith, R.A. McD., Shipley, D., Miller, M. 1995. “Unsteady Aerodynamics of Wind Turbines.” Paper 95-0526, 33rd Aerospace Sciences Meeting, Reno, NV, Jan. 1995.

Sebastian, T. 2012. “The aerodynamics and near wake of an offshore floating horizontal axis wind turbine.” PhD Thesis presented to the University of Massachusetts, Amherst.

Sebastian, T., Lackner, M.A. 2011. “Offshore floating wind turbines - an aerodynamic perspective.” In *49th AIAA Aerospace Sciences Meeting and Exhibit*, Orlando, FL, 2011. American Institute of Aeronautics and Astronautics.

Sebastian, T., Lackner, M.A. 2012. “Analysis of the Induction and Wake Evolution of an Offshore Floating Wind Turbine.” Energies, 5, pp. 968-1000.

Sebastian, T., Lackner, M.A. 2012. “Characterization of the unsteady aerodynamics of offshore floating wind turbines.” Wind Energy, 16, no. 3, pp. 339-352.

Simms, D., Schreck, S., Hand, M., and Fingersh, L. 2001. “NREL Unsteady Aerodynamics Experiment in the NASA-Ames Wind Tunnel: A Comparison of Predictions to Measurements.” National Renewable Energy Laboratory, NREL/TP-500-29494.

Tangler, J. L. 2002. “The Nebulous Art of Using Wind-Tunnel Airfoil Data for Predicting Rotor Performance.” 21st ASME Wind Energy Conference, Reno, NV, Jan. 14-17, 2002.

Tegen, S., Hand, M., Maples, B., Lantz, E., Schwabe, P., Smith, A. 2012. "2010 Cost of Wind Energy Review." NREL/TP-5000-52920.

Theodorsen, T. 1935. "General Theory of Aerodynamic Instability and the Mechanism of Flutter." NACA Report 496.

Thwaites, B. (Ed.). 1987. "Incompressible Aerodynamics." Dover Publications, New York, NY, 1987.

Timmer, W., van Rooij, R. 2001. "Some Aspects of High Angle-of-Attack Flow on Airfoils for Wind Turbine Application." European Wind Energy Conference and Exhibition, Copenhagen, July, 2001.

Tyler, J.C., Leishman, J.G. 1992. "Analysis of Pitch and Plunge Effects on Unsteady Airfoil Behavior." Journal of the American Helicopter Society, 37, no. 3, pp. 69-82.

Wagner, H., 1925. Über die Entstehung des dynamischen Auftriebes von Tragflügeln. *Zeitschrift für Angewandte Mathematik und Mechanik,* 5 (1), pp. 17–35.

Wang, Q., Xu, Y., Song, J.J., Li, C.F., Ren, P.F., Xu, J.Z. 2013. "3D stall delay effect modeling and aerodynamic analysis of swept-blade wind turbine." Journal of Renewable and Sustainable Energy, 5, no. 6.

Yu, Q., Chen, X. (2012). "Floating Wind Turbines." U.S. BSEE TA&R 669.